UC Irvine
UC Irvine Electronic Theses and Dissertations

Title

Multi-Scale Modeling for Morphogenesis of Healthy and Diseased Tissue

Permalink

https://escholarship.org/uc/item/19g3x4r6

Author

Figueroa, Seth Amin

Publication Date

2017

Peer reviewed|Thesis/dissertation

UNIVERSITY OF CALIFORNIA,
IRVINE

Multi-Scale Modeling for Morphogenesis of Healthy and Diseased Tissue

DISSERTATION

submitted in partial satisfaction of the requirements
for the degree of

DOCTOR OF PHILOSOPHY

in Biomedical Engineering

by

Seth Amin Figueroa

Dissertation Committee:
Professor Qing Nie, Chair
Professor Zoran Nenadic
Professor Jun Allard

2017

DEDICATION

You, the reader.

TABLE OF CONTENTS

LIST OF FIGURES

LIST OF TABLES

ACKNOWLEDGMENTS

CURRICULUM VITAE

Seth Amin Figueroa

EDUCATION

Doctor of Philosophy in Biomedical Engineering   **2017**
University of California - Irvine   *Irvine, CA*

Master of Science in Biomedical Engineering   **2016**
University of California - Irvine   *Irvine, CA*

Bachelor of Science in Biomedical Engineering   **2011**
Tulane University   *New Orleans, LA*

Bachelor of Science in Applied Mathematics   **2011**
Tulane University   *New Orleans, LA*

ABSTRACT OF THE DISSERTATION

Multi-Scale Modeling for Morphogenesis of Healthy and Diseased Tissue

By

Seth Amin Figueroa

Doctor of Philosophy in Biomedical Engineering

University of California, Irvine, 2017

Professor Qing Nie, Chair

In organisms, tissue development and maintenance must be precisely timed and spatially coordinated to ensure proper form and function. This can be difficult both to develop and to maintain in the complex environments present in organisms, and thus a mechanism that can be finely tuned and regulated must be present. Therefore, when studying the underlying principles of morphogenesis, it is important to consider the crucial biochemical, cellular, and tissue scales simultaneously. This creates a need for a mathematical and computational approach to understanding the complex biology of development. One way of achieving a high level of precision of control is through stem cell lineages. These lineages employ the use of stem cells and their progeny to maintain certain properties necessary for proper tissue function. One such system is found in the stratified inter-follicular epidermis. Here, we develop and use a two dimensional, multi-scale, cell lineage model to explore the molecular, cellular, and physical properties of healthy and diseased epidermis. The model recapitulates a variety of healthy epithelial tissue shapes, including the formation and maintenance of undulating structures, known as rete-ridges. We find that the dermis compliance and the cell-cell adhesion at the dermis-epidermis junction, in conjunction with internal physical pressures due to cell lineage dynamics, play an important role in the tissue morphology. We explore these dynamics to get a better understanding of morphological changes found in diseased skin, including thickening of the tissue and deformation of rete-ridges. Another

system in which the molecular mechanisms and cell dynamics driving morphogenesis remains unclear is in diversification of feather vane shapes. Here, we integrate a two dimensional, multi modular mathematical model with transcriptome profiling to elucidate the anisotropic signaling modules which break symmetry, alter cell shape, and generate diverse feather shapes. Overall, this work provides multi-dimensional frameworks to study development and applies them to various biological tissues to better understand their underlying processes.

INTRODUCTION

A tissue is an organized network of cells that performs a specific function in a multi-cellular organism. How the complex micro-environment at the molecular and gene-regulatory level, in conjunction with the macro-environment, at the cellular and tissue level, work to correctly grow and shape a tissue is still poorly understood. Moreover, understanding the pathology of a diseased tissue can be made more complex when dealing with such a large number of factors inherent in the development. The multi-scale nature of tissue development makes study of the organism using experiments very challenging and time consuming. In order to provide insight into a complex multi-level phenomenon, mathematical and computational modeling can be used to account for different biological observations at distinct spatial and temporal scales. For example, proteins often localize within a tissue on the order of minutes or seconds [4],the cell cycle can be on the order of hours or days [5], and overall tissue behavior can be on the time scale of weeks or months [6]. To integrate all these time scales into a single mathematical model can present significant computational challenges. Also, when handling all the spatial scales simultaneously in a mathematical model, the distribution of biochemical molecules, cell-to-cell interactions, and overall tissue movement and growth must be accounted for.

Tissue models that discretely account for cells can account for cell-to-cell interactions and the individuality of cellular decisions, but they can be computationally expensive. When modeling tissues using continuum methods, particularly in high dimensions, the growth of the tissue must be accounted for using moving interfaces representing tissue boundaries which often require special computational techniques. However, continuum models can be computationally efficient and incorporate morphogen gradients in a simple fashion. For each specific problem, tissue models and numerical methods can be developed to account for the crucial aspects specific to the problem. For example, the epidermis is stratified, with

stem cell accumulating in undulations that form at the basal boundary [7, 8], therefor a careful treatment of interfacial motion is needed to explore it's growth, morphology and pathological distortions. The well-studied presence of notch signaling in developing tissues [9] also serves as a specific problem that may need to be addressed using careful mechanisms that incorporate the individuality of cells.

Even with such computational challenges, tissue models can be very insightful in studying complex biological systems. In developmental biology, several important questions pertain to the morphophogenesis of healthy and diseased tissue. Computational experiments using tissue models provide a great avenue to explore the interdependence of these important concepts in an efficient and cost-effective manner without the inherent constraints in experiments.

This thesis aims to study the morphogenesis of healthy and diseased tissues using mathematical modeling. The primary model biological systems that are studied are stratified epithelia, the feather plumes, and the zebrafish pharyngeal jaw.

Chapter 1

A Spatial Cell Lineage Model for Healthy and Diseased Epidermis

1.1 Background

In organisms, proper tissue and organ development and maintenance must be precisely timed and spatially coordinated to ensure proper function. This can be difficult both to develop and to maintain in the complex environments present in organisms, and thus a mechanism that can be finely tuned and regulated must be present at each stage and level of an organisms life cycle. One way of achieving this precision of control is through stem cell lineages. These lineages employ the use of stem cells, transit amplifying or progenitor cells, and terminally differentiated cells to maintain tissues with certain properties necessary for proper tissue function. The homeostatic upkeep of tissues through a stem cell lineage is present in a variety of organisms, as well as a variety of tissues in each organism such as in the Zebrafish heart [10, 11], vertebra teeth [12, 13], feather follicles [14], Hematopoetic stem cells [15], among

others. In these organs, a balance between proliferation, differentiation, and apoptosis is needed to keep a specific population of each subset of cells functional in the organ [16].

In many of these examples, not only the population of the cells needs to be maintained, but also the organization and spatial distribution of the cells within the tissue often has an important role in the organ's function. It is often found that the stem cells form a niche, a specialized micro-environment where the stem cells reside [17, 18] and are protected. The local environment surrounding the niche also plays a role in cell fate determination of stem cell progeny and thus influences tissue structure as a whole. It has been shown that the stiffness and elasticity of structures surrounding the niche [19, 20], the surface chemistry [21], and signaling factors, such as calcium gradients [22, 23, 24], can affect stem cell fate and rate of proliferation. Due to the complexity of the surrounding environment, great importance lies in studying structural and functional changes in the cell lineage to harness its potential in regenerative medical applications, such as in scaffolding and tissue engineering applications [25, 26, 27], and understanding of associated diseases.

Ectodermal organs have emerged as a good model system to study tissue development, maintenance and organization. These organs can as they can continually turn over to regulate their size, topology, and ratio of differentiated cell types, depending on physiological needs or in response to injury [28]. Certain epithelia, such as epidermis, olfactory epithelium, and the cerebral cortex [29, 7, 8], often stratify into apical-basal cell layers, where stem cells reside in a niche along the basal layer and diffusive morphogens regulate the layering. Mathematical modeling has been used to elucidate principles on cell lineage dynamics and feedback regulations [30, 31, 32], as well as spatial dynamics of the tissue[26, 33, 34, 35]. For example, a one-dimensional continuum model has been developed to study Olfactory Epithelial structure [36]. In this study, tissue stratification and homeostasis are achieved through an apical-basal morphogen gradient and feedback regulation in the cell lineage.

4

Epithelia, though stratified in one direction, often have specialized structures in other dimensions. In the epidermis, along the basal layer are finger like structures which protrude into the basal-lamina known as rete-ridges [37]. It is at the base of these ridges that stem cells reside and a protected niche is formed. The importance of the stem cell niche and cell lineage feedback regulation as a cause of these undulating structures was studied previously [38]. Through computational analysis of the continuum two-dimensional model, it was found that the morphologies of stratified epithelia depend on spatial structure of the stem cell niche. In particular, undulating epithelial morphologies may develop when the niche forms along a dynamic, variable basal lamina as opposed to when its movement and formation are restricted by a rigid, fixed basal lamina.

In this model, one boundary has been assumed to be rigid and flat while the other is dynamic, allowing undulation and movement. It is unclear what will occur if both the apical and the basal sides allowing dynamic movement and undulating with unique and different morphologies. It has been observed that although undulations are more explicit along the basal layer, the apical layer can have an associated morphology as can be seen in the dorsal tongue [39, 1]. Incorporating more detailed tissue mechanics and biology in both sides into a model allow one to explore homeostasis and morphologies driven by fingerings of both boundaries. This will enable one us to investigate more complex tissue morphologies, including those that arise due to genetic diseases.

Here we investigate how dynamic structure of the boundaries and the feedback in the cell lineage may affect the formation of healthy and diseased stratified epithelial morphologies. We first present a two-dimensional continuum cell-lineage model with two dynamic interfaces able to deform and undulate. We then systematically explore the cellular dynamics in the model, which are driven by both the interactions between the tissue and the environment, and the internal spatial and temporal dynamics of the cell lineage. Simulations show the importance of rete-ridges in housing the stem-cell niche as well as increasing the surface

area of the basal-lamina to allow a larger influx of nutrients from the basal lamina, both of which can help the tissue grow to and maintain a proper homeostatic size. We also use the model as a novel way to look at key epidermal cell lineage properties, as well as the role of the epidermal-dermal interface to help us better understand the resulting morphology of diseased tissue.

1.2 Numerical Methods

1.2.1 Modeling the cell lineage in two dimensions with two dynamic boundaries

In this model, the cell lineage is made up of three distinct cell types: stem cells (SC), transit amplifying cells (TA), and terminally differentiated cells (TD) denoted as C_0, C_1, and C_2, respectively (fig. 1.1). Both SC and TA cells proliferate at rates ν_0 and ν_1. When proliferating they can either self-replicate, with a probability of p_0 and p_1, or differentiate, with a probability of $1 - p_0$ and $1 - p_1$. SC, TA cells and TD cells can undergo apoptosis at rates d_0, d_1, and d_2. The governing equations for the lineage accounting for growth of the tissue are given by eqs. (1.1) to (1.3)[36, 38].

$$\frac{\partial C_0}{\partial t} + \nabla \cdot \left(C_0 \vec{V} \right) = (2p_0 - 1)\,\nu_0 C_0 - d_0 C_0 \tag{1.1}$$

$$\frac{\partial C_1}{\partial t} + \nabla \cdot \left(C_1 \vec{V} \right) = 2(1 - p_0)\,\nu_0 C_0 + (2p_1 - 1)\,\nu_1 C_1 - d_1 C_1 \tag{1.2}$$

$$\frac{\partial C_2}{\partial t} + \nabla \cdot \left(C_2 \vec{V} \right) = 2(1 - p_1)\,\nu_1 C_1 - d_2 C_2 \tag{1.3}$$

By assuming incompressibility of the cells and normalizing their total concentration, eq. (1.4), we can sum eqs. (1.1) to (1.3) to give us the divergence of the velocity of the tissue due to cell turnover (eq. (1.5)). Furthermore, we assume the tissue follows Darcy's Law [40, 41] such that the cells move down a pressure gradient proportional to some constant (K), giving us a Poisson equation for the pressure in the tissue due to cell turnover, seen in eq. (1.7).

$$C_0 + C_1 + C_2 = 1 \tag{1.4}$$

$$\nabla \cdot \overrightarrow{V} = (\nu_0 - d_0)\, C_0 + (\nu_1 - d_1)\, C_1 - d_2 C_2 = \varphi \tag{1.5}$$

$$\overrightarrow{V} = -K\nabla P \tag{1.6}$$

$$-\Delta K P = \varphi \tag{1.7}$$

Here, we consider the tissue as a two-dimensional growing domain $\tilde{\Omega} = (0,1) \times (h_0, h_1)$, in which both $h_0 = h_0(x,t)$ and $h_1 = h_1(x,t)$ are dynamic boundaries that are a function of both space and time. h_0 Is considered the boundary at the basal lamina while h_1 is an apical boundary. The domain is taken to be periodic in the x direction. Along the apical and basal boundaries of the tissue, the different cell adhesion forces lead to surface tensions that may be caused by inter-cellular forces and cell-surface mechanics [42, 43]. From the Young-Laplace equation, the pressure difference across each of the boundaries is assumed to be proportional to the local curvatures (κ) and some constant (ξ):

$$P_1^{\text{inside}} - P_1^{\text{outside}} = \xi_1 \kappa_1 = \xi_1 \frac{\frac{\partial^2 h_1}{\partial x^2}}{[1 + (\frac{\partial h_1}{\partial x})^2]^{\frac{3}{2}}} \tag{1.8}$$

$$P_0^{\text{inside}} - P_0^{\text{outside}} = \xi_0 \kappa_0 = \xi_0 \frac{\frac{\partial^2 h_0}{\partial x^2}}{[1 + (\frac{\partial h_0}{\partial x})^2]^{\frac{3}{2}}} \tag{1.9}$$

At the apical boundary, we assume the pressure outside the tissue is negligible, giving us eq. (1.10) for the boundary pressure. For the basal boundary, we assume that due to the compressive forces of the dermis, which consists of connective tissue, there is a non-negligible pressure acting on the boundary. Here we model the compressive force of the dermis using

Hooke's law, whereby the amount of pressure the connective tissue exerts on the basal boundary of the epidermis is proportional to the depth (z) of the epidermal rete-ridges, where k is the spring constant of the dermis, giving us eq. (1.11) for the pressure at the basal boundary.

$$P_1 = \xi_1 \frac{\frac{\partial^2 h_1}{\partial x^2}}{[1 + (\frac{\partial h_1}{\partial x})^2]^{\frac{3}{2}}} \tag{1.10}$$

$$P_0 = \xi_0 \frac{\frac{\partial^2 h_0}{\partial x^2}}{[1 + (\frac{\partial h_0}{\partial x})^2]^{\frac{3}{2}}} - kz \tag{1.11}$$

The kinematic condition governing the movement of the dynamic boundary, $h_{0,1}$ is given by eq. (1.12), where u and w are the velocities of tissue movement in the x and y directions, i.e. $\overrightarrow{V} = u\mathbf{i} + w\mathbf{j}$.

$$\frac{\partial h_{0,1}}{\partial t} + u(x, h_{0,1}, t) = w(x, h_{0,1}, t) \tag{1.12}$$

1.2.2 Transformation to the Unit Square

To solve the partial differential equations governing the system we transform the domain $\tilde{\Omega} = (0, 1) \times (h_0, h_1)$ to the unit square $\Omega = (0, 1) \times (0, 1)$. We apply the coordinate system in eqs. (1.13) to (1.15), to give us the transformed derivatives for the system, eqs. (1.18) to (1.21) [38, 44]. For all simulations, the transformation function found in eq. (1.24) is used.

$$t = \tau \tag{1.13}$$

$$x = X \tag{1.14}$$

$$y = F(X, Y, \tau) \tag{1.15}$$

$$F(X, 0, \tau) = h_0(x, t) \tag{1.16}$$

$$F(X, 1, \tau) = h_1(x, t) \tag{1.17}$$

$$\frac{\partial}{\partial t} = \frac{\partial}{\partial \tau} - g_1 \frac{\partial}{\partial Y} \tag{1.18}$$

$$\frac{\partial}{\partial x} = \frac{\partial}{\partial X} - g_2 \frac{\partial}{\partial Y} \tag{1.19}$$

$$\frac{\partial}{\partial y} = g_3 \frac{\partial}{\partial Y} \tag{1.20}$$

$$\Delta = \frac{\partial^2}{\partial x^2} + \frac{\partial^2}{\partial y^2} = \frac{\partial^2}{\partial X^2} + g_4 \frac{\partial^2}{\partial Y^2} + g_5 \frac{\partial^2}{\partial XY} + g_6 \frac{\partial}{\partial Y} \tag{1.21}$$

$$g_1 = \frac{F_\tau}{F_Y}, \quad g_2 = \frac{F_X}{F_Y}, \quad g_3 = \frac{1}{F_Y} \tag{1.22}$$

$$g_4 = (g_2)^2 + (g_3)^2, \quad g_5 = -2g_2, \quad g_6 = g_2 \frac{\partial g_2}{\partial Y} + g_3 \frac{\partial g_3}{\partial Y} - \frac{\partial g_2}{\partial X} \tag{1.23}$$

$$F(X, Y, \tau) = \frac{(h_1(X, \tau) - h_0(X, \tau)) \left(\frac{\arctan[(2Y-1)\tan[\omega]]}{\omega} + 1 \right)}{2} + h_0(X, \tau) \tag{1.24}$$

10

1.2.3 Modeling Diffusive Signaling Molecules

It has previously been shown that Calcium (Ca) is a signaling factor which regulates epidermal structure through inducing differentiation in keratinocytes [22, 23, 24]. In the epidermis, a calcium gradient is formed where there is a high concentration near the apical cell layers, where there are more differentiated cells, while near the basement membrane there is a low concentration of calcium. In our model, we allow calcium to diffuse throughout the tissue and influence the cell lineage through inhibiting both SC and TA cells self-renewal probabilities, eq. (1.25). Similarly, we assume that nutrients (N) are able to diffuse from the dermis across the dermis-epidermis junction and throughout the epidermis. These nutrients are necessary for cell survival and thus an absence of nutrients will cause the cell to undergo apoptosis. The concentration of N in the system increases cell death rates through, eq. (1.26).

The diffusion of the morphogens throughout the tissue is governed by eqs. (1.27) and (1.28), where, D_{Ca} and D_N are diffusion coefficients, Ca_{deg} and N_{deg} are degradation rates, and the cell type C_j produces respective morphogen at a rate of μ_j, η_j, or consumes the morphogens at a rate of ζ_j, and ρ_j. The apical boundary of the tissue is assumed to have tight junctions[45], which are treated as an impermeable, no-flux boundary for both Ca and N. Calcium is kept low in the basal layers of the tissue by making the basal boundary a leaky boundary, meanwhile Dirichlet boundary conditions are used for Nutrition at basal boundary to account for its influx from the dermis. This assumption gives the following boundary conditions in eqs. (1.29) and (1.30), Where $\hat{n}$ is the unit outward normal vector of the boundary.

$$p_0 = \frac{\bar{p}_0}{1 + \left(\frac{[Ca]}{\gamma_0}\right)^{m_0}}, \qquad p_1 = \frac{\bar{p}_1}{1 + \left(\frac{[Ca]}{\gamma_1}\right)^{m_1}} \tag{1.25}$$

$$d_0 = \frac{\bar{d}_0}{1 + \left(\frac{[N]}{\varsigma_0}\right)^{n_0}}, \qquad d_1 = \frac{\bar{d}_1}{1 + \left(\frac{[N]}{\varsigma_1}\right)^{n_1}}, \qquad d_2 = \frac{\bar{d}_2}{1 + \left(\frac{[N]}{\varsigma_2}\right)^{n_2}} \tag{1.26}$$

$$\frac{\partial [Ca]}{\partial t} + \nabla \left([Ca]\vec{V}\right) = D_{\mathrm{Ca}}\Delta[Ca] + \sum_j^2 \mu_j C_j - \mathrm{Ca_{deg}} \sum_j^2 \zeta_j C_j [Ca] \tag{1.27}$$

$$\frac{\partial [N]}{\partial t} + \nabla \left([N]\vec{V}\right) = D_N \Delta[N] + \sum_j^2 \eta_j C_j - N_{\mathrm{deg}} \sum_j^2 \rho_j C_j [N] \tag{1.28}$$

$$\nabla Ca \cdot \hat{n}|_{y=h_1} = -\alpha_1 [Ca], \qquad \nabla Ca \cdot \hat{n}|_{y=h_0} = -\alpha_0 [Ca] \tag{1.29}$$

$$\nabla N \cdot \hat{n}|_{y=h_1} = -\beta_1 [N], \qquad N|_{y=h_0} = \beta_0 \tag{1.30}$$

1.2.4   Spatial and Temporal Discretizations

Now that the governing equations on Ω and $\tilde{\Omega}$ have been transformed to a rectangular domain, here we present the methods used to solve the transformed system in eqs. (1.7), (1.27) and (1.28).

Both curvatures $\kappa_{0,1}$ and g_6 are functions of the second derivative of the kinematic boundaries in the transformed domain regardless of the particular choice of F in eq. (1.15). As a result, P depends on the second derivative of $h_{0,1}$ while the partial derivatives of P govern the movement of $h_{0,1}$ as evident in eq. (1.12). Naturally, it follows that the movement of $h_{0,1}$ is implicitly dependent upon their own third derivative, and solving the transformed system of equations requires a high-order accuracy of the spatial discretization in the X-direction to maintain overall second-order accuracy.

Here, we use fourth-order central difference approximations for the derivatives of h and the partial derivatives of P in the X-direction:

$$\frac{\partial f}{\partial X} \approx \frac{-f_{i+2} + 8f_{i+1} - 8f_{i-1} + f_{i-2}}{12\Delta X} \tag{1.31}$$

$$\frac{\partial^2 f}{\partial X^2} \approx \frac{-f_{i+2} + 16f_{i+1} - 30f_i + 16f_{i-1} - f_{i-2}}{12\Delta X^2} \tag{1.32}$$

Because of the assumed periodic boundary conditions in the X direction of our system, the five-point stencil in the X-direction near the boundary can be implemented in a straight-forward fashion. For the discretization of the partial derivatives in the Y-direction, we use second-order central difference approximations.

To explicitly track the movement of the boundaries $h_{0,1}$ governed by the kinematic equation eq. (1.12), a second-order upwind approximation is used to discretize in space:

$$\frac{\partial h}{\partial X} \approx \begin{cases} \frac{3h_i - 4h_{i-1} + h_{i-2}}{2\Delta X}, & \text{if } u(X, Y|_{0,1}, \tau) > 0 \\ \\ \frac{-3h_{i+2} + 4h_{i+1} - h_i}{2\Delta X}, & \text{if } u(X, Y|_{0,1}, \tau) < 0 \end{cases} \tag{1.33}$$

For time evolution, a second-order TVD Runge-Kutta is used [46]. The morphogens are considered at a quasi-steady state, equating the left-hand side of eqs. (1.27) and (1.28) to zero. All calculations and plots were carried out using MATLAB. We demonstrate the order of accuracy for the mathematical model employed to solve the inter-facial motion using the transformation scheme found in eqs. (1.13) to (1.23) in tables 1.1 to 1.4. The overall spatio-temporal accuracy of the method is of second order. All simulations use the transformation scaling function F described in eq. (1.24) seen in fig. 1.2. A maximum norm difference between successive approximations is used to compute the error and order of accuracy.

Parameters for all simulations can be found in Appendix A.

1.3 Model Captures Morphological Traits of Various Healthy Epithelium Tissues

Our two-dimensional tissue model with two dynamic boundaries, shows that the spatial gradients of morphogens and their regulations on self-replication can lead to formation of a stem cell niche and stratification of the tissue (fig. 1.3A). In particular, the stem cell niche resides along the basal lamina, and TA cells reside near the bottom of the tissue as well, with TD cells occupying the upper regions of the tissue. Such spatial organization is controlled by the rapid uptake of calcium by the basal layer, forming a calcium gradient which is high apically. This calcium gradient results in higher self-replication probabilities for SC and TA cells (eq. (1.25)) near the basal lamina, and lower self-replication probability nearer the top of the tissue, prompting cells to differentiate as they migrate away from the basal lamina. Nutrient influx from the dermis creates a gradient which is high near the dermis-epidermis junction, and decreases apically. The nutrient gradient is partially responsible for the size of the tissue, since the death rate of the cells increases as nutrient concentration becomes sparse (eq. (1.26)).

By inducing a small perturbation of the basal lamina (fig. 1.3 B), rete-ridge formation is prompted, whereby the niche is housed at the most basal portion of the ridge. As the rete-ridges form and grow into the dermis, the calcium gradient within the ridge becomes steeper. This creates a niche in which the probability of self-replication of SC increases as the ridge grows larger. The pressure in the tissue due to the proliferation of SC and TA cells becomes a driving force, forcing the tissue ridge to grow longer, and protrude deeper into the dermis. Although the curvature of the boundary increases as the protrusions grow larger, it appears that the deformation of the tissue continues indefinitely, previously seen in Ovadia 2013, meaning the tissue does not reach a steady state (fig. 1.4 A, C). With the addition of the pressure feedback on the epidermis by the dermis in eq. (1.11), as the rete-ridges

grow longer, the force exerted on the tissue by the dermis becomes larger. Eventually a balance occurs between the SC niche driving growth of the epidermis and the resistance of the dermis, leading the tissue to reach a steady state (fig. 1.4 B, D).

The model, which has two free moving boundary, allows for a high diversity of epidermis morphologies, each with unique characteristics. In the oral cavity, a wide range of epidermis morphology can be found. These can be separated into three types: masticatory, lining, and specialized [1, 47, 48]. It is hypothesized that since masticatory epidermis, such as gingiva, are exposed to more forces than lining epidermis, they have longer rete-ridges to help dissipate the stress. The dorsal tongue, meanwhile, has papillae which protrude from the apical surface of the epidermis. It is thought that this increases the surface area of the tongue, helping the tongue grip food, clean the mouth, and spread saliva [49]. It has previously been shown that in some oral mucosa, there are highly proliferative cells that quickly lose a radio-labeled DNA nucleoside [50, 51], while in others the proliferation rate is lower and the nucleoside label is preserved [52, 53]. In gingiva, compared to lining tissues like ventral tongue, the number of cells which retained the nucleoside labels after 45 days is much higher[54]. Most often it is found that masticatory tissue has a long turnover time compared to lining mucosa, which replenishes all of the cells in the epithelium much more quickly, possibly due to necessitating more wound healing abilities [55]. In our model we simulated two tissues: One which had the low proliferation rate ($\nu_1 = 0.1$) and low turnover rate ($d_2 = 0.5$) of masticatory tissue, and one with high proliferation rate ($\nu_1 = 1$) and high turnover rate ($d_2 = 2$) of a lining tissue, (fig. 1.5 A, B). The simulations captured similar morphology to examples of masticatory (Gingiva) and lining (Lip) histologies found in mice [1]. The with low TA proliferation and low apoptosis formed a tissue which is thick and has large, wide rete-ridges. In contrast, by increasing TA proliferation as well as cell apoptosis, the model simulates a thin, nearly flat tissue. Finally, by decreasing the stiffness of the dynamic apical boundary, the model can simulate a tissue which forms long, protruding papillae similar to dorsal tongue tissue (fig. 1.5 C).

15

1.4 Homeostatic Tissue Size Dependent Formation of Rete-Ridges

Here we look at the influence rete-ridge formation and nutrition have on the final size of the epidermis. We first look at the case where rete-ridge formation suppressed and a tissue with a flat basal boundary is produced (fig. 1.6 A,D,G). When there is a low production of nutrition (β_0) in the dermis, a thin tissue is formed. As the amount [N] produced in the dermis increases, the final steady state size of the tissue increases (fig. 1.6 J, blue solid line). Note that the tissue area increases at a lower rate than the production of [N] in the dermis is increased. This is due to nutrition produced along a single dimension, and therefore increases linearly and not quadratically, as tissue area does. The increase in tissue area would also depend on the cell type distribution, with different cells possibly consuming nutrition at different rates.

When we do not inhibit the formation of rete-ridges, the same trend of tissue area increase with the increase of β_0 occurs (fig. 1.6 J, red dashed, and black dotted line). Moreover, we see that when keeping β_0 constant, the steady state tissue area is influenced by the number of rete-ridges that form. This occurs even when the length of the rete-ridges is kept constant. One reason an increase in the number of rete-ridges formed increases the tissue area is through increasing in surface area of the basal lamina. The undulations formed by the rete-ridges create a larger area for nutrition flux from the dermis to the epidermis. We took the length of the basal lamina into account when looking at final tissue size and interestingly we still see that tissue simulations with two rete-ridges with equally long basal laminas do not grow to the same size tissues with three rete-ridges (fig. 1.6 K). We see that tissue size is influenced by more than the surface area of the basal lamina produced by rete-ridge formation. We hypothesize that there is also an importance in the rete-ridges forming and housing the stem cell niche. An increase in the number of rete-ridges increase the amount

of stem cell niches formed, which can then supply the tissue with a larger influx of TA and ultimately TD cells, forming a larger tissue. The effect that rete-ridge size has on final tissue size could have an impact on how tissues are grown in-vitro. New evidence suggests that tissue grown on engineered scaffolds which allow for the formation of rete-ridges has an effect on tissue health [56].

1.5 Epidermal Cell Lineage Properties in Psoriasis

Psoriasis is a complex, chronic, inflammatory disease of the epidermis whose causes are not yet fully understood. The disease ranges in severity from a few scattered red, scaly plaques to involvement of almost the entire body surface and is estimated to affect about 24% of the population in western countries [57]. The degree of severity depends on genetic and environmental factors, and there is currently no known cure. The histopathology of psoriasis differs according to the stage and manner of the disease. Psoriasis vulgaris, the most common form, causes a thickening of the epidermis (acanthosis), elongated epidermal rete-ridges, an extended spinous layer, a diminished thickness of the stratum granulosum with less discrete layers, an irregular and thickened stratum corneum (hyperkeratosis) and psoriatic plaque formation [58, 59, 60]. The leading theory in plaque psoriasis is that pathogenic immunity is responsible for an increase in keratinocyte proliferation. It is believed that T cells and dendritic cells, together with the pro-inflammatory cytokines and chemokines that they secrete, create a pro-inflammatory environment in the skin that stimulates the proliferation of keratinocytes [58, 61]. It is also thought that apoptosis is decreased as a result of the increased T cell inflammatory response [62, 63] further contributing to the increase in keratinocyte presence [34, 64]. The increase in keratinocyte proliferation in the basal layers of the epidermis as well as incomplete terminal differentiation of late stage keratinocytes and decreased apoptosis is thought to distort the morphology of the tissue.

We first explore the effects of keratinocyte proliferation rate, modeled as the cell cycle rate of TA cells (ν_1), and its effects on healthy tissue. We look at two morphological elements of the tissue, the length of the rete-ridges and the area of the tissue. The length of the rete-ridges is the vertical distance between the lowest point of the basal boundary and the highest point of the basal boundary ($Length = \max_{0 \le x < 1} h_0(x) - \min_{0 \le x < 1} h_0(x)$). We find that an increase in the proliferation rate of TA cells decreases the rete-ridge length of the tissue and increases the area of the tissue(fig. 1.7 A, B). The increase in tissue area is analogous to a thickening

of the epidermis seen in psoriatic tissue. In this case, by increasing the cell cycle rate from $\nu_1 = 0.1$ to $\nu_1 = 1.2$, the area of the tissue increased over 50%. The increase in tissue area is due to the higher proliferation rate of TA cells causing an influx of cells increasing the internal pressure, expanding the tissue. The rete-ridge length decreasing is less pronounced, whereby increasing the cell cycle rate from $\nu_1 = 0.1$ to $\nu_1 = 1.2$, decreased the rete-ridge length by 26%. When there is low TA cell proliferation, positive internal tissue pressure is driven mainly by the SC niche, which is located at the most basal top of the rete-ridges (fig. 1.7C). Pressure due to SC proliferation is what causes fingering to occur, and the rete-ridges mainly expand downward, into the dermis. When there is high TA cell proliferation then positive internal tissue pressure is located in more apical areas of the rete-ridge and not concentrated at the basal tip (fig. 1.7 D). This pressure profile distributes much of the rete-ridge expansion laterally, creating wider, but ultimately shorter rete-ridges. We can also observe that there are areas of high pressure near the apical boundary showing that slight papillae formations.

We next explore how premature differentiation affects tissue morphology. We model premature differentiation as a decrease in a TA cell's self-replication probability (p_1). Along the basal boundary, the model shows that, depending on whether p_1 is greater than or less than 0.5, an increase in keratinocyte differentiation can results in an increase or decrease in rete-ridge length (fig. 1.7 D). The biggest change in rete-ridge length occurs when $p_1 > 0.5$, whereby increasing TA cells self-replication probability from 0.5 to 0.9 decreases rete ridge length by 37%. When $p_1 < 0.5$, a change in TA cells self-replication probability from 0.5 to 0.1 decreases rete-ridge length by 5%. The reason for this discrepancy between TA cell self-replication probability and tissue morphology occurring when p_1 changes between 0.5, is that TA cells change from sustaining or increasing its own population ($p_1 \geq 0.5$) to TA cells being unable to sustain their own population size ($p_1 < 0.5$). When TA cells cannot sustain their own population size, then the driving force for rete-ridge elongation is located at their basal tip (fig. 1.7 G), similar to when TA cell proliferation rate is low. When $p_1 \geq 0.5$, the

internal pressure driving rete-ridge is found in a larger area of the rete-ridge, creating wider, yet shorter undulations (fig. 1.7 H). The area of the tissue, however, consistently increases as p_1 increases, creating thicker tissues (fig. 1.7 F).

Apoptosis of differentiated cells in the model is regulated by the parameter d_2, which is the rate at which TD cells exit the cell lineage. When decreasing d_2, the area of the tissue increases while there is no change in rete-ridge length (fig. 1.7 I, J). We hypothesize the reason there is no change in rete-ridge length is that TD cells are mostly found above the rete-ridge, moreover their death occurs mainly at the most apical end of the tissue, and thus a change in their behavior has little effect on the pressure in the rete-ridges. We can see this in fig. 1.7K and L where the pressures at the basal boundaries are similar in shape and magnitude. This means that the increase in tissue area comes solely from an increase in the apical portion of the tissue. As few cells exit the system through apoptosis, the tissue is forced to grow larger to accommodate.

Overall, the changes in internal pressure magnitude and location due to changes in cell lineage dynamics can be seen to play a large role in rete-ridge size, and tissue area. Though changes to ν_1, p_1, and d_2 can result in an increased thickness of the tissue, as seen in psoriasis, no parameter change alone can account for the drastic increase in rete-ridge size observed in psoriatic tissue.

1.6   Role of the Epidermal-Dermal Interface in Tissue Architecture

With the dynamic, free moving boundaries of the tissue, the imposed surface tension from cell-to-cell adhesion, as well as the compliance of the dermis, are forces that help maintain the regularity of tissue morphology. We tested the effect of the epidermal-dermal physical properties on the epidermis morphology. In the model the compliance of the dermis is modeled by Hooke's law (eq. (1.11)), where its compliance is the coefficient k. Simulations changing the stiffness of the dermis shows that a stiffer, non-compliant dermis will decrease the rete-ridge length by preventing their ability to penetrate into the dermis (fig. 1.8 A). An increase in Dermis stiffness will also result in a smaller tissue area (fig. 1.8 B). Similar results are seen when the effects of increasing the surface tension (ξ_0) at the dermis-epidermis junction of in the basal boundary (fig. 1.8 E, F). We found that a high surface tension, representing strong cell-cell adhesion, reduced the length of the rete-ridges, while a low surface tension resulted in longer ridges. We also see that in both cases of increasing the surface tension of the basal boundary and decreasing the compliance of the dermis, the area of the tissue decreases, meaning that the tissue is not compensating for the loss in rete-ridges with an expanded layer of terminally differentiated cells. This loss of rete-ridge formation again supports the importance of rete-ridges in determining the final epidermis size. One difference that we see between changing basal boundary surface tension and dermis compliance is internal tissue pressure profile (fig. 1.8 C, D, G, H). Simulations show that a lower dermis stiffness will allow the rete ridge to come into equilibrium with a lower internal tissue pressure, while when the dermis is stiff the tissue will have a much higher internal tissue pressure at steady state. On the other hand, higher internal tissue pressure is found when boundary stiffness is low, compared to when boundary stiffness is high.

Another skin pathology, Acanthosis Nigricans (AN), manifests a variety of morphological changes in the epidermis similar to those found in Psoriasis, including a thickening of the epidermis and elongated rete-ridges [65, 66]. It is thought that that increase in keratinocyte proliferation and differentiation seen in AN is caused by dysfunctional Insulin receptors, over competition between insulin, and anti-insulin receptor antibodies affecting insulin growth factor receptors [67, 68, 69]. Unlike in psoriasis, however, AN is also characterized by severe papillomatous elevations, which are ridges formed at the apical boundary of the tissue. One difference between AN and psoriasis is that in psoriasis, psoriatic plaques often form at the top of the epidermis. It is thought that the abnormal retention of partly cornified cells is due to incomplete terminal differentiation of keratinocytes as well as infiltration of leukocytes [58]. It has been shown that cutaneous resonance running times (CRRTs), which are inversely proportional to skin stiffness, are decreased as the severity of psoriasis increases [70]. The formation of the psoriatic plaques could be one mechanism by which skin stiffness is increased with the onset of psoriasis. In our model the increase in the surface tension (ξ_1) of the apical boundary can be said to be analogous to increasing the stiffness of the boundary. We found that by decreasing the surface tension of the apical boundary there is an increase in papillae length, with the apical boundary becoming very undulated (1.8 I-L). When the surface tension of the apical boundary was increased, papillae formation could be eliminated. This shows that a stiffness of the apical boundary is able to prevent or facilitate the distortion of the tissue, possibly helping differentiate between the morphologies found between psoriasis and AN. It is also noted that changes in apical boundary stiffness has a small impact on tissue area, where formation of papillae increase tissue size.

The external environment surrounding the stem cell niche plays a large role in determining the morphology of the tissue. Our model shows that a strong cell-cell adhesion, which is modeled as a surface tension, at the basal boundary can impede fingering if it is too strong. The internal pressures due to cell proliferation in the stem cell niche cannot overcome the surface tension and thus, even with a perturbation, rete-ridges do not form resulting in a flat

boundary [71]. It has recently been hypothesized that mechanical stresses due to the physical pressures created by cell proliferation in the epidermis aid in remodeling the epidermis-dermis boundary and help make the rete ridges in oral mucosa [48]. Here we see how tissue formation is affected when the stem cell niche plays a role in determining the surface tension of the boundary surrounding it. We assume that a local, short range morphogen (A) is secreted by stem cells which are under high pressure (eq. (1.34)). Since the variable describing pressure, P, assumes both positive and negatives values, we use a modified hill function to model the production of morphogen A by the stem cells (eq. (1.35)). The morphogen acts locally to weaken the surface tension of the basal boundary

$$\frac{\partial[A]}{\partial t} + \nabla\left([A]\overrightarrow{V}\right) = D_A\Delta[A] + \Gamma C_0 - A_{\text{deg}}[A] \tag{1.34}$$

$$\Gamma = \begin{cases} \frac{P_{max}}{1+(\omega_p P)^{q_p}} & \text{if, } P \geq 0 \\ 0 & \text{, Otherwise} \end{cases} \tag{1.35}$$

$$\nabla A \cdot \hat{n}|_{y=h_1} = 0 \tag{1.36}$$

$$\nabla A \cdot \hat{n}|_{y=h_0} = -\sigma_0[A] \tag{1.37}$$

Where, D_A is the diffusion coefficient, $A_{d}eg$ is the degradation rate, and the SC C_0 produces respective morphogen at a rate of Γ, which is dependent on a modified hill function of pressure (P). The boundary conditions for morphogen A are:

The morphogen A, weakens the boundary through decreasing the surface tension:

$$\xi_0 = \frac{\bar{\xi}}{1 + (\omega_c[A])^{q_c}} + \xi_{min} \tag{1.38}$$

Assuming that the rate of flux of calcium out of the basal lamina is dependent on the cell-cell adhesion, then a weakening of the cell adhesion could also change the calcium flux (α_0).

Morphogen A acts on calcium flux through:

$$\alpha 0 = \frac{\bar{\alpha}}{1 + (\omega_\alpha[A])^{q_\alpha}} + \alpha_{min} \tag{1.39}$$

We study the model by first simulating a tissue in which the surface tension of the basal lamina is high enough to prevent rete-ridge formation entirely fig. 1.9 A, and morphogen A has no impact on either tissue surface tension or bounday leakyness. We find that by allowing the morphogen A to decrease the surface tension of the tissue, rete-ridges are able to form fig. 1.9 B. The rete-ridges have a short length, and appear to be more pointy and narrow than the usually formed ridges. This is most likely due to the boundary stiffness remaining high at the lateral sides of the rete-ridges, while it decreases most at the center line of the ridge. Finally by allowing the morphogen A to both weaken the surface tension of the basal boundary, as well as increase the flux of $[C_a]$ out of the epidermis, longer rete ridges form fig. 1.9 C.

1.7 Conclusion

In this chapter we explored the two-dimensional spatial effects of an epidermal stem-cell lineage on stratified tissue morphology through modeling. The two-dimensional model has two dynamic interfaces which are able to undulate and deform due to the internal tissue pressure of cell proliferation and cell death. Cell stratification in the model is achieved by the formation of a signaling morphogen gradient of Calcium, which is known to induce differentiation in keratinocytes [22, 23, 24]. A second gradient of nutrition influx from the dermis into the epidermis is formed which feeds cells, and inhibits cell apoptosis. The undulating morphologies simulated by the model are able to capture the healthy epithelial tissue forms [1], including those which have papillae protrusions on the apical boundary. We found that cell turnover time plays a role in final tissue form. A fast cell turnover times produce thinner, lining type tissue structures with small rete-ridges, while a slow cell turnover time increased both the area of the tissue as well as the rete-ridge length.

We speculate that the formation of proper rete-ridge size and number are an important part of healthy stratified tissue morphogenesis. When a flat tissue is assumed the tissue size to which it can grow is limited directly by the amount of nutrients produced by the dermis. However, when rete-ridges are able to form, the tissue is able to grow to a larger size, despite the low production of nutrient. We speculate the reason to be two-fold. Firstly, the increase in surface area of the epidermis-dermis boundary allows for a larger amount of dermis nutrients to flow into the epidermis, allowing the sustainability of a larger tissue. Simulations show, however, that the increase in surface area of the epidermis-dermis was not sufficient to explain the expanded tissue sizes. Tissues with a larger number of rete-ridges grew to a larger homeostatic size than their two rete-ridge counterparts, even when surface areas were kept the same. We speculate that this is due to ridges housing the stem cell niche. The protective niche environment formed houses the collection of stem cells which then proliferate and produce TA, and ultimately TD cells, which give rise to the tissue. A

larger number of these stem-cell niche environments is likely to give rise to a tissue with a larger homeostatic size. The model gives us insight into the importance of rete-ridge formation in ensuring a proper tissue size. This is something that can be important for use in developing tissues in vitro, where often the formation of rete-ridges is not something that is considered.

We used the model to explore epidermal cell lineage properties in psoriasis, a disease which results in thickened epidermis, with psoriatic plaque forming along the apical boundary, and elongated rete-ridges protruding deeply into the dermis. Psoriatic tissue differs from healthy tissue in that it has over proliferating keratinocytes, incomplete differentiation of keratinocytes, and decrease apoptosis. We explored these properties individually using out model and show that, while they can each produce a tissue which has some of the characteristic properties of psoriasis, they individually do not produce a thick tissue with elongated rete-ridges usually seen. The model shows that increased proliferation rate of TA cells has opposing effects on rete-ridge length and tissue area. As proliferation of TA cells increases so does the tissue area, due to the influx of cells forcing the tissue to expand. This influx of cells is located mainly in the middle regions of the rete-ridge, causing the ridges to have a more lateral-medial expansion, causing a decrease in final rete-length. Similar results are seen when the self-replication probability of TA cells are increased. As the probability of TA cells self-replicating during cell proliferation increases so does the area of the tissue. Interestingly, when the probability of self-renewal is below 0.5, increasing probability slightly increases rete-ridge length. However, once the threshold of 0.5 is crossed, increasing self-renewal probability drastically decreases the rete-ridge length. We hypothesize this is due to 0.5 being the threshold where TA cells can maintain and grow their own population through self-replication. At this threshold, the influx of TA cells again changes the pressure dynamics in the tissue creating shorter and wider rete-ridges. Finally, the change in TD cell death rate had a large effect on the final size attainable by the tissue. High levels of apoptosis led to tissue of smaller area. The rete-ridge formation in these tissues, however, remained

virtually unchanged by the change in apoptosis. We speculate this is due to the cellular dynamics being of the stem cell niche and the TA cells being largely unaffected by the TD cell population at the sizes we studied.

The role of the epidermis-dermis boundary is one which is still not fully understood and is difficult to explore both in vitro and in vivo. As such little experimental work has looked at the mechanical properties of the basal lamina in psoriasis. It is possible that the disease results in a weaker cell-cell binding than healthy tissue, resulting in a more easily deformed tissue shape. One possible reason for this is that psoriatic tissue has a higher in-flux of lymphocytes, T cells, and other inflammatory response cells migrating across the dermis-epidermis boundary [59, 60]. This movement of cells across the basal lamina would have a disruptive effect on the cell-cell adhesion as well as in the extra cellular matrix which comprises the structural integrity of the dermis [72, 73] leading to a more pliable boundary. We see from simulations that both the integrity of the cell-cell adhesion creating the surface tension at the boundary, and the compliance of the dermis, can allow or diminish rete-ridge protrusion into the dermis. Therefore, a tissue with a compromised strength of the epidermis-dermis boundary can distort, and allow excessively long rete-ridges to form. Moreover, the model shows that the surface tension of the apical boundary can allow for the formation of apical structures known as papillae to protrude outward. These protrusions are a charactaristic morphology of Acanthosis Nigricans, a disease which also shows epidermal thickening and formation of elongated rete-ridges, similar to psoriasis. The strength of the cell-cell adhesions, or the fact that psoriasis forms a psoriatic plaque at the apical boundary can be a reason why AN and psoriasis, though they have some similarity in morphology, differ in whether they form papillae protrusions.

By combining the results of exploring the cell lineage and the physical properties of the basal and apical boundaries we were able to simulate architecture of diseased diseased tissues, including thickened epidermis, elongated rete-ridges, and papillae protrusions fig. 1.10.

Psoriasis tissue was simulated by decreasing cell apoptosis, increasing keratinocyte proliferation rate while keeping the self-replication probability below 0.5. The epidermal-dermal junction compliance was also weakened. This allowed the tissue to increase in tissue area, while also expanding its rete-ridges deep into the dermis. AN tissue was simulated by by increasing cell proliferation rate and decreasing the stiffness of both the epidermal-dermal junction and the apical boundary. Extensions of the current modeling framework to incorporate more detailed tissue mechanics and elaborate signaling networks into the continuum model may also help understand the morphogenesis of healthy and abnormal epithelial tissues, with potential to identify novel components that may aid in forming treatment of epithelial diseases.

1.8 Figures and Tables
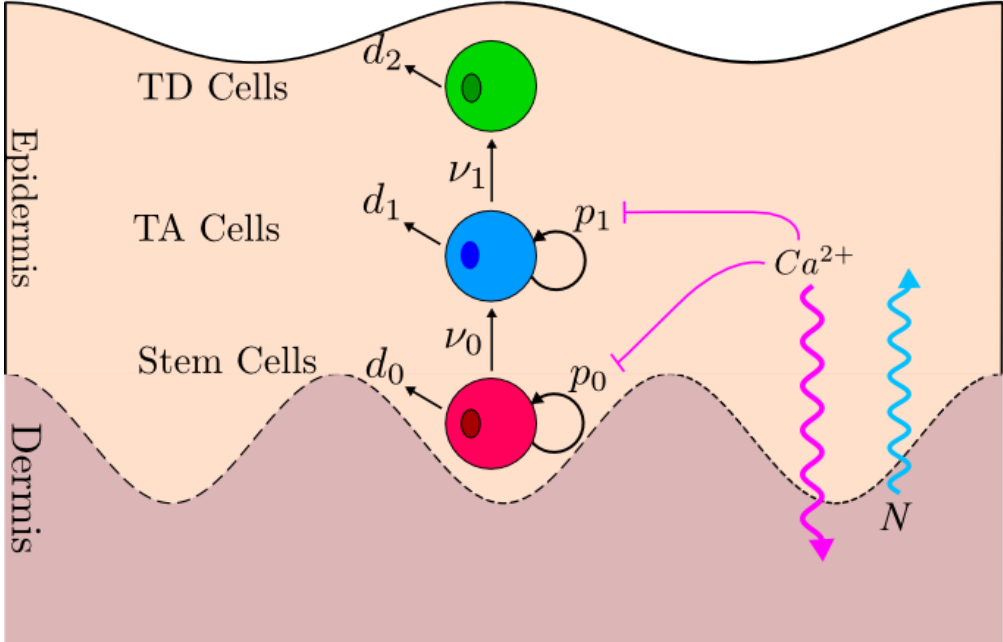
Figure 1.1: Schematic diagram of two-dimensional tissue and stem-cell lineage. Stem and TA cells proliferate with rates ν_0 and ν_1 and either self-replicate or differentiate upon division to become TD cells. All cells undergo natural cell death at a rate of d_0, d_1, d_2. The regulatory molecule Calcium (Ca^{2+}) is produced in the epithelium, diffuses throughout the tissue and can exit the tissue through a permeable basal lamina. Ca^{2+} acts as a differentiation signal and thus inhibits the self-replication probabilities of stem and TA cells, p_0 and p_1. A nutrient (N) diffuses through the basal lamina from the dermis into the epidermis. It diffuses throughout the tissue and is necessary for cellular survival. It therefore acts on the death rates of the cells, by inhibiting apoptosis. The apical surface serves as a closed tissue surface with tight junctions. Both apical and basal boundaries are free-moving.
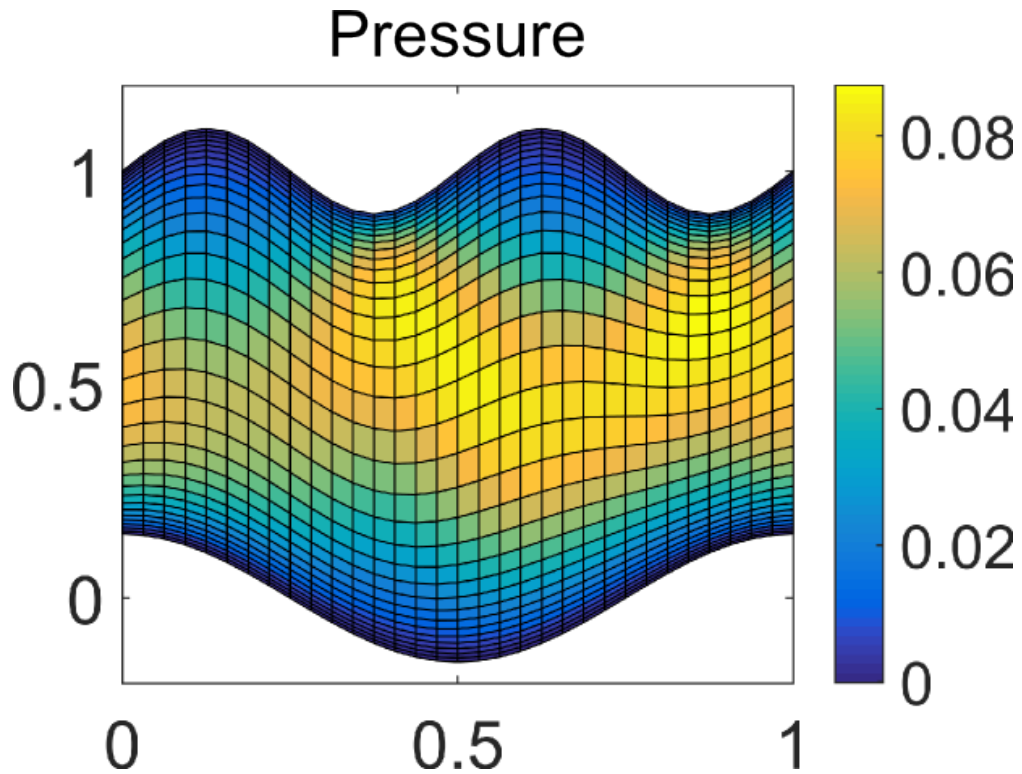
Figure 1.2: Pressure plotted on computational grids for numerical tests where N=32. The pressure equations being solved is $\Delta P = 1$, with $\xi_1 = \xi_0 = 1e-3$, $K = 1e-1$. The transformation scaling function F in eq. (1.24) is used. This scaling uses more grid points near the interface boundaries where gradients are sharper.
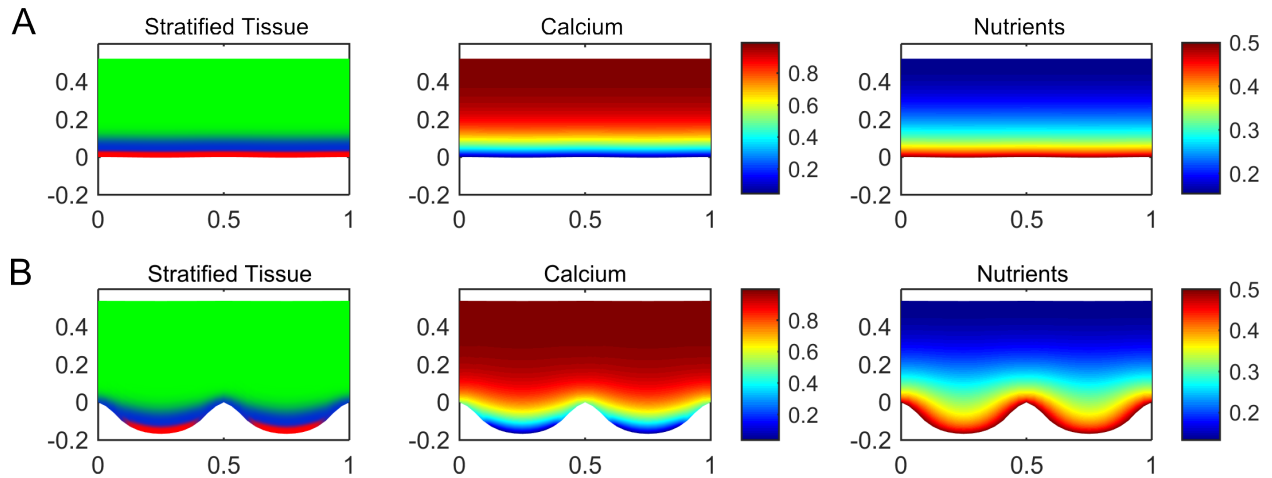
Figure 1.3: Tissue stratification and Morphogen gradients. Model simulation showing the spatial dynamics of morphogens and their regulations on self-replication leads to formation of a stem cell niche and stratification of the tissue. In particular, the stem cell niche (red) resides along the basal lamina, and TA cells (blue) reside near the bottom of the tissue as well, with TD cells (green) occupying the upper regions of the tissue. Such spatial organization is partly controlled by the formation of a calcium gradient which can leak through the basal lamina and has a no flux boundary condition along the apical layer. The tissue size is party controlled by the nutrients supplied by the dermis available. A gradient is formed which is high near the basal lamina and deceases nearer the apical boundary.
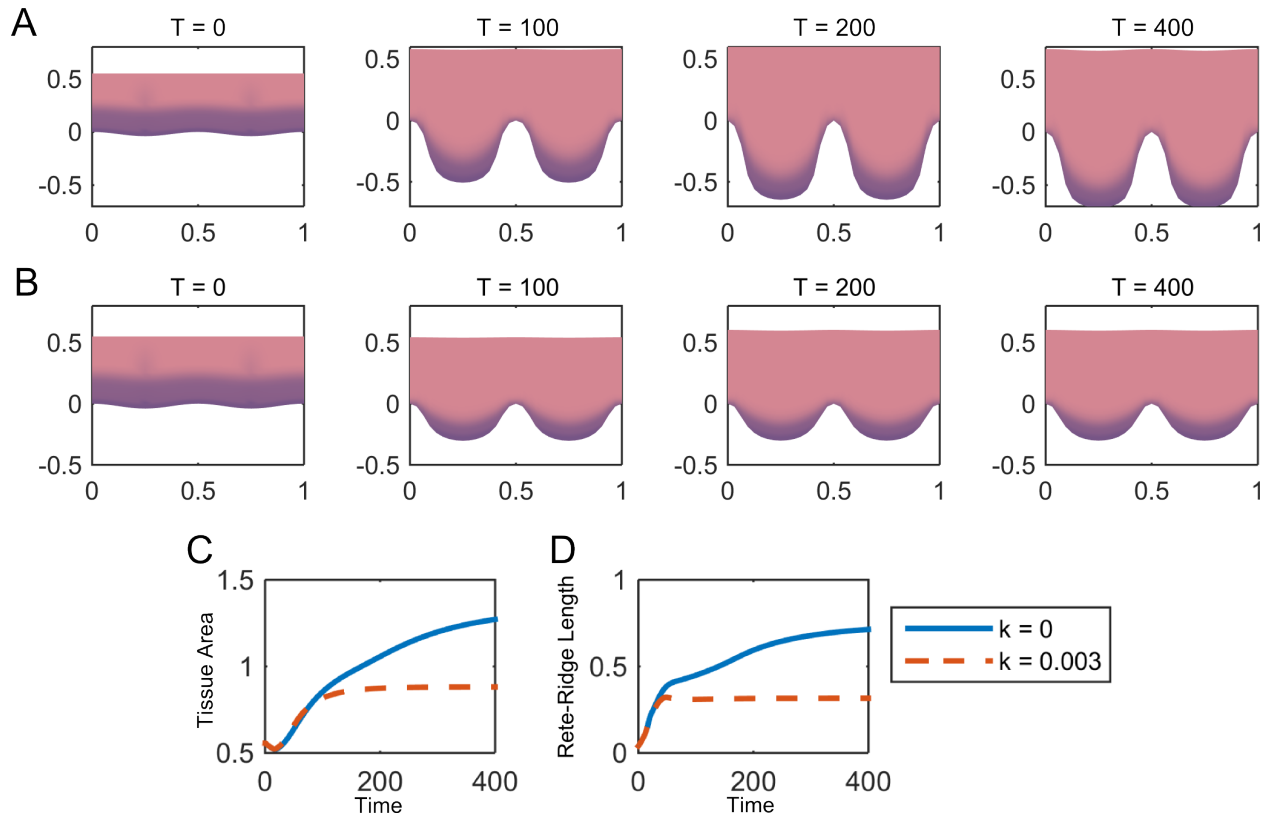
Figure 1.4: Dermis pressure allows tissue to achieve steady state (eq. (1.11)). A) Simulations showing that without a compressive force from the dermis ($k = 0$) along the epidermis-dermis junction, the rete-ridges formed will continue to elongate. B) Simulations showing that the addition of a compressive force from the dermis ($k = 0.003$) allows the tissue to reach a steady state. C) and D) Variation in tissue area and rete-ridge length over time.
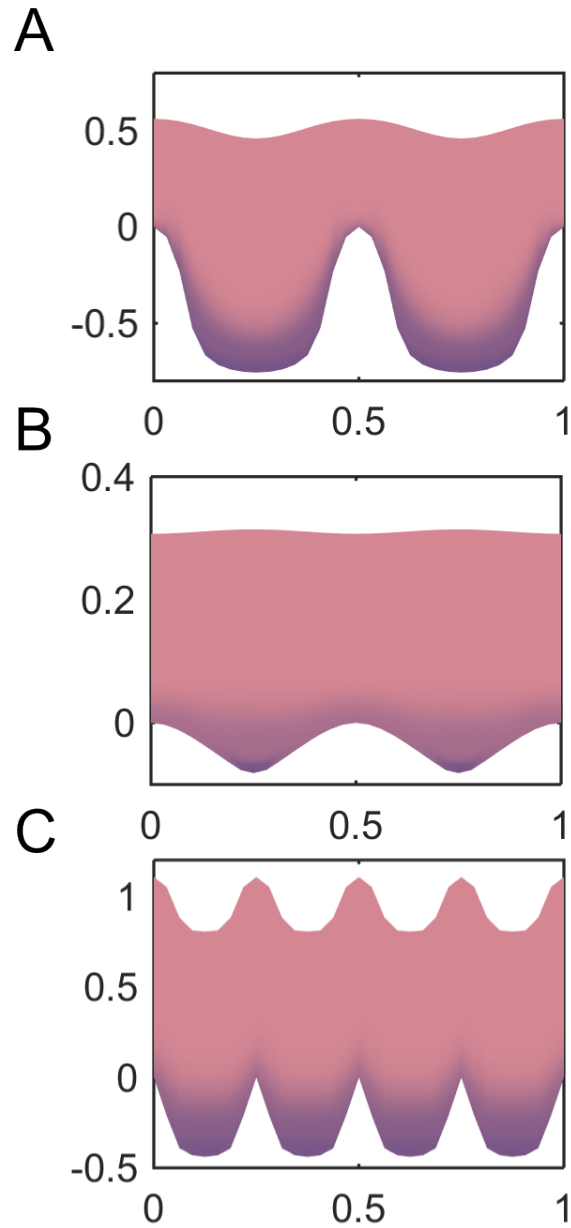
Figure 1.5: Model simulations of biological tissue morphologies found in oral epithelium [1]. With two dynamic boundaries, a large variety of stratified epithelial morphologies can be modeled. In this figure we show (A) Gingiva, a masticatory epithelia which has large, thick rete-ridges, (B) the inner lip tissue, which is a lining epithelia and is thin with almost no protrusions into the dermis, and (C) a specialized epithelia found on the dorsal part of the tongue, which has papillae protrusions on the apical surface.
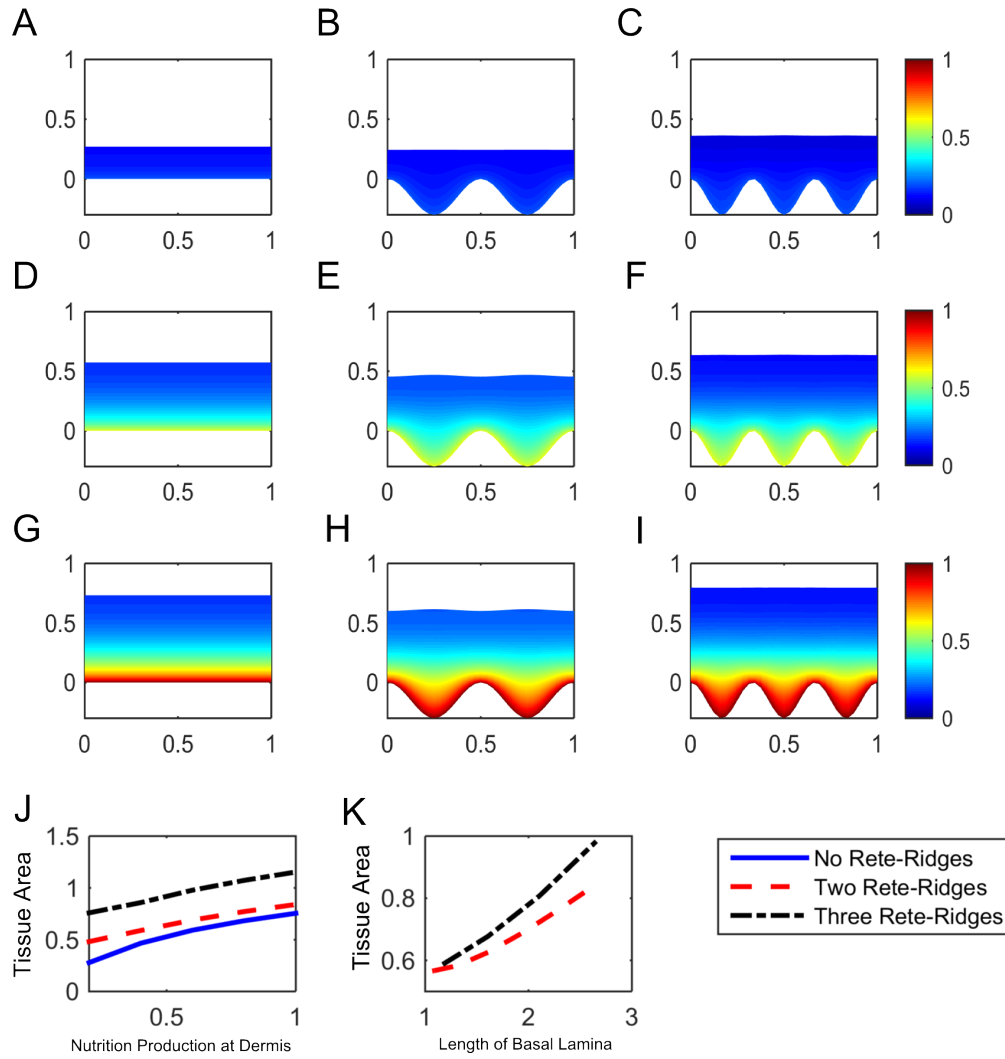
Figure 1.6: (A-I) Simulated steady-state tissue sizes with differing amounts of Nutrition produced by the dermis, as well as different number of rete-ridges formed. Colorbar shows the concentration of nutrition ([N]) (J) Steady state tissue area as a function of [N] produced at the dermis. (K) Steady state tissue area as a function of length of the basal lamina.
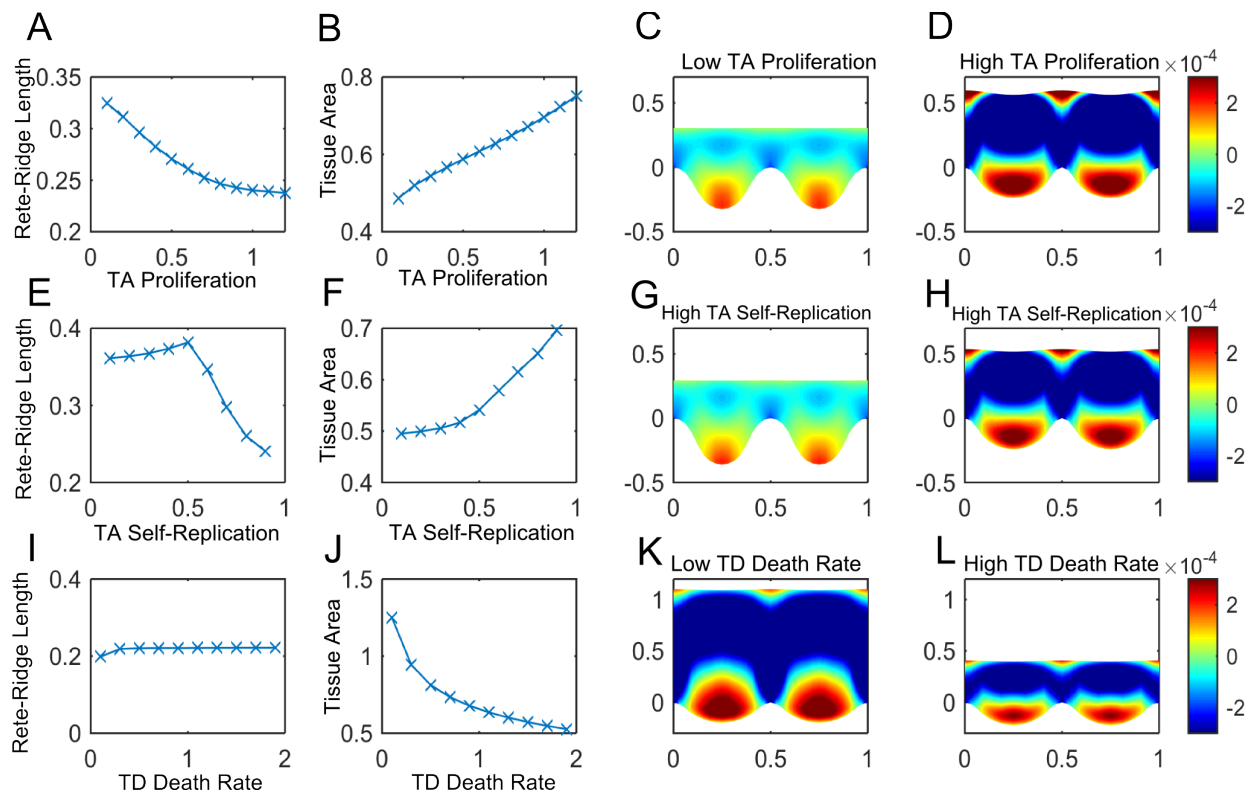
Figure 1.7: (A,B) An increase in the proliferation rate of TA cells (ν_1) decreases the rete-ridge length of the tissue and increases the area of the tissue. (C,D) Internal pressure of the tissues for low proliferation rare ($\nu_1 = 0.2$) and for high proliferation rate ($\nu_1 = 1.2$). (E) Cell replication probability (p_1) correlates positively with rete-ridge length when $p_1 < 0.5$ and negatively when $p_1 > 0.5$. (F) An increase in p_1 increases the tissue area regardless of if p_1 is greater than or less than 0.5. (G,H) Internal pressure of the tissue for low self-replication probability ($p_1 = 0.2$) and high self-replication probability ($p_1 = 0.9$). (I) Apoptosis of TD cells (d_2) has little effect on rete-ridge length and shape. (J) However, a decrease in cell death increases the area of the tissue, resulting in a thinner tissue. (K,L) Internal pressure of the tissue for low apoptosis ($d_2 = 0.1$) and high apoptosis ($d_2 = 2$).
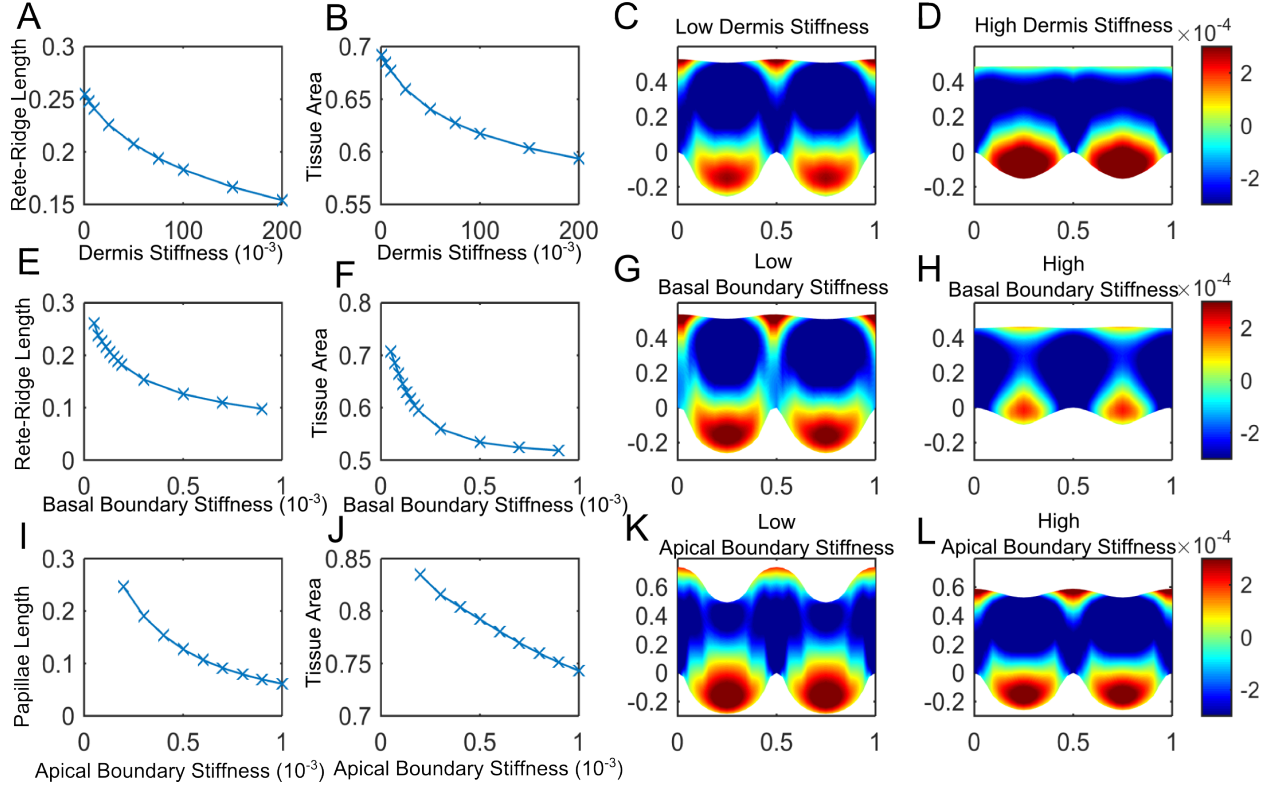
Figure 1.8: (A,B) Simulations changing the stiffness of the dermis (eq. (1.6)) shows that a stiffer, non-compliable dermis will decrease the rete-ridge length as well as the tissue area. (C,D) The internal tissue pressure shows that a lower dermis stiffness ($k = 10e-3$) will allow the rete ridge to come into equilibrium with a lower internal tissue pressure, while when the dermis is stiff ($k = 200e-3$) the tissue will have a much higher internal tissue pressure at steady state. (E, F) An increase in basal boundary stiffness (ξ_0) decreases the rete-ridge length and decreases tissue area. (G, H) Internal tissue pressure of low basal boundary stiffness ($\xi_0 = 1e-4$) and high basal boundary stiffness ($\xi_0 = 9e-4$). (I,J) Simulations changing the stiffness of the apical boundary show that papillae are able to form, and increase in size as apical boundary stiffness decreases. This formation also results in a slight increase in tissue size. (K,L) Internal tissue pressure show that papillae formation occurs adjacent to the location of rete-ridges in the x-spatial direction, where pressure at the apical boundary is highest. Simulations of (K) and (L) use parameters $\xi_1 = 0.2e-3$ and $\xi = 1e-3$.
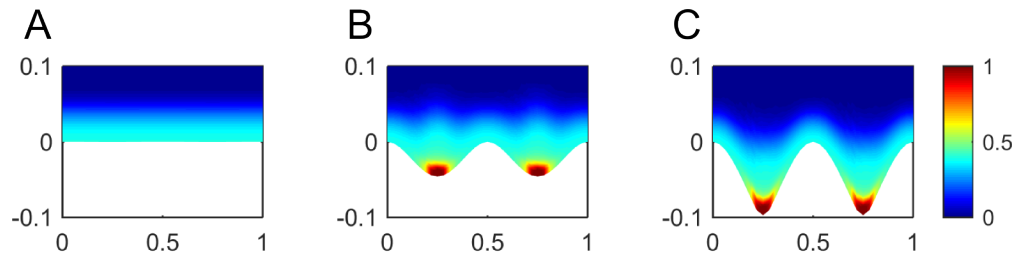
Figure 1.9: (A) A tissue with a high basal boundary stiffness is unable to form rete-ridges. (B) Pruduction of a morphogen A by SC in high pressure locally weakens boundary stiffness and allows formation of small rete-ridges (C) Morphogen A weakens boundary stiffness as well as increases the flux of morphogen Ca out of the epidermis, increasing the size of rete-ridges formed. Colorbar shows concentration of morphogen A.
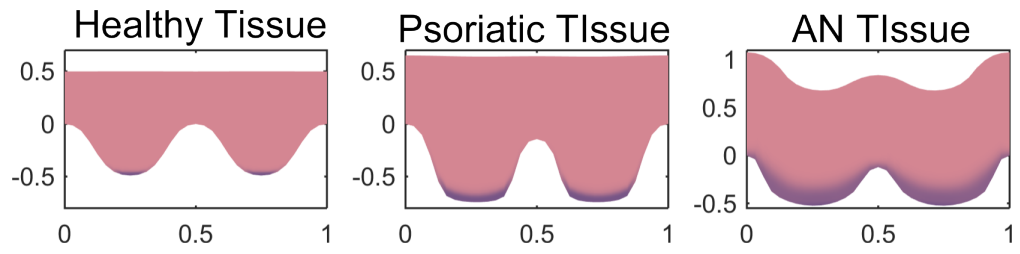
Figure 1.10: Simulations of a healthy tissue, a psoriatic tissue, and an Acanthosis Nigricans Tissue.

Table 1.1: Errors and orders of accuracy for calculations of the internal tissue pressure eq. (1.7), morphogen Ca eq. (1.27), and the calculations for tissue velocity due to pressure in both the x- and y-directions eq. (1.6), without time evolution. The boundaries are given by $h_1(x) = 0.1 * \cos(2\pi x) + 1$, $h_0(x) = 0.1 * \sin(4\pi x)$ and an influx of cells of $\psi = 1$. Parameters chosen for solving the internal pressure are $K = 1$, $\xi_1 = \xi_0 = 1e-5$. Parameters chosen for solving the morphogen are $\nabla Ca \cdot \hat{n}|_{y=h_1} = \nabla Ca \cdot \hat{n}|_{y=h_0} = -200$, $D_{Ca} = \mu_j = 1$, $a_{deg} = 0.1$, $\beta_j = 0$. Parameters chosen for solving the velocity due to pressure are $K = 1$, $P = \cos(2*pi*x)\sin(2*pi*y)$. Parameters $\omega = 1.25$ is chosen for all simulations

	Pressure		Ca		Velocity x		Velocity y	
N	Error	Order	Error	Order	Error	Order	Error	
8	--	--	--	--	--	--	--	--
16	1.34 e-2	--	9.15 e-3	--	2.74	--	2.48	--
32	0.27 e-2	2.34	1.43 e-3	1.67	4.19 e-1	2.71	3.58 e-1	2.79
64	6.28 e-4	2.08	5.15 e-4	1.47	7.82 e-2	2.42	5.84 e-2	2.62
128	1.55 e-4	2.02	1.32 e-4	1.96	1.78 e-2	2.14	1.47 e-2	1.99
256	3.86 e-5	2.00	2.85 e-5	2.22	4.33 e-3	2.04	3.67 e-3	2.00

Table 1.2: Errors and orders of accuracy for calculations of the internal tissue pressure eq. (1.7), and the kinematic boundary conditions eq. (1.12), with time evolution. The simulations are run until a final time of $t = 6.25e - 2$. The boundaries are given by $h_1(x) = 0.1 * \cos(2\pi x) + 1$, $h_0(x) = 0.1 * \sin(4\pi x)$ and an influx of cells of $\psi = 1$. Parameters chosen for solving the internal pressure are $K = 1$, $\xi_1 = \xi_0 = 1e - 5$, $\omega = 1.25$ and $\Delta\tau = \Delta x^2$

N	Pressure		h_0		h_1	
	Error	Order	Error	Order	Error	
8	--	--	--	--	--	--
16	2.12 e-2	--	2.21 e-5	--	2.82 e-2	--
32	6.22 e-3	1.77	1.19 e-5	0.89	4.41 e-3	2.68
64	1.34 e-3	2.12	2.04 e-6	2.55	9.61 e-4	2.20
128	2.95 e-4	2.18	4.56 e-7	2.16	2.29 e-4	2.07
256	6.87 e-5	2.10	1.18 e-7	1.95	4.79 e-5	2.26

Table 1.3: Errors and orders of accuracy for calculations of the internal tissue pressure eq. (1.7), and the kinematic boundary conditions eq. (1.12), with time evolution. The simulations are run until a final time of $t = 6.25e-2$. The boundaries are given by $h_1(x) = 0.1 * \cos(2\pi x) + 1$, $h_0(x) = 0.1 * \sin(4\pi x)$ and an influx of cells of $\psi = 1$. Parameters chosen for solving the internal pressure are $K = 1$, $\xi_1 = \xi_0 = 1e-5$, $\omega = 1.25$ and $N = 128$

	Pressure		h_0		h_1	
Δt	Error	Order	Error	Order	Error	
1 e-2	--	--	--	--	--	--
5 e-3	2.16 e-4	--	9.84 e-7	--	2.01 e-7	--
2.5 e-3	4.40 e-5	2.29	2.56 e-7	1.94	3.51 e-8	2.52
1.3 e-3	1.01 e-5	2.13	5.08 e-8	2.33	7.51 e-9	2.23
6.25 e-4	2.41 e-6	2.07	1.28 e-8	1.98	1.74 e-9	2.11
3.13 e-4	5.88 e-7	2.03	3.14 e-9	2.03	4.22 e-10	2.05
1.56 e-4	1.45 e-7	2.02	7.76 e-10	2.02	1.04 e-10	2.02

Table 1.4: Errors and orders of accuracy for calculations of epithelial growth and stratification. The simulations are run until a final time of $t = 6.25e-2$, with $\Delta\tau = \Delta x^2$. Parameters chosen can be found in table (REF TABLE) in the appendix.

	Pressure		C_0		Ca	
N	Error	Order	Error	Order	Error	
8	--	--	--	--	--	--
16	8.56 e-4	--	2.98 e-3	--	1.71 e-2	--
32	1.85 e-4	2.21	4.88 e-4	2.61	4.32 e-3	1.98
64	4.51 e-5	2.04	1.24 e-4	1.98	1.34 e-3	1.69
128	1.12 e-5	2.01	4.93 e-5	1.33	4.77 e-4	1.49
256	2.81 e-6	2.00	1.32 e-5	1.93	1.39 e-4	1.78

Chapter 2

A Multi-Regulatory Feather Model for Diverse Feather Shapes

2.1 Background

Over the last two decades, spectacular palaeontological discoveries, mainly from China, have revolutionized our understanding in the origin and evolution of feathers [74, 75, 76, 77, 78, 79, 80, 81]. Major novel functions of feathers that evolved include endothermy, communication, aerodynamic flight and so on. These are achieved through stepwise retrofitting of the original feather forms [74, 75, 76, 80, 81].

The three major transformative events that occurred during feather shape evolution are: (i) singular cylindrical filaments to periodically branched feathers; (ii) radially symmetric feathers to bilaterally symmetric feathers by developing mirror-imaged vanes separated by a central shaft (rachis) and (iii) symmetric or asymmetric alterations of vane shapes, including the innovation of feathers specialized for flight. Previous comparative analysis of flight feather (remige) shapes in a variety of birds indicates a strong association between the

level of vane asymmetry and flying ability [82]. These feathers serve as mini-airfoils that can generate lift. The co-localization of the center of gravity and the center of the lifting force in these feathers make the birds more stable in the air. These feathers also facilitate unidirectional pass-through of air during flapping. Additionally, they can separate from each other to minimize wind resistance [82, 83, 84, 85, 86]. Besides these major transformative events, other morphologic features that emerged during evolution include the deep follicles containing stem cells for cyclic regeneration[80], the hooklets and curved flanges in barbules and the solid cortex and air-filled pith in rachis and ramus[87]. Together, these features enhanced feather mechanical strength, reduced weight, improved air-trapping efficiency and ensured renewability of feathers after damage.

In the past, efforts have been made to unveil the patterning rules and molecular circuitry generating different feather forms. For the previously mentioned transformative event (i), BMP and its antagonist, NOGGIN, were shown to regulate branching periodicity [88]. An activator/inhibitor periodic-branching (PB) model was further used to explain how branching morphogenesis occurs autonomously by interactions of diffusible morphogens in the epithelium [89]. For event (ii), feather stem cells were found to exhibit a ring configuration, horizontally placed in downy feathers but tilted downward anteriorly (rachis side) in bilaterally symmetric feathers [14]. An anteriorposterior WNT3A gradient was shown to convert radial to bilateral feather symmetry. Flattening of the gradient converted bilaterally to radially symmetric feathers [90]. Yet for event (iii), it remains unclear how feather vane shapes are altered in different body regions (for example, symmetric body plumes vs asymmetric remiges along the wing), at different growth phases (for example, primary remiges of large flying birds have naturally occurring emarginated notches, meaning different vane widths at different phases of feather growth). Understanding of feather polymorphism at different physiological developmental stages (for example, natal down and adult plumes) and across different genders (for example, sail-shaped remiges occur in male but not female mandarin ducks) is also lacking. We believe studying the complex feather vane shapes in Aves provides

44

great opportunities to understand how systematic and environmental information are sensed and interpreted by skin appendage stem cells.

Here, through anatomic and computational analysis we found two morphological parameters highly associated with feather vane shape diversity: the topology of the barb generative zone (BGZ) and the insertion angles of barbs into the rachis. The BGZ is where the regularly spaced barbs initiate and hence it has also been called the new barb locus [91]. Morphologically it is thinner than the neighbouring epithelial regions, containing irregularly spaced small branches. Eventually it disintegrates to allow vanes to separate and the feather cylinder to open up upon feather maturation.

Through transcriptome profiling and functional perturbations, we identify mesenchyme (pulp) derived GDF10 and GREM1 as key regulators for rachis and BGZ topology, respectively. They function by modulating BMP signalling in adjacent epithelium. The interaction between WNT signalling, GDF10 and GREM1 establishes the symmetric vane configuration. Additionally, differentially localized CYP26B1, CRABP1 and RALDH3 in the pulp establish anisotropic RA signalling. This modulates GREM1 expression and epithelial cell shapes which then adjusts BGZ topology and the barb-rachis angle, resulting in alterations of vane width and symmetry. Thus the co-option of multi-scale mesenchymal signalling modules by feather epithelial progenitor cells likely drives vane shape diversification

2.2   Experimental Observations

Analysis of feather morphology was conducted on rooster remiges with different asymmetry levels (primary and secondary remiges) and body plumes with different vane widths (dorsal and breast plumes). Before feather maturation, the pulp (considered to be the source of nutrition during growth) is en-wrapped by epithelium. This, in turn, is wrapped inside the feather sheath which gives the feather primordium a cylinder conformation. Upon maturation the pulp retreats and the BGZ disintegrates, allowing the vanes to separate (fig. 2.1).

A morphological parameter associated with vane shape variation is the barb-rachis angle. Measurement show that narrower vanes have a statistically significant smaller helical growth angle, while barb length remains relatively similar. This was true for both body plumes and wing plumes.

Another morphological difference between vanes was the width of the BGZ. Experiments show the width of the BGZ is inversely correlated with the width of the vanes. For asymmetric remiges, higher asymmetry levels are associated with a larger BGZ that expands toward the lateral side, restricting the epithelial area for lateral vane formation. For symmetric body plumes, narrower vanes are associated with a larger BGZ which expands in both lateral and medial directions.

Crucial molecular regulators of vane shape were identified through RNA-seq. Analysis indicated that GDF10, a BMP family member, is downregulated in the pulp of lateral side primary remiges and dorsal plumes. In situ hybridization unveiled highly localized GDF10 expression in the pulp adjacent to the rachis. RNA-seq also indicated that the BMP antagonists, GREM1, is upregulated in the pulp of lateral side primary remiges and dorsal plumes. In situ hybridization demonstrated localized GREM1 expression in the pulp adjacent to the BGZ. Similar expression patterns of GDF10 and GREM1 were also seen in zebra finch and Japanese quail remiges.

The differential localization of Retinoic Acid (RA) regulators, CYP26b1 and CRABP1 in asymmetric remiges implies a potential link between the RA gradient and vane asymmetry. In symmetric feathers CRABP1 and CYP26b1 had homogeneous expression. Wide symmetric vanes had high Crabp1 and low CYP26b1, while narrow symmetric vanes had low CRABP1 and high CYP26b1. Furthermore, downregulation of RA signaling decreases feather vane widths and results in significantly sharper barb-rachis angles. In asymmetric plumes, CRABP1 and CYP26b1 had opposing medial-lateral gradients. In situ hybridization of RA related factors in different types of feathers implies an association between increased RA levels and decreased GREM1 expression, therefore, we hypothesize RA signalling works upstream to inhibit GREM1 expression.

2.3   A Multi-Module Regulatory Model

To better understand the molecular regulation of feather vane shapes we turned to mathematical modeling. The cylindrical growing domain of the feather is modeled as a one dimensional spatial domain with periodic boundary conditions. Here, the molecular interplay is solved using a series of ordinary and partial differential equations. The circular domain grows downward in time to represent the proliferation of new cells pushing the previous cells upward during development.

Our new Multi-Module Regulatory Feather (MRF) model includes the new experimental findings on on GDF10, GREM1, RA and WNT signaling. In the MRF model the concentration of extra-cellular diffusible RA is represented by $[RA_o]$, diffusible WNT by $[WNT]$, diffusible GDF10 by $[GDF]$ and diffusible GREM1 by $[GREM]$. The concentrations of non-diffusible molecules are similarly represented, intracellular RA by $[RA_i]$, CRABP1 by $[BP]$, CYP26B1 by $[CYP]$ and RA receptors by $[R]$. $[RA_i]$ bound with $[R]$ forms the complex $[RAR]$, which we use as an RA signal, and $[RA_i]$ bound with $[BP]$ forms the complex $[RABP]$, eqs. (2.1) to (2.6). The interactions between RA_o, RA_i, BP, CYP and R are based on a previous zebrafish model [92], with the WNT, GDF and $GREM$ interactions added based on our experimental result eqs. (2.7) to (2.9).

$$\frac{\partial[RA_o]}{\partial t} = D_{RA_o}\frac{\partial^2[RA_o]}{\partial x^2} + V_{RA_o}\left(B_{RA_o} + \frac{1}{1 + \left(\frac{k_1}{[WNT]}\right)^{n_1}}\right)$$

$$- (1+\beta)\,k_p[RA_o] + k_p[RA_i] \tag{2.1}$$

$$\frac{\partial[RA_i]}{\partial t} = k_p[RA_i] + r_{R2}\,[RAR] + r_{BP2}\,[RABP] - r_{RA_i1}[CYP][RA_i] - k_p[RA_i]$$

$$- k_{on}[RA_i]\,[R] + k_{off}\,[RAR] - m_{on}[RA_i]\,[BP] + m_{off}[RABP] \tag{2.2}$$

$$\frac{\partial[R]}{\partial t} = V_R - r_{R1}\,[R] - k_{on}[RA_i]\,[R] + k_{off}\,[RAR] - j_\alpha\,[RABP]\,[R] + j_\beta\,[BP]\,[RAR] \tag{2.3}$$

$$\frac{\partial[RAR]}{\partial t} = k_{on}[RA_i]\,[R] - k_{off}\,[RAR] + j_\alpha\,[RABP]\,[R] - j_\beta\,[BP]\,[RAR] - r_{R2}\,[RAR] \tag{2.4}$$

$$\frac{\partial[BP]}{\partial t} = V_{BP}\,(x) - r_{BP1}\,[BP] + r_{RA_i2}\,[CYP]\,[RABP]$$

$$- m_{on}\,[RA_i]\,[BP] + m_{off}\,[RABP] + j_\alpha\,[RABP]\,[R] - j_\beta\,[BP]\,[RAR] \tag{2.5}$$

$$\frac{\partial[RABP]}{\partial t} = -\,r_{RA_i2}[CYP]\,[RABP] + m_{on}[RA_i]\,[BP] - m_{off}\,[RABP]$$

$$- j_\alpha\,[RABP]\,[R] + j_\beta\,[BP]\,[RAR] - r_{BP2}\,[RABP] \tag{2.6}$$

$$\frac{\partial[WNT]}{\partial t} = D_{WNT}\frac{\partial^2[WNT]}{\partial x^2} + V_{WNT}\,(x)\left(B_{WNT} + \frac{1}{1 + \left(\frac{k_2}{[GDF]}\right)^{n_2}}\right) - r_{WNT}[WNT] \tag{2.7}$$

$$\frac{\partial[GDF]}{\partial t} = D_{GDF}\frac{\partial^2[GDF]}{\partial x^2} + V_{GDF}\,(x)\left(B_{GDF} + \frac{1}{1 + \left(\frac{k_3}{[RAR]}\right)^{n_3}}\right) - r_{GDF}[GDF] \tag{2.8}$$

$$\frac{\partial[GREM]}{\partial t} = D_{GREM}\frac{\partial^2[GREM]}{\partial x^2}$$

$$+ V_{GREM}\left(B_{GREM} + \frac{1}{1 + \left(\frac{k_4}{[RAR]}\right)^{n_4} + \left(\frac{k_5}{[WNT]}\right)^{n_5}}\right) - r_{GREM}[GREM] \tag{2.9}$$

Here, V_i, B_i, D_i and r_i are the maximum production rates, basal production rates, diffusion coefficients and the decay rates of molecule type $i(RA_o, RA_i, R, RAR, BP, RABP, WNT,$ $GDF, GREM)$, respectively. In some cases, a molecule can decay when it is both unbound and bound in a complex. Therefore, two decay rates are given: r_{BP1} and r_{BP2} for CRABP1 unbound and bound to RA, r_{R1} and r_{R2} for the RA receptor unbound and bound to RA, and r_{RA_i1} and r_{RA_i2} for RA_i unbound and bound to CRABP1. Parameters k_{on}, k_{off}, m_{on} and m_{off}, are on and off rates for complexes RAR and $RABP$. The rate at which RA in complex $[RAR]$ unbinds and binds with CRABP1 to form $[RABP]$is j_a, while the rate at which RA in complex $[RABP]$ unbinds and binds to RA receptors to form $[RAR]$ is j_b. Diffusible extracellular RA is modeled as entering the cell at rate k_p, and b is the proportion of RA lost from the system in this transition. Regulation of activation and inhibition between molecular species are regulated by Hill functions, where k_1, k_2, k_3, k_4 and k_5 are dissociation constants and n_1, n_2, n_3, n_4 and n_5 are Hill coefficients. Some maximum production rates, as well as the concentration of CYP26B1 are spatially dependent and are defined as follows:

$$x = [0, 1) \tag{2.10}$$

$$[CYP]_j = a_{cyp} * Exp[v_{cyp}(\sin(2\pi x) - 1)] + B_{CYP} \tag{2.11}$$

$$V_{BP}(x) = a_{bp} * Exp[v_{bp}(\sin(2\pi(x + 0.5)) - 1)] + B_{BP} \tag{2.12}$$

$$V_{WNT}(x) = a_{wnt} * Exp[v_{wnt}(\cos(2\pi(x + 0.5)) - 1)] \tag{2.13}$$

$$V_{GDF}(x) = a_{gdf} * Exp[v_{gdf}(\cos(2\pi(x + 0.5)) - 1)] \tag{2.14}$$

Here, a_i is a scaling coefficient and v_i defines the slope of the gradient formed for molecule type $i(CYP, BP, WNT, GDF)$.

The formation of the barbs which make up feather vanes is modeled using a Periodic Branching (PB) model. The PB model is based on a previous activatorinhibitor model [89], where a slow diffusing, self-regulating activator (A), activates a fast diffusing inhibitor (B) and a non-diffusible inhibitor (C). Both inhibitors B and C downregulate activator A. Recent evidence suggests that BMP may act as the fast diffusing inhibitor in feather development. The $[GREM1]$ and $[GDF10]$ steady state profiles formed in the MRF model are incorporated in the PB model through inhibiting B downregulation of A, and upregulating basal production of B, respectively eqs. (2.15) to (2.17).

$$\frac{\partial [A]}{\partial t} = D_A \frac{\partial^2 [A]}{\partial x^2} + \frac{\left([A]^2 + b_A\right)}{s \left(1 + s_A [A]^2\right) \left(\frac{s_B [B]}{1 + (s_G/[GREM])^{nG}} + s_C [C]\right)} - r_A [A] \tag{2.15}$$

$$\frac{\partial [B]}{\partial t} = D_B \frac{\partial^2 B}{\partial x^2} + r_A [A]^2 + b_B [GDF] - r_B [B] \tag{2.16}$$

$$\frac{\partial [C]}{\partial t} = b_C [A]^2 - r_C [C] \tag{2.17}$$

The concentration of activator A is represented by $[A]$, inhibitors B and C by $[B]$ and $[C]$, Grem1 by $[GREM]$ and GDF10 by $[GDF]$. Here, D_A and D_B are the diffusion coefficients of A and B, r_A, r_B and r_C are decay rates of A, B and C. Parameter s modulates the maximum auto-catalytic reaction of A, s_A, s_B, s_C and s_G are saturation coefficients, b_A and b_B are the basal production of A and B, while b_C modulates the maximum production of C. n_G is a Hill coefficient. Parameters for all simulations can be found in Appendix B.

2.4 Mechanisms Regulating Barb-Rachis Helical Angle

From the unfolding cylinder in fig. 2.1 we can see that the helical barb-rachis angle (θ) during growth may be influenced by the proximal-distal growth rate of the feather, i.e. how quickley the feather propagates upward, as well as the propagation speed of the traveling waves around the feather collar. We theorize that the helical angle can be calculated by a trigonometric relationship between the traveling wave speed and the proximal-distal growth rate (eq. (2.18)).

$$\theta = \arctan\left(\frac{W}{V}\right) \tag{2.18}$$

We first explored the effect on helical angle due to a change in the P-D growth rate of the feather. We found that by increasing this growth rate the helical angle became more narrow (fig. 2.3 A). Since no other parameters in the model were altered, the speed of propagation of the activator remained constant, meaning all change in helical angle is due to the change in the growth rate. In order for P-D growth rate to alter helical angle there needs to be a way in which the tissue can control its growth rate. Several possibilities exist: cell proliferation rate can be changed, the volume to which the cell grows can be changed, or the proximal-distal length of the cell can be changed.

We looked at the varying components of the PB model and tested how changes in parameter values altered the feather form and found that the largest change in helical angle occurred due to changes made to the diffusivity of the activator (fig. 2.3 B). While other parameters were able to change the helical angle by a few degrees, the change in activator diffusivity gave the largest range of possible helical angles formed. The change in helical angle is due to the propagation of the activator wave speed. We can intuitiviley deduce why increasing

the diffusivity of the activator increases the traveling wave speed. As a peak of activator increases, it diffuses outward upregulating the activator concentration in neighboring cells. The faster the diffusion of the activator, the sooner it activates a neighboring cell. Since the inhibitor does not turn on until after the activator has reached a certain threshold, it lags behind the activator, unable to speed up or slow down the propagating wave (fig. 2.3 C). With the P-D growth rate kept constant, a faster traveling wave means that the barbs formed at the BGZ reach the rachis quicker and thus form shorter vanes with wider angles.

Interestingly, epithelial cells (especially those in BGZ regions) in growing remiges of narrow feathers have a more elongated appearance (in the proximaldistal direction) than those of wider vanes. A similar situation is also seen in feather epithelial cells exposed to different endogenous RA levels. We hypothesize that proximal-distal cell elongation would increase the P-D growth rate (provided cell proliferation rates remain unchanged) thereby reduce the helical growth angle according to eq. (2.18).

A second potential mechanisms through which cell shapes can affect the helical growth angle is through altering the tissue tortuosity. It has been noted that diffusivity can be affected through the tortuosity of the system's medium [93]. Assuming diffusion of the molecule is quickest through the ECM and not through cell cytoplasm, then tissue architecture, which is affected by the size, shape and arrangement of cells, can affect tissue tortuosity [94]. Tortuosity is described by λ and is defined by the length of the shortest possible path between two points that a molecule can travel through divided by the straight line distance between the two points (eq. (2.19)). In effect, by forcing the particle to take a longer path to get to the same destination, its transport speed has been slowed down. Since the PB model relies on diffusion as a main transport mechanism, increasing tortuosity results in a decrease in diffusivity (eq. (2.20)) and thus a decrease in barb-rachis angle. A change in tissue tortuosity could account for the discrepancy between the predicted angle and the observed angle found when changing only the P-D growth rate of the feathers. One reason

is that diffusivity being inversely proportional to the square of tortuosity, so a small change in tortuosity can result in a large change in diffusivity. Through image analysis, outlined the cell shapes of two feathers, a wide vaned breast plume and a narrow vaned dorsal plume. We calculated the tortuosity of each tissue by randomly generating two points within the tissue and calculating the shortest path around the cells between them fig. 2.4. This was done 2000 times for each tissue. The tortuosity of the breast plume was found to be $\lambda_B = 1.13 \pm 0.04$, and for the dorsal plume $\lambda_D = 1.61 \pm 0.4$. This results in the breast plume having a diffusivity twice that of the dorsal plume.

$$\lambda = \frac{L}{C} \tag{2.19}$$

$$D^\star = \frac{D}{\lambda^2} \tag{2.20}$$

2.5 Anisotropic RA Signaling Modulates Vane Width

We used the MRF model to explore the landscape of RA and its effect on vane width modulation. We first explore a simpler MRF model with no RA module. In this case RA, CRABP1 and CYP26b1 are removed from the model leaving only the interaction between WNT, GDF and GREM2. The model is able to produce a rachis with extremely short vanes (fig. 2.5), predicting that early feathers found in dinosaurs which may not have expressed RA signaling were possible. It also shows that the anterior-posterior axis of the feather is regulated by opposing gradients of GDF, Wnt and GREM1, which supports evidence that a WNT gradient is responsible for the conversion of a radially symmetric feather (one in which no rachis is formed) to a bilaterally symmetric feather [90]. Simulations show that the addition of the RA module mediates the width of the feather vanes. Whereby high concentration of CRABP1 in conjunction with low concentrations of CYP26B1, produce a high level of RA signaling. This in turn downregulates the expression of GREM1 at the posterior end of the feather follicle, decreasing BGZ size. A high concentration of CYP26b1 and a low concentration of CRABP1 has the opposing effect, decreasing RA signaling. In turn, the BGZ expands due to a higher expression of GREM1 posteriorly, resulting in narrow feather vanes(fig. 2.5).

Furthermore, our model shows that RA signaling is the lateralmedial regulatory module, controlling the asymmetry between feather vanes fig. 2.6. Through opposing gradients of CYP26B1 and CRABP1 in the lateral-medial direction, an anisotropic landscape of RA is formed. This gradient of RA signaling shifts the size and position of the BGZ with respect to the rachis, forming a wide vane where RA signaling is high, and a narrow vane where RA signaling is low. Through incrementally changing the expressions of CRABP1 and CYP26B1 in the opposite direction, changes the slope of the RA gradient. A continuum of asymmetry levels can be produced. Such a continuum of asymmetry is commonly observed in a row of remiges along the the bird wing.

From here we move forward to examine how flight feathers retrogressed in diverse plumage of flightless birds. We explored the model to study if retrogressed morphology of ostrich and emu remiges are associated with altered expression patterns of the key molecular signals in the MRF model. We looked at a diverse set of plumes, including the ostrich remige, which has wide vanes and a narrow rachis, chicken breast feathers with after-plumes, and emu primary remige with dual rachis. The model shows that GDF10 is a crucial regulator of rachis width. An increase in RA signaling, which increases vane width through down regulation of GREM1, could result in a decrease in GDF. This increase in RA expression would be responsible for the ostrich plume morphology (fig. 2.7 C, G). Moreover, simulations show that a higher expression of GDF10 in the anterior side of the chicken after feather could cause the anterior after feather to have a larger rachis and vane than the posterior after feather, creating two feathers of asymmetric proportions(fig. 2.7 B,F). This asymmetry in the chicken after-feather would not be observed in emu primary remige, where CRABP1 epression is homogeneous(fig. 2.7 D, H). Finally, dual gradients of WNT signaling, one at the anterior and one at the posterior have been observed in feathers with dual rachis. Simulations show that activation of WNT signaling at the posterior side of the feather could induce additional rachis and vane formation (fig. 2.7 B, D, F, H).

2.6 Discussion

Organ shaping is a fundamental issue in development and critical in tissue engineering. In many cases organ shapes are influenced by signals arising both within and outside the organ. We believe the diverse feather vane shapes in modern birds provide a great opportunity to decipher the principles of morphogenesis and understand how stem cells can alter their behaviors in response to different environmental information.

Here we established a multi-module regulatory model revealing that the feather mesenchyme provides micro-environmental signals to tune the self-organized branching program of feather epithelial progenitors. First, branching of the feather epithelial cylinder requires interactions between activators and inhibitors. Second, GDF10 and GREM1 acted on inhibitor signaling to tune the branching process, leading to the establishment of Rachis and BGZ topology, respectively. Third, a WNT gradient coordinated the position of the rachis and BGZ through interactions with GDF10 and GREM1, which established the bilateral-symmetric vane configuration. Fourth, the anisotropic RA landscape, shaped by differential levels of CYP26B1 and CRABP1 over different body regions and time, introduced a new dimension of vane shape variations through crosstalk with GREM1 to adjust the BGZ topology (and potentially GDF10 to adjust rachis topology) and barb-rachis angles.

Differential RA signaling activities have been implicated as a key regulator of region-specific phenotypes. For example, RALDH2/ mouse embryos have been reported to show bilaterally asymmetric somitogenesis due to leftright desynchronization of segmentation clock oscillations [95]. Previous analyses of naked neck chickens revealed elevated RA in the neck potentiates BMP signalling, which inhibits feather formation [96]. Our findings here indicate GREM1 as a potential candidate to explain the potentiation effect of RA on BMP signalling. During limb development, RA forms a gradient for proximaldistal limb patterning [97], which is in the same direction as those in primary remiges. Therefore, it is possible that the limb

57

RA gradient is somehow imprinted within the remige pulp cells and the steepness of the limb RA gradient is used to establish a continuum of asymmetry levels in remiges along the wing.

Besides its effect on BGZ topology, RA signaling also modulates barb-rachis angles, which may further contribute to the diversification of vane shapes. We observe different feather epithelial cell shapes in feather vanes having different RA levels. Lower RA is associated with a more elongated cell shape in the proximaldistal direction. Through mathematical modeling we demonstrate two potential mechanisms through which cell shapes could affect helical growth angles. One is through the increase in feather growth rate, which would also result in increased barb lengths. The second is through cell shape altering the tortuosity of the feather tissue, affecting diffusivity of the activator and thus the propagation speed at which barbs form from the BGZ to the rachis.

In summary, our study here reveals a multi-module regulatory network in feather mesenchyme that facilitates the diversification of feather vane shapes through regulating the branching morphogenesis of feather epithelial progenitors. Such interactions between organ stem cells and their microenvironment are also observed in the development and regeneration of other organs. It would be intriguing to investigate how these microenvironment signals crosstalk with systematic signals, such as differential hormone levels in different genders, seasons and physiological developmental stages.

2.7   Figures
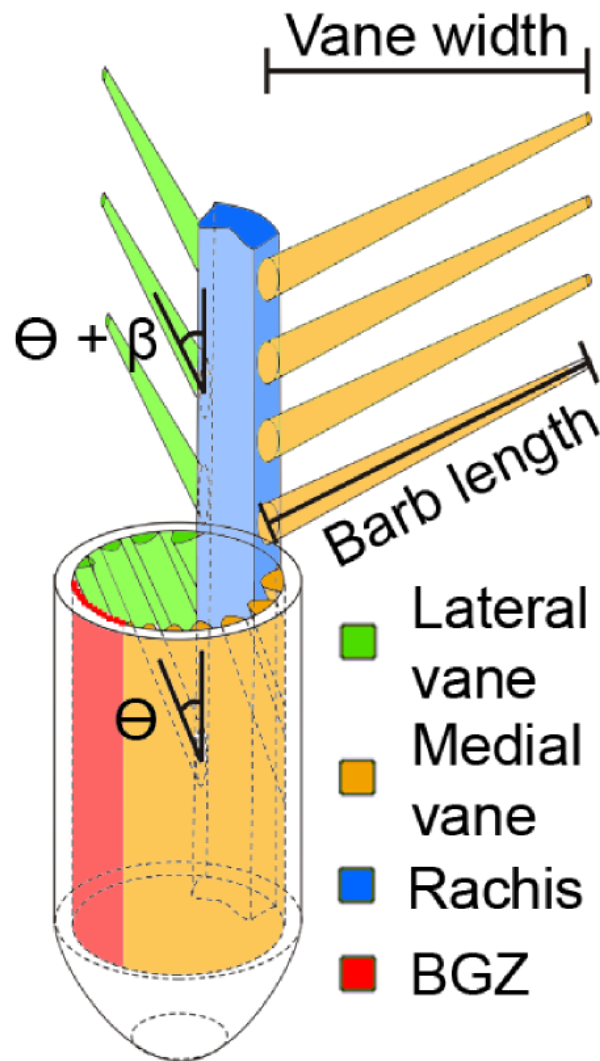
Figure 2.1: Schematic drawing of feather before and after maturation. The barb-rachis angle is a combination of the helical growth angle (θ) during branching morphogenesis and the expansion angle (β) after maturation. Feather barbs are generated at the Barb generative zone (BGZ) and propagate around the feather follicle toward the rachis.
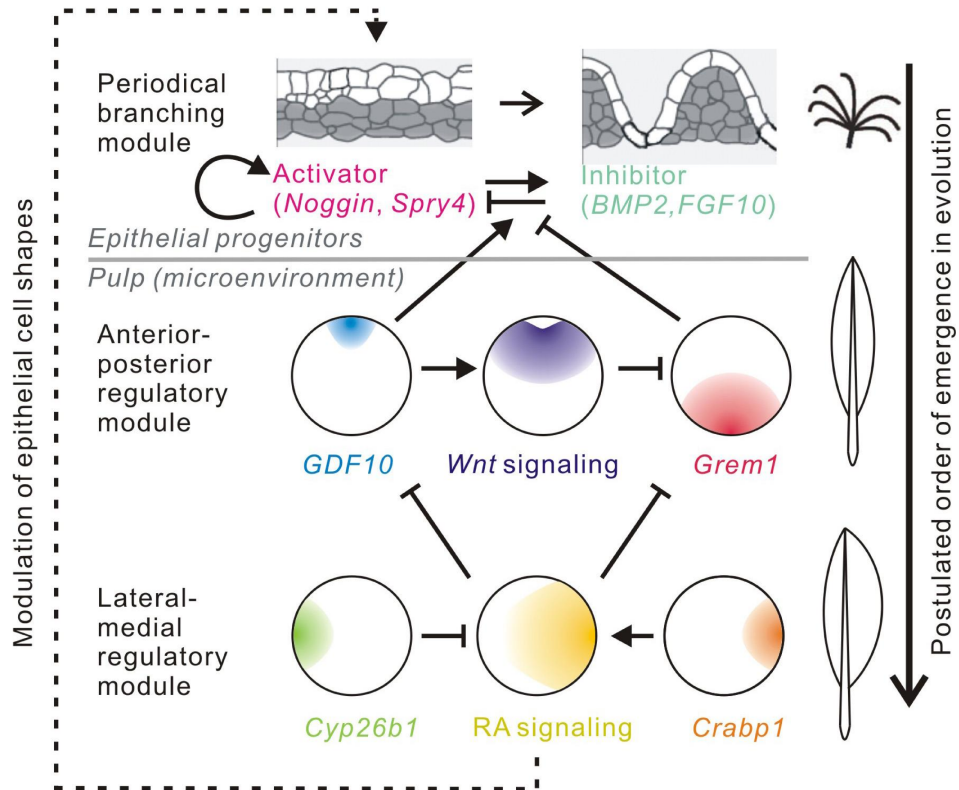
Figure 2.2: Schematic representation of the infrastructure of the multi-module regulatory feather (MRF) model and the corresponding transformative events of feather shapes in evolution. Dashed lines denote crosstalk relationships not fully confirmed.
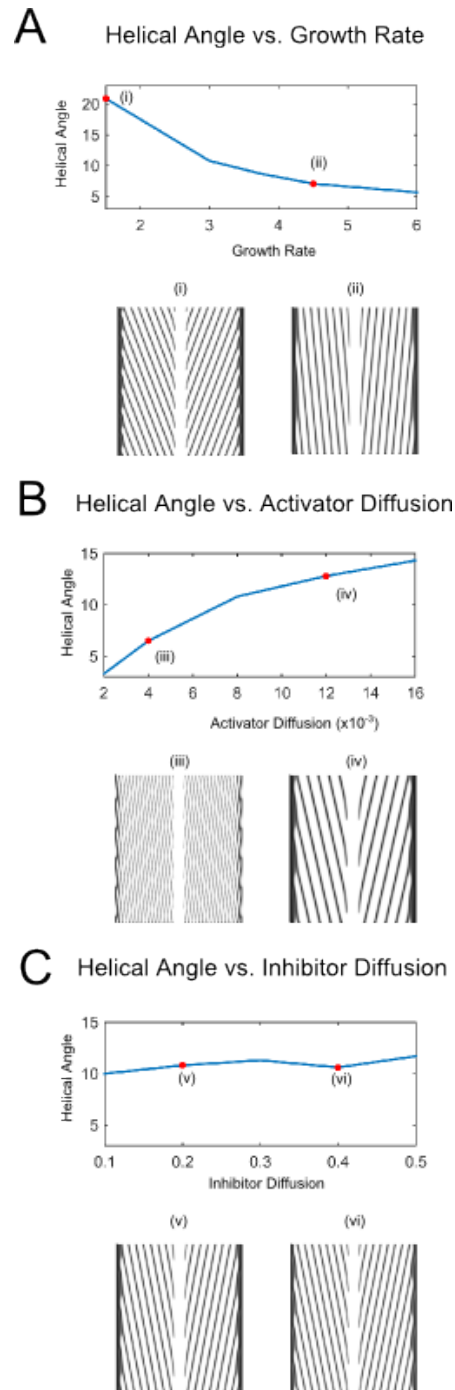
Figure 2.3: (A) Helical growth angle decreases with the increase of gross feather growth rate. Feather simulations of selected data points are also shown. Simulation angles are simulated using the Periodic Branching model. (B) Helical growth angle increases with the increase of activator's diffusivity. (C) Increasing inhibitor diffusivity only trivially alters helical growth angle.

61
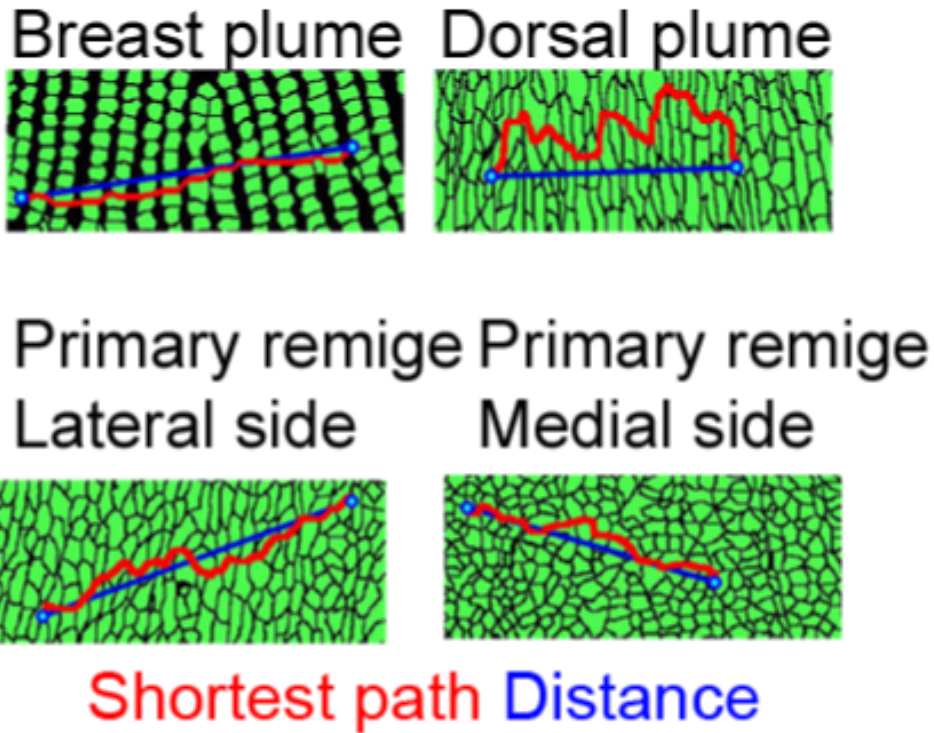
Figure 2.4: Differential epithelium tortuosity in different feathers. Red lines: shortest path around the cells; blue lines: the distance between two points. Tissue tortuosity is inversely correlated with activator/inhibitor diffusivity eq. (2.20).
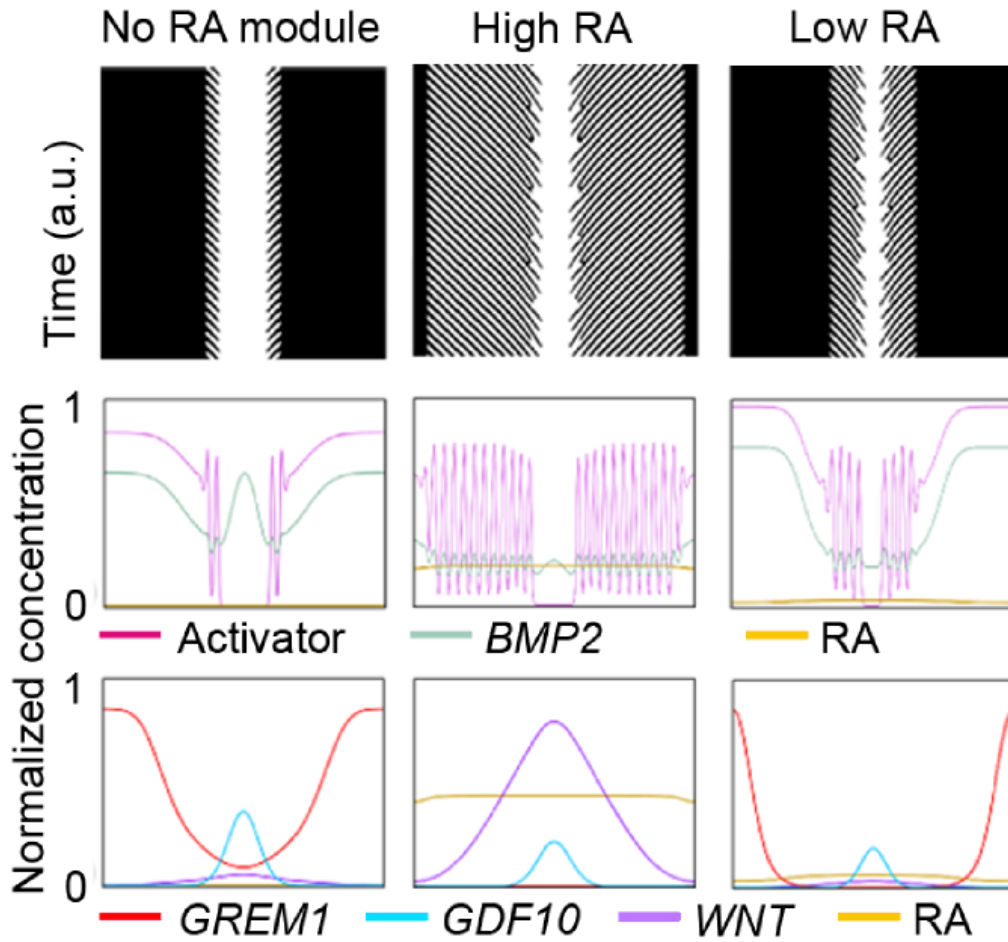
Figure 2.5: Representative simulations of vane shape variations using the MRF model either without RA module, with high RA (CRABP1 level set at 1.1, CYP26B1 at 0.02, arbitrary units), or with low RA (CRABP1 at 0.005, CYP26B1 at 0.2).
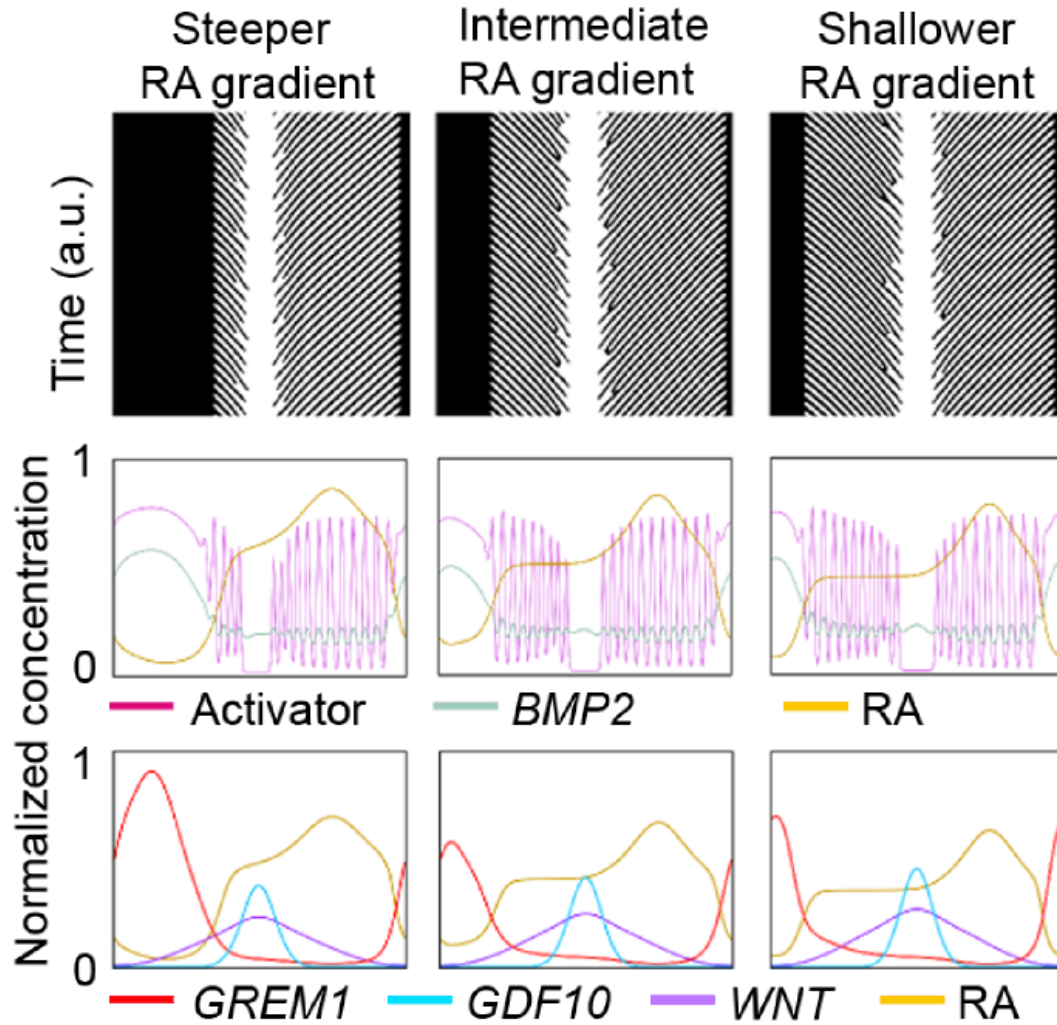
Figure 2.6: Representative simulations of feathers with different levels of vane asymmetry by changing the slope of RA gradient (CRABP1 at 0.006, CYP26B1 at 5 for the steeper RA gradient, CRABP1 at 0.03, CYP26B1 at 0.5 for the intermediate RA gradient, CRABP1 at 0.06, CYP26B1 at 0.3 for the shallower RA gradient)
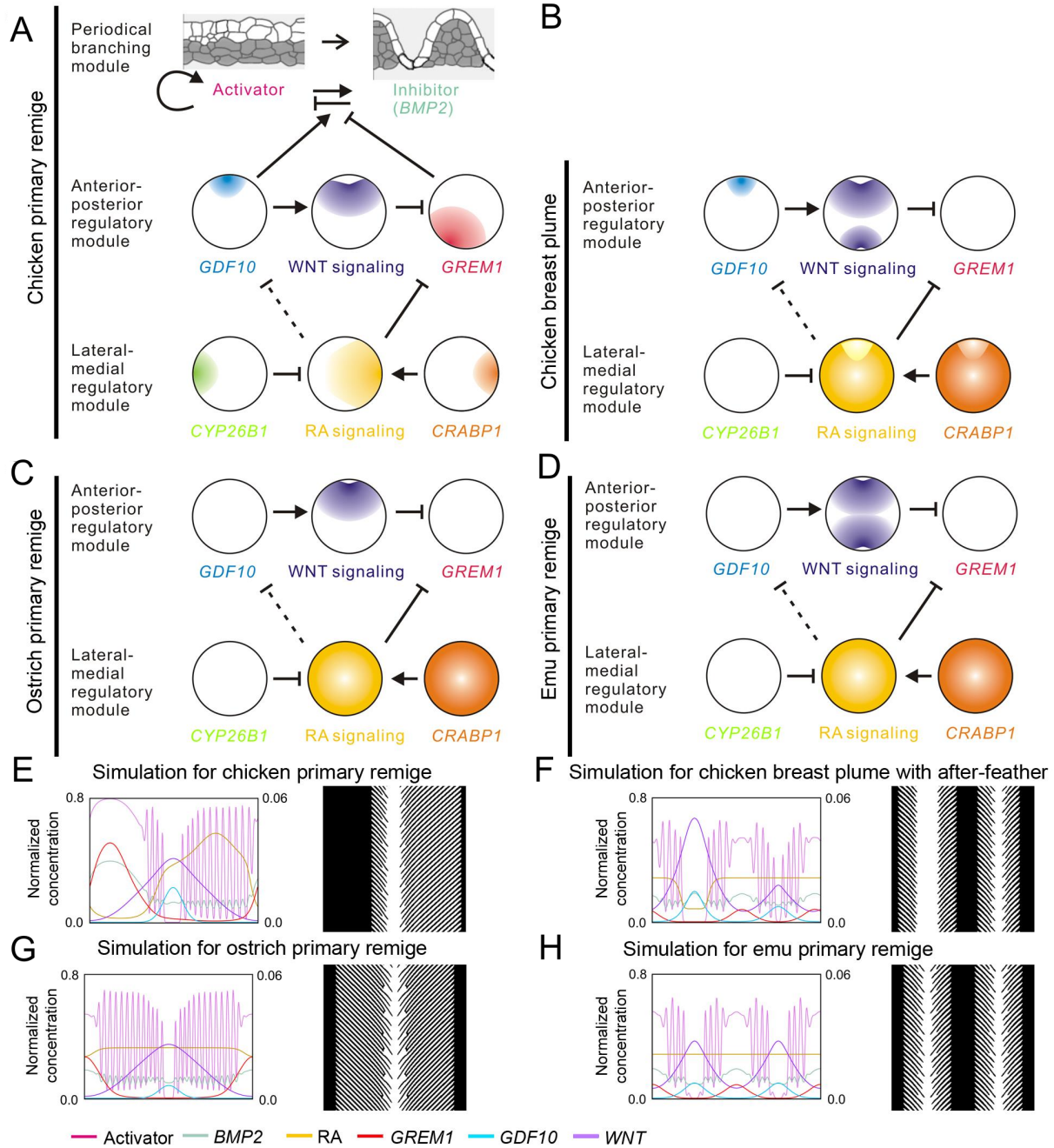
Figure 2.7: Modeling and simulating the change of rachis number and size based on observed gene expression patterns. (A-D) Schematic representation of the multi-module regulatory feather model (MRF) in different feather forms. Periodical branching (PB) model is shown in (A). (E-H) Simulations of diverse feather forms as a result of changes in molecular expression patterns.

Chapter 3

A Single-Cell Tracking Model for Irregular Cell Shapes

3.1 Background

In many biological systems there are individual cell interactions, such as cell-cell signaling [9], cell-extracellular matrix signaling [98], and cell adhesion junctions [99], which govern aspects of tissue morphogenesis. Moreover, cells are often found to take on specific shapes which can also influence the systems behavior [100, 101, 102]. These shapes are a times highly irregular, whereby one axis is much longer than the other or the cells have a specific geometry to them such as culumnar, cuboidal, elliptical, or spherical. There is therefore a need to be able to model a tissue at the scale of the individual cells, which can properly capture their bio chemical and bio mechanical interactions, aswell as model their cell shapes, to properly understand development.

An often used approach is cell-center agent based modeling, in which cells operate under specific biological and physical rules given [103, 104]. While these can capture some cell

interactions and tissue population dynamics, they often do not take into account the cell's shape. More recently cell-center based models have attempted to resolve this by approximating irregular shapes by ellipses [34, 105]. While these can account for changes in the aspect ratio of cells, it does not take into account the cells specific geometry.

Here we present a single-cell tracking model for irregular cell shapes which combines realistic cell morphologies with cell-cell bio-mechanics and tissue population dynamics. Our model includes an ability to describe the cell's shape in terms of its geometric features as well as changes in its aspect ratio. Cell bio mechanical interactions include cells adhesion as well as repelling one another. The population dynamics of the tissue are scholastically modeled at the individual cell level, and therefore can allow for cells to make informed decisions on their fates based on both temporal and spatial cues.

Parameters for all simulations can be found in Appendix C.

3.2 Model Formulation

3.2.1 Cell Movement

Let us consider an arrangement of N cells whose centers of mass are located at $n_k = (x_k, y_k)$ for $1 \leq k \leq N$. We define a tissue network from the cells (T) by taking the Delaunay triangulation of the spatial point arrangement of cell centers of mass. This triangulation forms a graph of nodes, representing the cell centers of mass, and edges, representing cell-to-cell contacts [106]. This gives rise to a tissue network in which only neighboring cells are assumed to be in contact, and can therefore interact with one another.

In order to model cell bio-mechanics we must determine exactly how near or far the cells are from one anther. We do this by calculating the distance between surfaces of interacting cells in our network T. The distance between the surface of cell k and another cell i is represented by δ_{ki}. By the symmetric property, the distance from the surface of cell i to cell is $\delta_{ik} = -\delta_{ki}$. We assume the bio-mechanical forces involved in cell interaction are of two varieties. The first is an outward pressure exerted by the cells on one another if they are too close (defined by $\delta_{ik}^p < 0$). The second is an attractive force, whereby the cells bind to one another when they are in a close enough range. The adhesion between cells is caused in part by adhesive molecules, such as cadherin and integrin [107], present on the cell surface. We model these attractive and repulsive forces using eqs. (3.1) and (3.2) [34, 108, 109]. Where the amount of repulsive force on cell k by cell i ($V_{k,i}$) is proportional to the overlapping length of the cells. The adhesive force ($U_{k,i}$) is linearly proportional to the space between the distance of the cell surfaces, given that $\delta_{ki} > 0$, and that the cells are within a range close enough for adhesive molecules to bind ($\delta_{ki} < \sigma$). V_0 and U_0 are constants of proportionality. By symmetry, the force acting on cell i is equal and opposite the force acting on cell k, therefore computation times can be minimized.

$$
V_{k,i} = \begin{cases} V_0 \delta_{ik} & \text{if, } \delta_{ik} < 0 \\ 0 & \text{Otherwise} \end{cases} \tag{3.1}
$$

$$
U_{k,i} = \begin{cases} U_0 \delta_{ik} & \text{if, } 0 > \delta_{ik} < \sigma \\ 0 & \text{Otherwise} \end{cases} \tag{3.2}
$$

$$
\tag{3.3}
$$

The direction of the force is along the vector $\boldsymbol{v}_{ki}$, which is a vector pointing from the center of mass of cell k to the cell center of mass on cell i. By computing the forces acting on cell k by all the cells in which it is connected to by an edge in T we can get the overall force acting on the k fig. 3.1 A.

$$
\boldsymbol{F}_k = \Sigma_{O(i)} V_{k,i} \boldsymbol{v}_{ki} + \Sigma_{O(i)} U_{k,i} \boldsymbol{v}_{ki} \tag{3.4}
$$

We can the calculate the motion of the cell due to the force exerted on it by:

$$
\mu \frac{dn_k}{dt} = \boldsymbol{F}_k \tag{3.5}
$$

Which we can solve for numerically using a the forward euler method, giving us:

$$
n_k(t + \Delta t) \approx n_k - \frac{\boldsymbol{F}_k}{\mu} \Delta t \tag{3.6}
$$

3.2.2 Irregular Cell Shapes

In some models the Delaunay triangulation is used with a Morse potential [108] to calculate cell movement and the cell size is simply determined by how far two cell nodes are from one another. However, this necessitates the assumtion that cells are perfect circles. Due to the possibility of the cells having highly irregular shapes, i.e. where one axis is much longer than the other, simply using the edges from the triangulated mesh may not always result in desired cell interaction (fig. 3.1 B). Others have developed cell center based models which account for irregular shapes by approximating cells by various ellipses and calculating the distance between the cell surfaces, or the area of overlap between cells, to model more complex shapes [34, 105]. While these methods can account for cells which have elongated shapes, the cells must still be modeled as ellipses which cannot account for cuboidal or columnar cells, as can be found in several tissues (fig. 3.1 C) [100, 110, 111]. Here we develop a new method of modeling cell-cell interaction that allows for bio-mechanical interaction between cells of highly irregular shapes that can differentiate between ellipsoid cell types and cuboidal cell types.

The shape and size of each cell is described by three parameters, a_k, b_k and s_k such that they form a type of "rectellipse" eq. (3.7) [2, 3], where the cell k has width $2a_k$ and a height of $2b_k$. The value of s_k describes the degree of curvature of the cell walls, where a cell with $s = 1$ is perfectly rectangular, and a cell with $s = 0$ is perfectly round, seen in fig. 3.2 A. The formula for a rectellipse is a semi-algebraic curve, therefore in order to prevent multiple branches to form our cells we restrict the values of χ_k and γ_k to eqs. (3.8) and (3.9).

$$\left(s_k \frac{\chi_k}{a_k} \frac{\gamma_k}{b_k} \right)^2 - \left(\frac{\chi_k^2}{a_k^2} + \frac{\gamma_k^2}{b_k^2} \right) + 1 = 0 \tag{3.7}$$

$$|\chi_k| \leq a_k \tag{3.8}$$

$$|\gamma_k| \leq b_k \tag{3.9}$$

In order to remedy the issue of cell center nodes being unable to account for irregular cells interacting along long axis, cells of highly irregular shapes have additional cell points P_k added along the longer cell axis. The new cell nodes for cell k are located at $n_k^p = (x_k^p, y_k^p)$, where $1 \leq p \leq P_k$. The number of additional cell points is determined by eq. (3.10), and the points are located at points equidistant from one another and the boundary of the cell, along the longer cell axis . If both axis of the cell are equal then the cell is represented by a single node, $n_k^1 = n_k$ (fig. 3.2 B).

$$P_k = \text{floor} \left(\frac{max(a_k, b_k)}{min(a_k, b_k)} \right) \tag{3.10}$$

A new tissue network of the cells (T^*) is found with a Delauney Triangulation using the new cell centers, whereby edges connecting two nodes within the same cell are disregarded. We also only allow cells to interact once with another specific cell, therefore if two nodes from a single cell have an edge with another cell, the only the closest pair is considered. The translated equation for the rectellipse drawn around node n_k^p becomes:

$$\left(s_k \frac{\chi_k - \alpha}{a_k} \frac{\gamma_k - \beta}{b_k}\right)^2 - \left(\frac{(\chi_k - \alpha)^2}{a_k^2} + \frac{(\gamma_k - \beta)^2}{b_k^2}\right) + 1 = 0 \tag{3.11}$$

$$\alpha = x_k^p - x_k \tag{3.12}$$

$$\beta = y_k^p - y_k \tag{3.13}$$

The question now arises as to how to find the δ_{ki} for cells of highly irregular shapes. To do this we first determine the direction vector $\boldsymbol{v}_{ki}^p$ through the translated cell node, n_k^p, connected by an edge on T^* to the translated node of another cell, n_i. We then find where along the cell surfaces the direction vector crosses, allowing us to compute r_{ki}^p and r_i, which are the distances from the cell centers n_k^p and n_i to their respective cell surfaces along vector $\boldsymbol{v}_{ki}^p$ (fig. 3.2 C). If the direction vector points to a cardinal direction (i.e. the vector is a unit vector), then the distance from the cell center of mass n_k^p to the cell surface along $\boldsymbol{v}_{ki}^p$ can be found trivially by solving for χ_{ki} or γ_{ki} in eq. (3.14), depending on the vector bearing.

$$\begin{cases} \left(s_k \frac{\chi_{ki}-\alpha}{a_k} \frac{\beta}{b_k}\right)^2 - \left(\frac{(\chi_{ki}-\alpha)^2}{a_k^2} + \frac{\beta^2}{b_k^2}\right) + 1 = 0 & \text{if, } \boldsymbol{v}_{ki}^p = \begin{bmatrix} \pm 1 \\ 0 \end{bmatrix} \\[2em] \left(s_k \frac{\alpha}{a_k} \frac{\gamma_{ki}-\beta}{b_k}\right)^2 - \left(\frac{\alpha^2}{a_k^2} + \frac{(\gamma_{ki}-\beta)^2}{b_k^2}\right) + 1 = 0 & \text{if, } \boldsymbol{v}_{ki}^p = \begin{bmatrix} 0 \\ \pm 1 \end{bmatrix} \end{cases} \tag{3.14}$$

Since solving for either χ_{ki} or γ_{ki} will yield two solutions, we define r_{ki}^p as the minimum of the absolute value between the two solutions. The larger solution would be the distance from the node n_k^p to the cell surface along vector $-\boldsymbol{v}_{ki}^p$.

$$r_{ki}^p = \begin{cases} min(|\chi_{ki}|) & \text{if, } \boldsymbol{v}_{ki}^p = \begin{bmatrix} \pm 1 \\ 0 \end{bmatrix} \\ \\ min(|\gamma_{ki}|) & \text{if, } \boldsymbol{v}_{ki}^p = \begin{bmatrix} 0 \\ \pm 1 \end{bmatrix} \end{cases} \tag{3.15}$$

The distance r_i is found similarly.

If the vector does not equate to a cardinal direction, then to find the distance from n_{ki}^p to the cell surface along vector $\boldsymbol{v}_{ki}^p$ we need to solve our rearranged form of eq. (3.11) for γ_{ki}. We make the solved form of γ_{ki} be a function of ξ (eq. (3.16)). Once again, there are multiple solutions for γ_{ki}. We choose which function of γ_{ki} to use based on the relative position of the two cell nodes, n_{ki}^p and n_i, to one another. We also constrain our model to have $s_k < 1$ to avoid dividing by zero.

$$\gamma_{ki}(\chi) = \begin{cases} \beta + b_k \sqrt{\frac{a_k^2 + (\chi - \alpha)^2}{a_k^2 - s_k^2(\chi - \alpha)^2}} & \text{if, } y_k^p < y_i \\ \\ \beta - b_k \sqrt{\frac{a_k^2 + (\chi - \alpha)^2}{a_k^2 - s_k^2(\chi - \alpha)^2}} & \text{if, } y_k^p > y_i \end{cases} \tag{3.16}$$

We then define a new function $f(\chi)$, which describes a line drawn along vector $\boldsymbol{v}_{ki}^p$. Finally, we define a function $F(\chi)$, which is a linear combination of $\gamma_{ki}(\xi)$ and $f(\xi)$. By solving for the root of $F(\chi)$ we can determine where along the cell boundary the vector $\boldsymbol{v_{ki}}$ crosses.

$$\boldsymbol{v}_{ki}^p = u\hat{i} + w\hat{j} \tag{3.17}$$

$$f(\chi) = \frac{\nu}{u}\chi - \alpha \tag{3.18}$$

$$F(\chi) = \gamma_{ki} - f(\chi) \tag{3.19}$$

To find the root we employ the use of the Interval Newton's Method [112]. This is done in order to find the solution on the correct quadrant of the cell. Interval Newton's Method works as follows, we begin by defining a function $F(x)$, such that its derivative is continuous in the interval $[a, b]$:

$$0 \notin \{F'x, x \in [h_1, h_2]\} \text{ and } F(h_1) \cdot F(h_2) < 0 \tag{3.20}$$

An interval X_n, which is within $[h_1, h_2]$ and contains the zero of function $F(x)$ is improved to a smaller interval X_{n+1} by:

$$X_{n+1} := \left(m(X_n) - \frac{F(m(X_n))}{F'(X_n)} \right) \cap X_n \tag{3.21}$$

Where $m(X_n)$ is a point within the interval X_n. In our model we define $m(X_n)$ as the midpoint in X_n. We choose the initial interval $X_0 = [h_1, h_2]$ based on where the two cell nodes n_{ik}^p and n_i are relative to one another. The iterative root finding method is run until the range between X_n reaches a certain tolerance or a max iteration has been reached. In the case of a max iteration being reached, a bisect method is used to find the root. Figure 3.3 A and B shows the Iterative Newton's Method converging to the solution on circular ($s = 0$) and cuboidal ($s = 0.99$) cell shapes. The tolerance used as a stopping criteria was $1e - 4$,

which the method was able to achieve in 6 or fewer iterations. The method is also able to converge to the solution in more complex elongated shapes (fig. 3.4 A) as well as when the cell node is displaced from the cell center of mass (fig. 3.4 B).

The solution to the root of $F(\chi)$ is χ_{ki}^p, which we then input in eq. (3.16) to get γ_{ki}^p. The distance r_{ki}^p is then defined as:

$$r_{ki}^p = \sqrt{(\chi_{ki}^p)^2 + (\gamma_{ki}^p)^2} \tag{3.22}$$

Distance r_i is found in a similar fashion.

Using r_k^p and r_i, as well as the distance between nodes n_k^p and n_i, we can determine the distance δ_{ik}^p between the cell surfaces of cell k and i eq. (3.23).

$$\delta_{ik}^p = \sqrt{(x_k^p - x_i)^2 + (y_k^p - y_i)^2} - |r_k^p| - |r_i| \tag{3.23}$$

The force, however, does not act on the node n_k^p. Instead assume the force acts on the original cell center of mass n_k, giving us the force acting on cell k at one instant as (fig. 3.2 C):

$$\boldsymbol{F}_k = \Sigma_{O(p)}\Sigma_{O(i)}V_{k,i}^p\boldsymbol{v}_{ki}^{\boldsymbol{p}} + \Sigma_{O(p)}\Sigma_{O(i)}U_{k,i}^p\boldsymbol{v}_{ki}^p \tag{3.24}$$

Figure 3.5 shows a the time evolution of a cluster made up of three distinct types of cells of various shapes and sizes and how they are able to arrange themselves. We see that as time evolved the cells that are overlapping move away from one another. The model is able

to arrange the cells despite their being cuboidal, round, or rectangular. The simulation is terminated when the maximum force $\boldsymbol{F}$ of each cell is less than a given tolerance.

3.2.3 Tissue Growth

Tissues growth and homeostasis is often the result of cell proliferation balanced with cell apoptosis. Often cells, such as stem cells and transit amplifying cells are able to self-replicate during proliferation, or differentiate. To implement the proliferation, self-replication, and apoptosis undergone by cells in a tissue we first describe the cell-lineage by a set of modified cell lineage ODEs [30] to allow for differences in asymmetric and symmetric differentiation [113, 114, 115]. Suppose that the tissue is composed of $M+1$ cell types, then each cell type, c_j, where $j = 0, ..., M$, has an associated proliferation rate, ν_j and a cell apoptosis rate, d_j. Each cell type j, that undergoes cell division also has a probability of symmetrically differentiating, p_j^s, asymmetrically differentiating, p_j^a, or self-replicating, p_j^r, where $p_j^s + p_j^a + p_j^r = 1$. The governing deterministic ODE's for this system are as follows:

$$
\begin{aligned}
c_0 &= c_0\nu_0(p_0^r - p_0^s) - c_0 d_0 \\
c_1 &= c_0\nu_0(2p_0^s + p_0^a) + c_1\nu_1(p_1^r - p_1^s) - c_1 d_1 \\
&\vdots \\
c_{M-1} &= c_{M-2}\nu_{M-2}(2p_{M-2}^s + p_{M-2}^a) + c_{M-1}\nu_{M-1}(p_{M-1}^r - p_{M-1}^s) - c_{M-1} d_{M-1} \\
c_M &= c_{M-1}\nu_{M-1}(2p_{M-1}^s + p_{M-1}^a) - c_M d_M
\end{aligned}
\tag{3.25}
$$

Since the number of cell we are modeling is small, we can stochastically simulate the dynamics of the cells using a Stochastic Simulation Algorithm (SSA), [116, 117]. Here, we are modeling events at an individual cell level, and not the population dynamics as a whole, so we must

modify the above ODEs to treat each individual cell as its own differential equation, otherwise the SSA model would give us the event that occurred to a specific cell population type, but not to which specific cell. The event rates, therefore, for a particular cell k, in a population of N cells, can be though of as $\nu_{kj}p_j^s$, $\nu_{kj}p_j^a$, $\nu_{kj}p_j^r$ and d_{kj} if k is of cell type j. Therefore, the number of possible events which can occur when solving the SSA is equal to $4N$. By modeling the SSA at the individual cell level we are able to use the spatial information of the tissue.

The ODEs for a sample deterministic model consisting of three cell types, a stem cell c_0, a transit amplifying cell c_1, and a terminally differentiated cell c_2, are as follows:

$$
\begin{aligned}
c_0' &= c_0\nu_0(p_0^r - p_0^s) - c_0d_0 \\
c_1' &= c_0\nu_0(2p_0^s + p_0^a) + c_1\nu_1(p_1^r - p_1^s) - c_1d_1 \\
c_2' &= c_1\nu_1(2p_1^s + p_1^a) - c_2d_2
\end{aligned}
\tag{3.26}
$$

In the above system c_0 can either self-replicate or differentiate into c_1. Similarly c_1 can self-replicate or differentiate into c_2. In 3.6, we can see the deterministic solution plotted over several iterations of the SSA solution. We see that modeling the system dynamics at the cell level is able to produce the population dynamics. In 3.5, we simulate a tissue which incorporates both the cell lineage dynamics and the cell-biomechanics of the single cell tracking model. When a cell dies it is removed from the system, an offspring cell is placed in a random position near the mother cell. The model assumes that the movement of cells occurs at a much faster rate than the cell lineage dynamics, therefore after each gillespie time-stem, the single cell tracking model is iterated until the tissue reaches an equilibrium.

3.3 Conclusion

In this chapter we have presented a novel single cell tracking model able to simulate the bio-mechanical interactions between cells of highly irregular shapes. The cells are represented by "rectellipses" [2, 3], and thus can take a variety of forms found in biological systems which previous cell-center models are unable to account for. In order to model cells of highly elongated shapes (where one cell axis is much longer than the other) the we add additional nodes to along the longer cell axis. A Delauney Triangulation is then used with these additional nodes, giving a more accurate representation of which cells are in contact with one another. Furthermore, the model employs the use of root-finding methods to calculate the distances between cell nodes and cell surface boundaries, giving us a highly accurate approximation to the distance between the surfaces of interacting cells. These methods together allow us to more accurately simulate the bio-mechanical forces and cell movement than previous models have allowed for irregular cell shapes.

The model also employs a novel approach to the use of a Stochastic Simulation Algorithm for modeling population cell lineage dynamics and tissue growth. Rather than applying the SSA to pools of cell populations in the system, each cell rate and probability of division is treated individually. This allows us to not only calculate which reaction in the population occurs, but also to which specific cell it occurs to. This can be highly useful in modeling tissues where the cell population dynamics are highly spatially dependent such as in stratified epidermis [71, 23, 24] and drosophila wing disk [118]. In these systems morphogens, which are diffusible signaling molecules, form gradients which cue cell growth, differentiation, and cell fate determination. Therefore, a model must be able to model proliferation rates, division probabilities, and cell apoptosis in both a spatial and temporal manner. The addition of diffusible signaling molecules, as well as internal regulatory networks in the cells can improve the single cell tracking model presented.

3.4 Figures
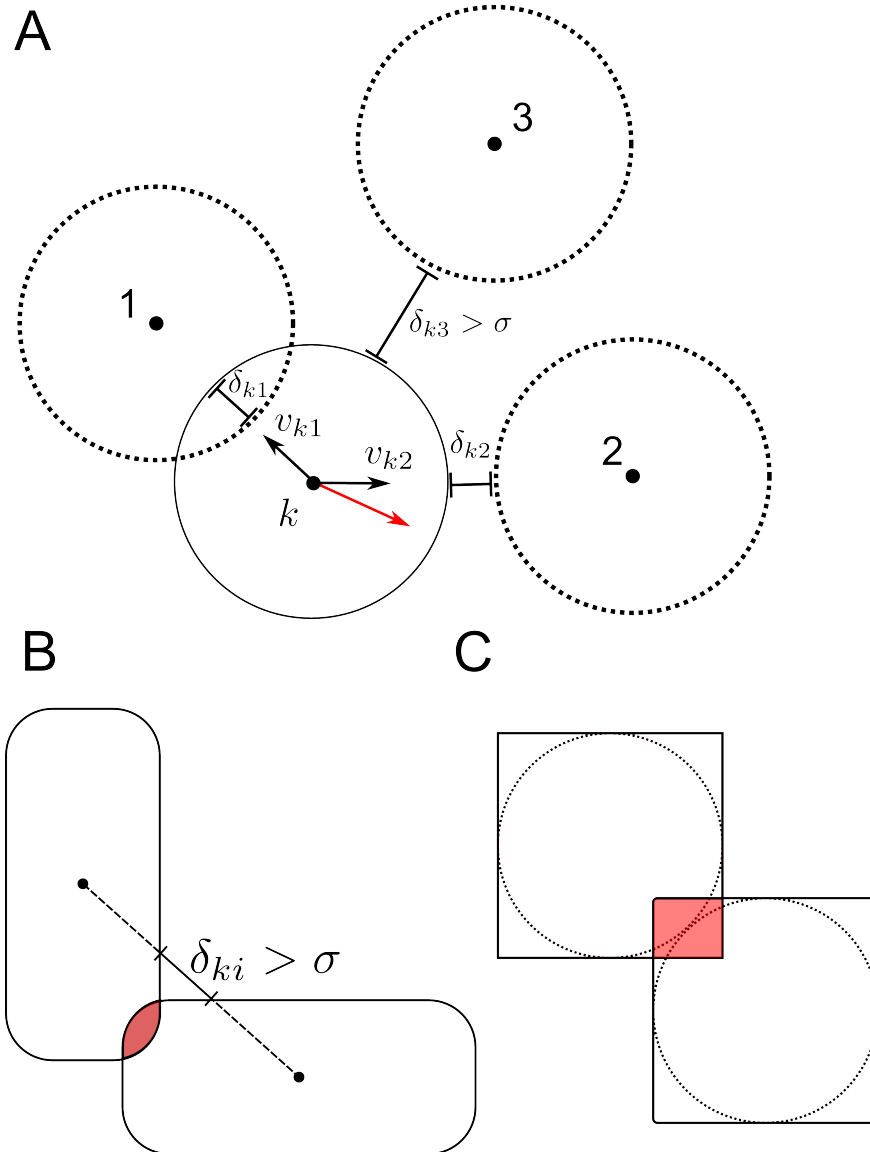
Figure 3.1: (A)Schematic for traditional cell center-based model. The distance between cell surfaces δ_{ki} is used to determine the forces acting on cell k. Cell k and cell 1 are overlapping thus cell k will be pushed away from cell 1 along vector v_{k1}. Cell 2 is near enough to k to attach to it, thus cell k will move toward to cell 2 along vector v_{k2}. Cell 3 is too far to interact with cell k and thus has no influence on cell k's movement. The red arrow shows the direction of cell k's movement due to forces exerted on it by cells 1 and 2. (B,C) Illustrations describing the pitfalls of the traditional cell-center based models when applied to irregular shapes. Cells of elongated shapes may be modeled as not interacting due to their nodes being too far away, despite that the cells are in fact overlapping at their edges. Cells of cuboidal shape are poorly approximated with circles, resulting in an overlap of cells.
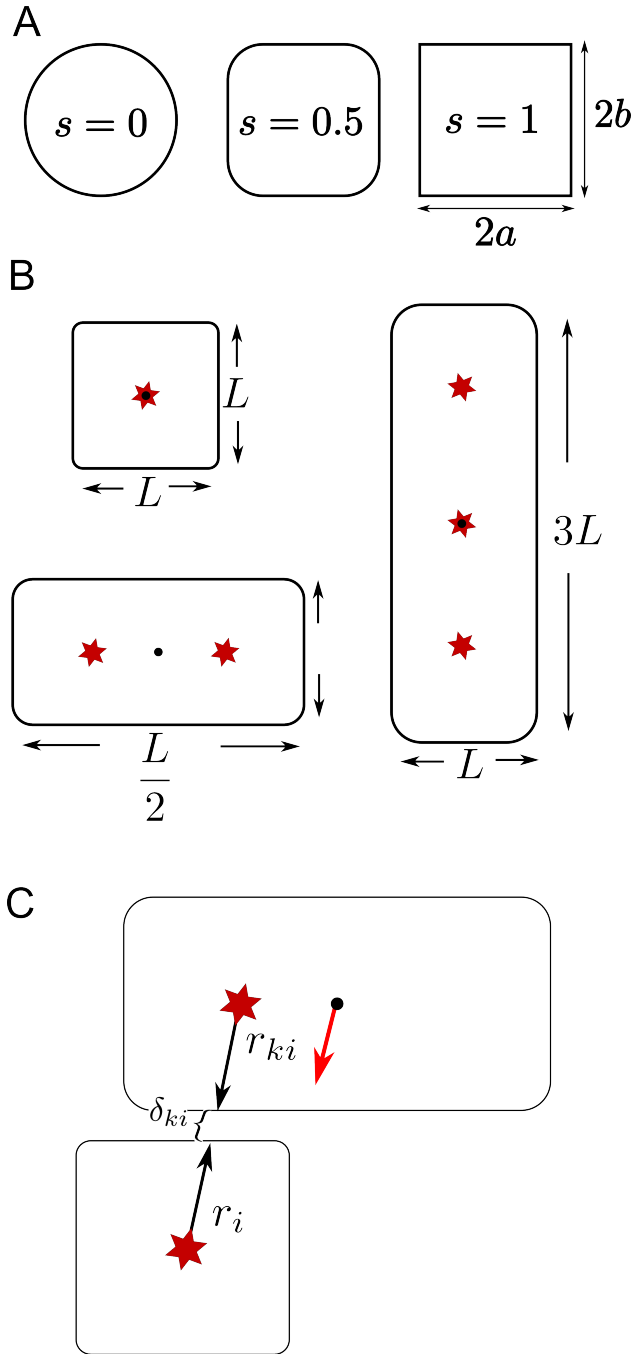
Figure 3.2: (A) Cell shapes are approximated by "rectellipses" [2, 3], where their height is and length are described by variables a and b, and the roundness of their boundary is a function of s in 3.7. (B) Additional cell nodes (red stars) are added to cells with elongated shapes. The number of added nodes corresponds to the ratio of the height and the width of the cell. (C) The distances, r_{ki} and r_i, from interacting nodes (red stars), to the cell surface boundary along a line which connects them, is used to calculate δ_{ki}, the distance between the surfaces of interacting nodes. The force due to the interaction between translated nodes acts on the center of mass of the cell (red arrow).

A

No. of Iterations = 0   No. of Iterations = 1   No. of Iterations = 3   No. of Iterations = 5
Interval Width = 1   Interval Width = 0.5   Interval Width = 0.05207 Interval Width = 1.7605e-05
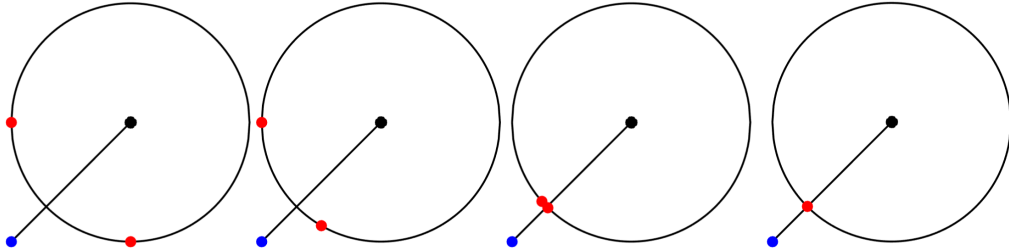
B

No. of Iterations = 0   No. of Iterations = 1   No. of Iterations = 2   No. of Iterations = 6
Interval Width = 1   Interval Width = 0.5   Interval Width = 0.25   Interval Width = 7.8551e-05
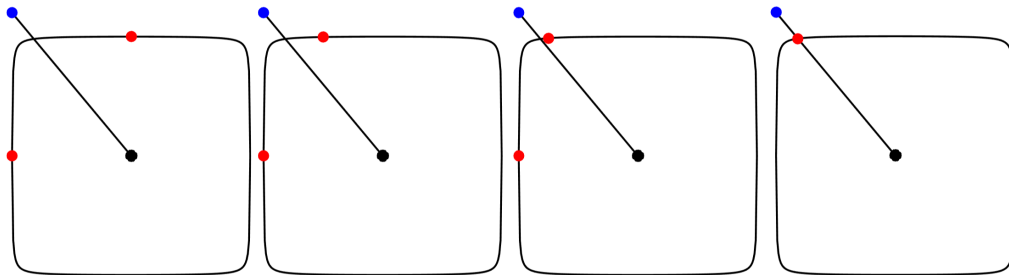
Figure 3.3: Iterations of Interval Newton's Method applied to finding the intersection between a line connecting the black and blue dots, and the surface of the cell. The red dots represent the interval distance being iterated. The stopping criteria used is when the width of the interval is less than $1e-4$(A) A perfectly round cell ($s = 0$, $a = 1$, $b = 1$). (B) A cuboidal cell $s = 0.99$, $a = 1$, $b = 1$

81
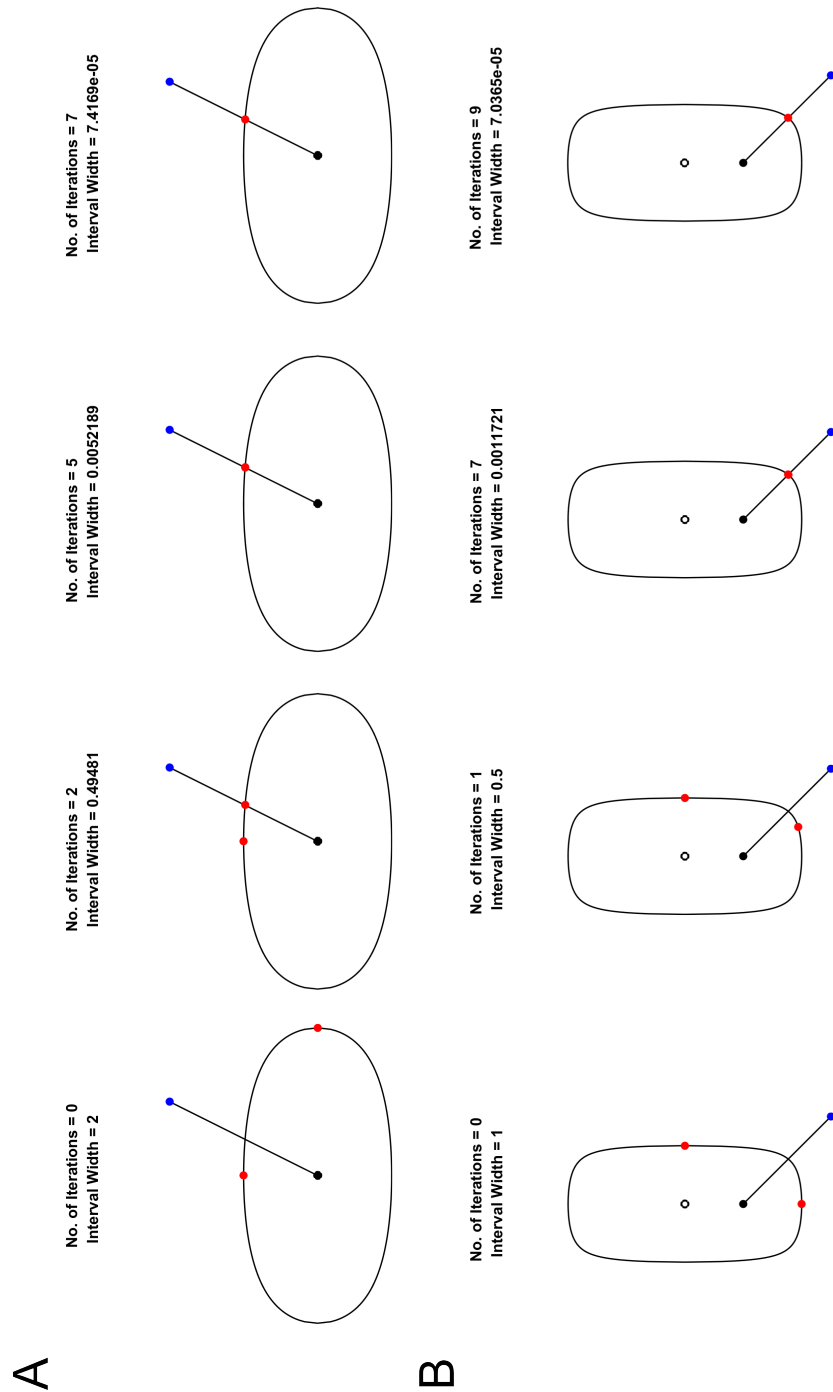
Figure 3.4: Iterations of Interval Newton's Method applied to finding the intersection between a line connecting the black and blue dots, and the surface of the cell. The red dots represent the interval distance being iterated. The stopping criteria used is when the width of the interval is less than $1e-4$. (A) Elongated rounded cells ($s = 0.5$, $a = 2$, $b = 1$). (B) Elongated cells where the node is translated along the longer axis ($s = 0.9$, $a = 1$, $b = 2$)
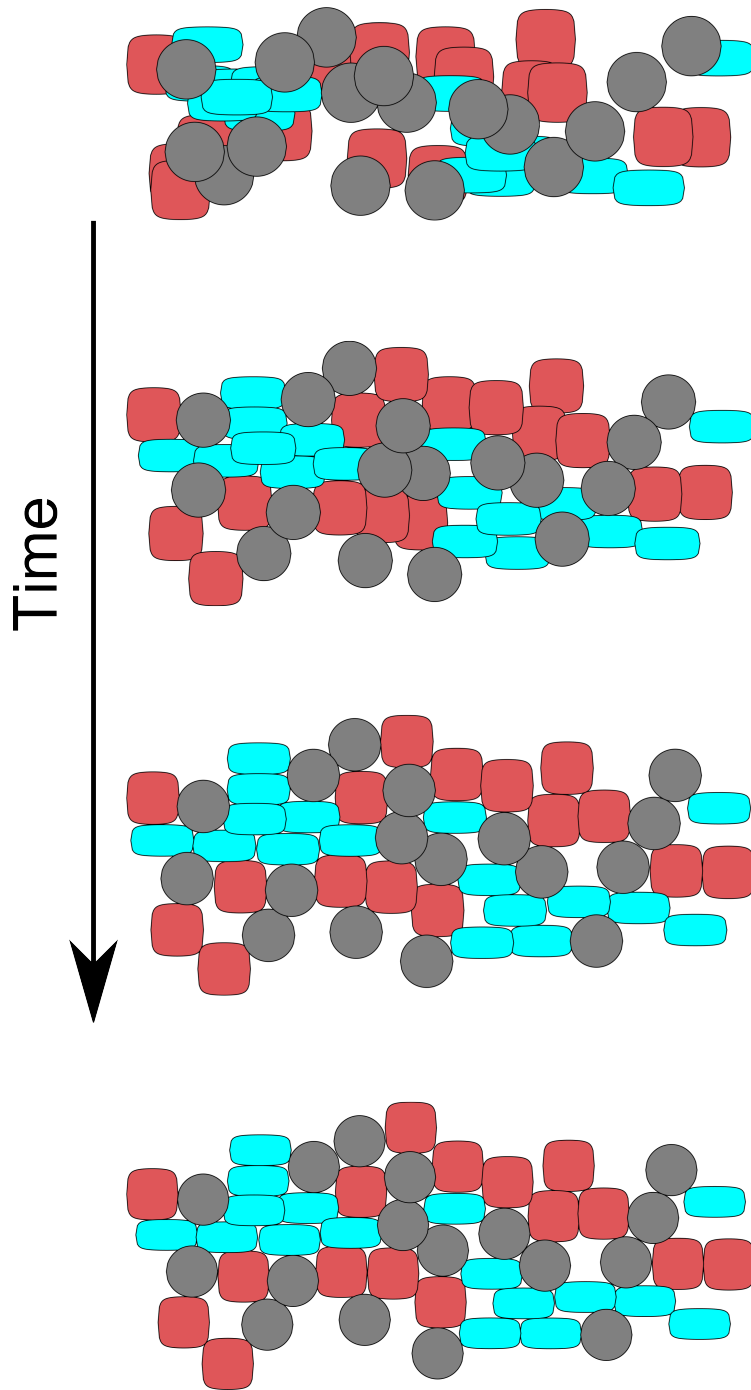
Figure 3.5: Time course of cells rearranging using the single cell tracking model developed. Initial cell positions and type are randomly chosen within a specified domain. The model is able simulate cell bio mechanics regardless of cell shape and size.
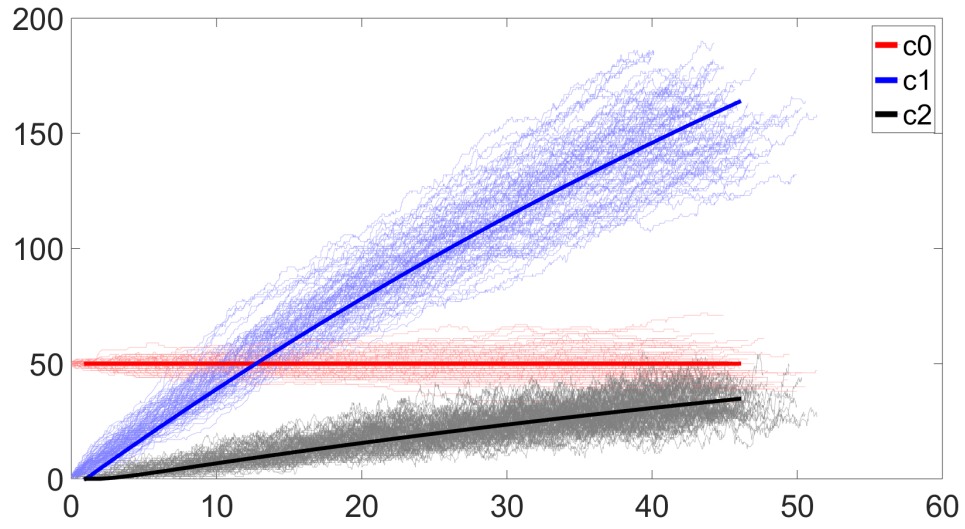
Figure 3.6: Stochastic simulation and deterministic solution to eq. (3.26) with parameters. The stochastic simulations were run 200 times for a specific set of initial conditions.
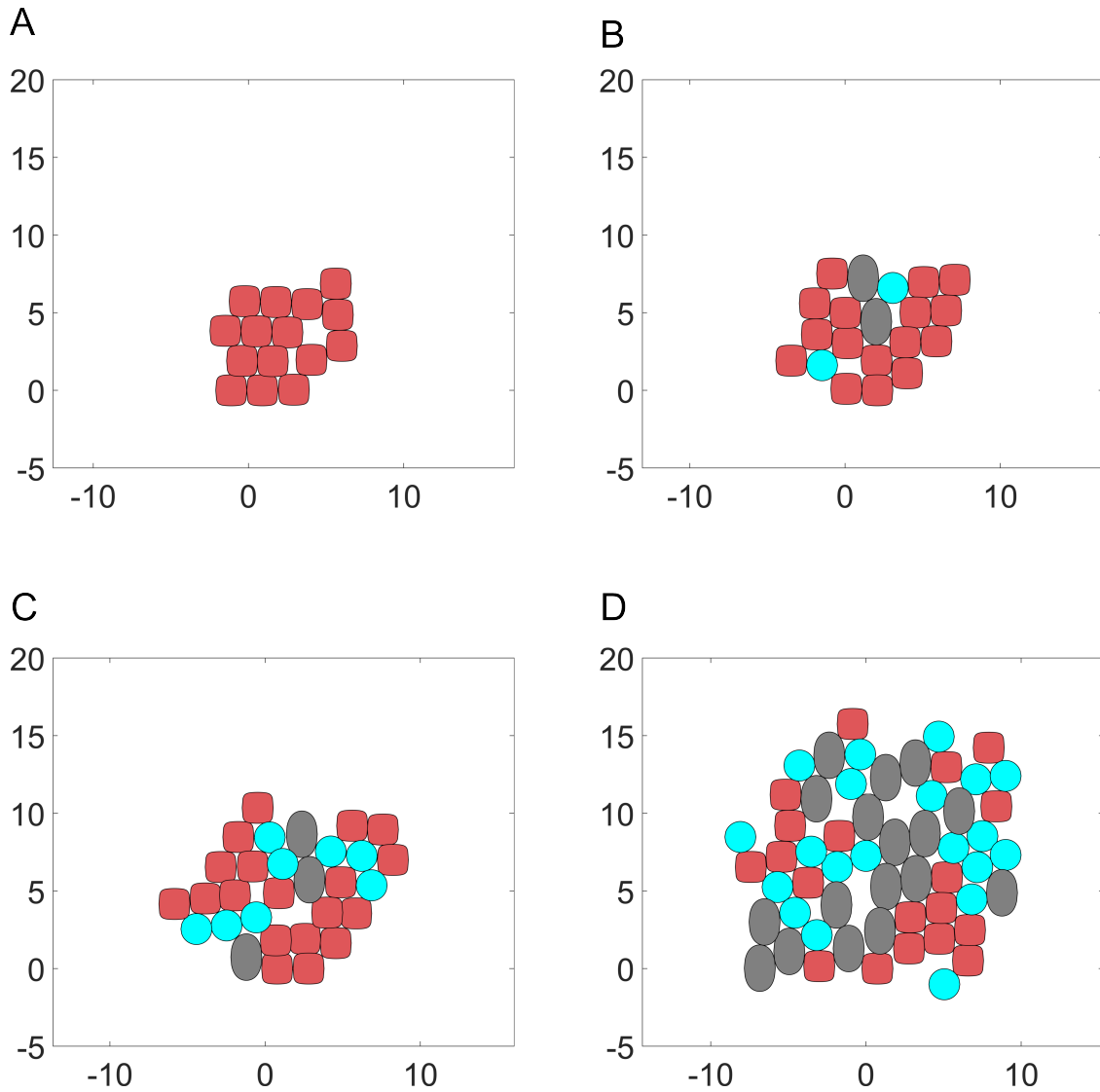
Figure 3.7: Temporal evolution using the Single cell tracking model to simulate cell-cell interaction forces and the Stochasitc Simulation Algorithm to simulate population dynamics of eq. (3.26). (A) An initial condition of 15 c_0 cells(red, ($s = 0.9$, $a = 1$, $b = 1$)) was given. (B,D) Temporal evolution of the system. c_1 cells (cyan, $s = 0$, $a = 1$, $b = 1$) are the offspring of c_0 cells and can differentiate into c_2 cells (grey, $s = 0.5$, $a = 1$, $b = 2$)

Chapter 4

Notch Signaling as a Strategy for Robust Barb Formation in Feathers

4.1 Background

Pattern formation in developing organisms has been a longstanding problem in developmental biology. To create a specific pattern in developing tissues, cells must adopt fates which depends both on their location in space and in time. In 1952 Dr. Alan Turing proposed that cells self organize based on fluctuations in the concentration of diffusible molecules[119]. Since then, it has been shown that the dynamics of activator-inhibitor systems of patterning can be found in many aspects of biology [120, 121, 122, 123]. The specification of cells in an activator-inhibitor system can be complex, however, and as such is sensitive to external environmental influences. This can become an issue once a cell must firmly establish a specific fate, since an activator-inhibitor model may continue to change its fate over time.

One such system can be found in aves, where it is hypothesized that feather barbs are formed through the dynamics of an activator-inhibitor mechanism [89, 100]. In the patterning of

ave plumes, it is believed that the activator expression level in a cell causes it to undergo apoptosis [124, 125]. Therefore, incorrect determination of cell fate can result in a misshapen, and weak feather.

Often times a cell-cell contact based signaling method can be used to help a cell adopt and maintain cell fate. One system often employed for this is a notch based signaling system [126, 127, 128]. A notch regulatory system has been seen in early plume development of aves. It is thought to be responsible for specifying the location of where new feather buds form, as well as being involved in directing their growth [129, 130]. Notch expression has also been noted in early plume develpment, forming along barb-ridges, while serrated, a known transmembrane signaling protein, is expressed at a similar time along the marginal plates [129]. This dual expression is similar to that of BMP, which is expressed in the barb-ridge [88], and Sonic Hendgehog (SHH), which is expresed in the marginal plate [124], of the growing feather barb. BMP is a strong candidate for being the diffusible inhibitor in the activator-inhibitor system, while SHH shares many similarities with the profile of the activator [89].

Here we use our single cell tracking model to explore a notch-serrated signaling mechanism as a way to help determine cell fates in barb formation. We find that the activator-inhibitor model of barb formation is unable to properly determine cell fates in higher dimensions. Through the integration of the activator-inhibitor model with cell-cell contact mediated signaling the we are able to robustly regain the proper pattern of barbs.

4.2 A Discrete Spatial Model of Activator-Inhibitor Mediated Barb Formation

In this section we will adapt the single cell tracking model developed in the previous chapter to study barb formation in feathers. Parameters for all simulations can be found in Appendix D.

In order to use the single cell tracking model for irrgular shapes, we must incorporate diffusion and gene-regulatory dynamics into the model. Diffusion in the system is modeled using a discrete laplace operator eq. (4.1) [131], where ω_k is the number of edges attached to cell k. The cell network T^* is used to define ω_k.

$$\Delta u_k \approx (Lu)_k = \Sigma_i \frac{1}{\omega_k}(u_k - u_i) \tag{4.1}$$

This reduces the diffusion of a signaling molecule in the system to a source sink model. Coupled with a reaction kinetics within the cell a simple reaction-diffusion equation shown in eq. (4.2) can be discritized using a forward euler scheme to become eq. (4.3).

$$\frac{\partial u}{\partial \tau} = D_u \Delta u + v - deg_u u \tag{4.2}$$

$$\frac{U_k^{n+1} - U_k^n}{\Delta t} = \frac{Du}{\omega_k} \Sigma_i (U_k - U_i) + V_k - deg_u U_k \tag{4.3}$$

It has previously been shown that in feather development the cell shape changes based on environmental factors [100]. It is hypothesized that the cell shape change is one crucial mechanism for determining the feather morphology. Through proximal-distal elongation,

the feather is may be able to grow more quickly, thereby decreasing the barb-helical angle. The feather cell shapes are highly cuboidal, and experiments have shown that their proximal-distal length may be as much as three times as long as their medial-lateral width, giving them a highly complex morphology. Our new cell-center based model can be used to study the development of a feather with complicated cell shapes.

Feather barb formation has previously been modeled as an activator inhibitor system along a ring eqs. (4.4) to (4.6) [89, 100], where a slow diffusing, self-regulating activator (A), activates a fast diffusing inhibitor (B) and a non-diffusible inhibitor (C).

$$\frac{\partial [A]}{\partial t} = D_A \frac{\partial^2 [A]}{\partial x^2} + \frac{\left([A]^2 + b_A\right)}{s \left(1 + s_A [A]^2\right) \left(\frac{s_B [B]}{1 + (s_G/[GREM])^{n_G}} + s_C [C]\right)} - r_A [A] \qquad (4.4)$$

$$\frac{\partial [B]}{\partial t} = D_B \frac{\partial^2 B}{\partial x^2} r_A [A]^2 + b_B [GDF] - r_B [B] \qquad (4.5)$$

$$\frac{\partial [C]}{\partial t} = b_C [A]^2 - r_C [C] \qquad (4.6)$$

The concentration of activator A is represented by $[A]$, inhibitors B and C by $[B]$ and $[C]$, Grem1 by $[GREM]$ and GDF10 by $[GDF]$. Here, D_A and D_B are the diffusion coefficients of A and B, r_A, r_B and r_C are decay rates of A, B and C. Parameter s modulates the maximum autocatalytic reaction of A, s_A, s_B, s_C and s_G are saturation coefficients, b_A and b_B are the basal production of A and B, while b_C modulates the maximum production of C. n_G is a Hill coefficient.

Using a forward euler method for time discretization, eqs. (4.4) to (4.6) are transformed into eqs. (4.7) to (4.9):

$$A_k(t + \Delta t) = A_k(t)+$$

$$\left[D_A \Sigma_i \frac{1}{\omega_k} (A_k - A_i) + \frac{A_k^2 + b_a}{s(1 + s_A A_k^2)\left(\frac{s_B B_k}{1+(s_G/grem_k)^{n_G}} + s_C C_k\right)} - r_A A_k \right] \Delta t \qquad (4.7)$$

$$B_k(t + \Delta t) = B_k(t) + \left[D_B \Sigma_i \frac{1}{\omega_k} (B_k - B_i) + r_A A_k^2 + b_b gdf_k - r_B B_k \right] \Delta t \qquad (4.8)$$

$$C_k(t + \Delta t) = C_k(t) + \left[b_C A_k^2 - r_C C_k \right] \Delta t \qquad (4.9)$$

In order to save computational time, the activator-inhibitor model is not solved on a ring of cells, rather a domain is defined from the Barb Generative Zone (BGZ) of the feather follicle to the rachis. We have a high production of gdf at the rachis, and a high production of grem at the BGZ. Both grem and gdf are diffusible molecules, modeled in a similar fashion to the activator inhibitor system. We define the length of our domain as 24 cells wide. We first begin by showing that the activator-inhibitor model presented in this computational frame work is able to produce traveling waves of activator from the BGZ to the rachis, consistent with previous models fig. 4.1. In this instance there is no cell movement or cell proliferation, rather snapshots in time are taken and plotted in reverse chronological order, simulating the growth of a feather. Notice that although the feather formed does not have sharp boundaries between cells with high (black) and cells with low (white) concentrations of activator, the barbs formed are easily distinguishable.

In order to simulate a more realistic model of feather growth the original cell layer is allowed to proliferate upward in time. Biomechanical cellular forces can now move cells, and organize them accordingly. Cell proliferation in here is modeled as a new offspring cell being formed directly above the mother cell. Offspring cells no longer have the capability of proliferating, however they still undergo fate determination through the activator-inhibitor model. Cells

undergo final fate determination once they propagate upward a specified distance from the initial row of proliferating cells. At this point they are removed from the system and become a part of the formed feather.

In fig. 4.2 we can see this process, whereby cells are removed from the system and are considered terminally differentiated once they pass 4 cell heights away from the initial row of proliferating cells. We can see that, even though the parameters for the activator-inhibitor model are unchanged, the feather barbs are no longer properly formed. This is due to the fact that the activator-diffusion coupling is now occuring in two dimension, rather than in a single dimension as has been previously studied. This addition of a second dimension creates a much more difficult environment for the activator waves to propagate properly, and activator signaling is lost. In order tp further study the formation of feathers we must first make the cell specification signal clearer in a system with two spatial dimensions.

4.3 Notch-Serrate Signaling in Cell Specification

The notch contact signaling systems most often works in a sender/receiver system. In these systems, when two cells come into contact surface molecules on the sender cell, such as Jagged, Serrated, or Delta [127], bind to a transmembrane protein Notch expressed on the receiver cell. Receiver cells come in one of two flavors[132]. 1)The signal in the receiver cell upregulates the production of notch, while simultaneously inhibiting the production of the second trans-membrane protein (i.e. Serrated) or 2) The signal in the receiver cell upregulates the production of both notch and the second trans-membrane protein. In the feather system it is unclear which flavor of notch signaling is occuring.

Notch signaling requires cell-cell contact, and therefore cell-center based models are optimal for studying these types of systems. Here we study both flavors of notch signaling using the our new cell-center based model. We assume that serrated production is upregulated by the activator, and that it also auto-regulates. We also assume that internal notch and serrate concentrations mutually inhibit one another. Cell-Cell contact notch signaling upregulates internal notch concentrations and can either inhibit serrate production, which we will refer to as model A fig. 4.3A) or can activate serrate production, which will be referred to as model B (fig. 4.3B). Notch is described by eq. (4.10) for both models. The dynamics of Serrated is described by eq. (4.11) for model A and eq. (4.12) for model B. Here, I represents the cell-cell signaling.

$$\frac{\partial N}{\partial t} = s_N \frac{I + b_N}{1 + I + (\gamma_N N)^{n_N}} - deg_N N \tag{4.10}$$

$$\frac{\partial S}{\partial t} = s_S \frac{b_S S^{n_S} + A^2}{1 + S^{n_S} + I + (\gamma_S N)^{n_S}} - deg_S S \tag{4.11}$$

$$\frac{\partial S}{\partial t} = s_S \frac{b_S S^{n_S} + A^2 + I}{1 + S^{n_S} + (\gamma_S N)^{n_S}} - deg_S S \tag{4.12}$$

We discratize eqs. (4.10) to (4.12) in a similar fashion as above. The levels of trans-membrane notch and serrate are considered to be directly proportional to the concentration of internal notch and serrated concentrations, therefore notch serrate signaling (I) can be modeled by eq. (4.13).

$$I_k = N_k \Sigma_O(i) S_i \tag{4.13}$$

We begin by studying the notch-serrated dynamics of model A when exposed to a steady state, undulating gradient of activator as seen in fig. 4.4 A. We see in that as time evolves serrate expression is high where activator expression in high, while notch expression is high where activator expression is low (fig. 4.4 B). After a certain time activator expression is turned off (fig. 4.4 C). At this time we see that notch and serrate expression is highest when they are touching a cell which is expressing the other signaling molecule. Notch has formed wide bands, while serrate has very narrow bands of single cell width. Although notch bands are wide, the cells in the middle of the bands express a much lower level of notch than cells at the edges of the bands. At a later time, even though activator expression has been turned off, notch and serrate expression is still high fig. 4.4 D. The bands remain similar in size and shape as when activator expression was initially turned off. Cells, however, do not express levels of notch or serrate at the high levels seen when activator expression was on.

When the same activator pattern was tested with model B, similar initial results were seen (fig. 4.5 A,B). Serrate and notch formed sharp bands of expression depending on the level of activator concentration. The bands formed by serrate, however are noticibly wider than the bands formed in model A. The expression of serrate in cells located at the center of the bands is higher than the expression of serrate at cells neighboring cells expressing high levels of notch. Notch expressing cells display similar dynamics as to those seen in model A, where

the cells at the edges of the bands in contact with serrate expressing cells have the highest expression of notch. After a certain time activator expression is turned off fig. 4.5 C. We see that as time evolves the expression of notch in cells at the band edges express higher levels of notch than when activator was present. The notch expressing cells in the middle of their bands continue to express lower levels. Serrate expressing cells appear to express high and uniform levels of serrate regardless of where in the band the cell is located.

From these results we gather that both models of notch-serrate signaling are able to form sharp interfaces when expressed to steady state gradients of activator. Model A formed thinner serrate expressing cell bands, while model B formed wider, even levels of serrate expressing cell bands.

Next we looked to see the influence of the notch-serrate signaling models on barb-rachis formation. We integrated both the notch-serrate models with the activator-inhibitor model of barb-rachis formation (eqs. (4.4) to (4.6)), by having cell fates determined by the levels of serrate, rather than the levels of activator, when cells differentiated. We assumed that the proliferating cells at the bottom of the feather do not express notch or serrate. The offspring cells are able to express both notch and serrate and move upward as new offspring cells are formed. When cells grow past a certain height they are assumed to have become fully differentiated. Cells expressing high levels of serrate undergo apoptosis, while cells that do not express high levels of serrate form the barbs and the rachis. We can see in 4.6 A, that model A forms a feather with alternating bands of high and low serrate. A basic pattern of barb-rachis formation is visible, however, the alternating serrate bands distort the feather morphology. The alternating expression of notch and serrate are characteristic of notch signaling inhibiting the second trans-membrane protein [133, 134]. As one cell expresses a high level of serrate, the cell which proliferates below it and comes into contact with it will have serrate expression inhibited due to notch signaling. This cell therefore does not express serrate, so it cannot inhibit serrate expression in the cell bellow it. This pattern continues

as cells proliferate upward, being broken intermittently by high levels of activator, forming a visible but distorted barb and rachis. Model B, on the other hand, is able to form very clear and sharp barbs and rachis 4.6 B. In this case the activator is able to clearly define which cells express serrate. The notch signaling then aids in the formation of sharp boundaries.

With the notch-serrate model B, we are able use the activator-inhibitor model to study the dynamics of feather development in two dimensions with cell proliferation. We re-visit the hypothesis that cell expansion in the proximal-distal direction can be used as a mechanism to control feather vane shape. Be elongating proximal distal axis of the offspring cells by a factor of two we ran the cell-center based model with the activator-inhibitor dynamics. We see that the barb-rachis angle formed with shorter cells is wider than the barb-rachis angle formed with longer cells fig. 4.7.

4.4 Conclusion

In this chapter we use the Single Cell Tracking model formulated in chapter 3 to explore the two dimensional spatial effects of cell proliferation and shape on barb rachis formation. The use of the single cell tracking model was employed due to the irregular cell shapes feather tissue has been found to have [100]. It was hypothesized that the cell shape elongation found in ave feathers contributed to the formation of barbs with a small helical. Previous models used a continuum approach to simulating barb formation in which growth was defined as a passage of time and did not specifically take cell proliferation or shape into account [89, 100].

We found that when the activator-inhibitor system used in previous barb formation models was applied to a two dimensional spatial system it was unable to produce proper feather morphology. We hypothesized that notch-serrate signaling, which has been shown to form alternating sharp boundaries in the feather follicle [129], can be used in conjunction with the activator-inhibitor system to specify sharp barb boundaries. We showed that a notch signaling system which up-regulates both notch and serrate production, while notch and serrate mutually inhibit one another, can robustly pattern feathers.

Activator-inhibitoe systems has been likened to a language that can be very expressive in placing patterning [172]. As the complexity of the environment grows, the ability for an activator-inhibitor system to properly pattern a system become increasingly difficult. We observe that a system that utilizes the fickle activator-inhibitor system must also utilize a method which is robust to complicated environment to aid the system in proper development and formation. The notch-serrate signaling system proposed in this chapter is one way of achieving that.

4.5 Figures
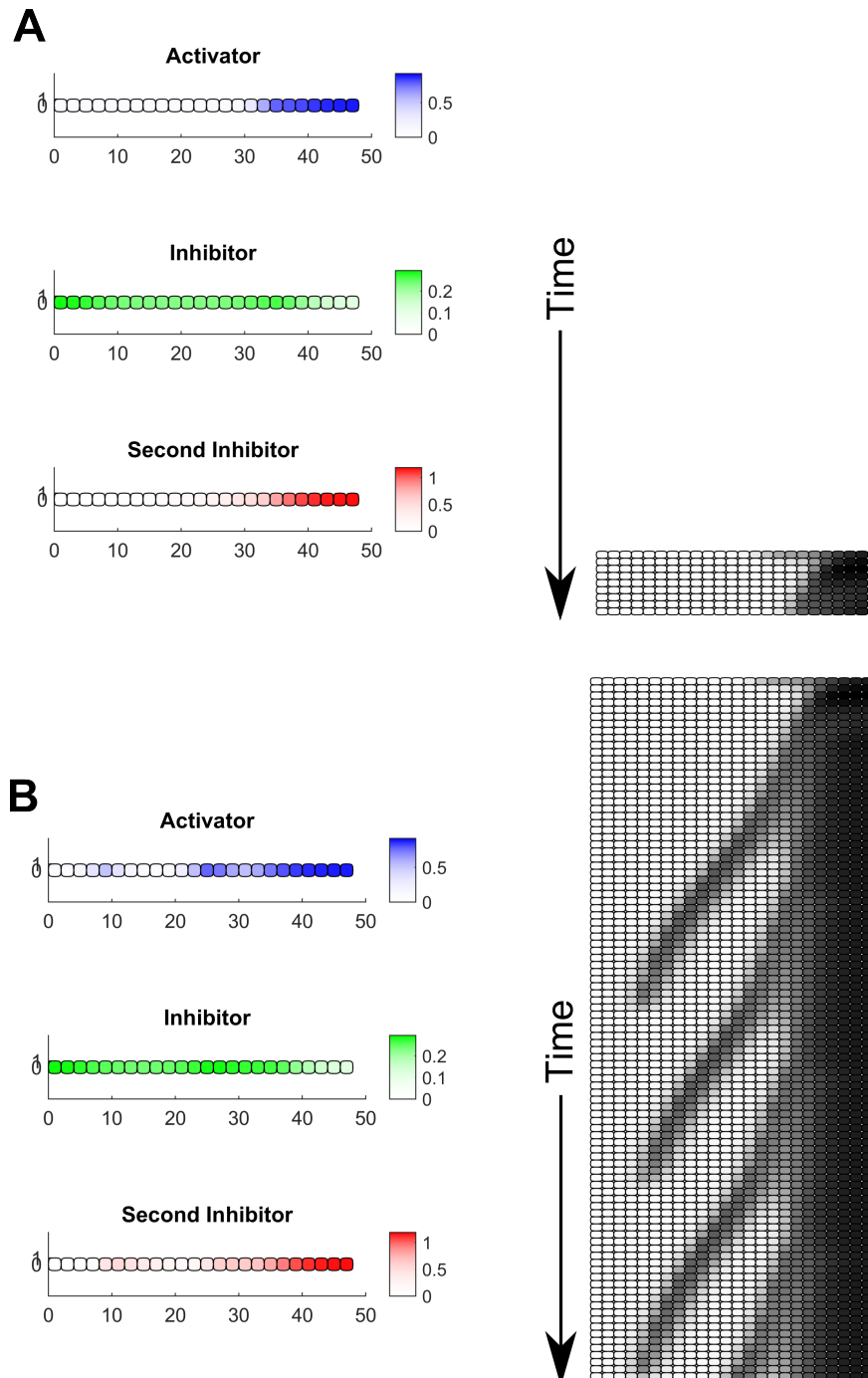
Figure 4.1: Dynamics of activator inhibitor system in single cell-tracking model. Waves of activator initiate from the BGZ (right of x-axis) and propagate to the rachis (left of x-axis) forming feather barbs. There is no cell proliferation, rather the feather is formed from snapshots in time of activator levels in cells. (A) is early time, (B) is later in time
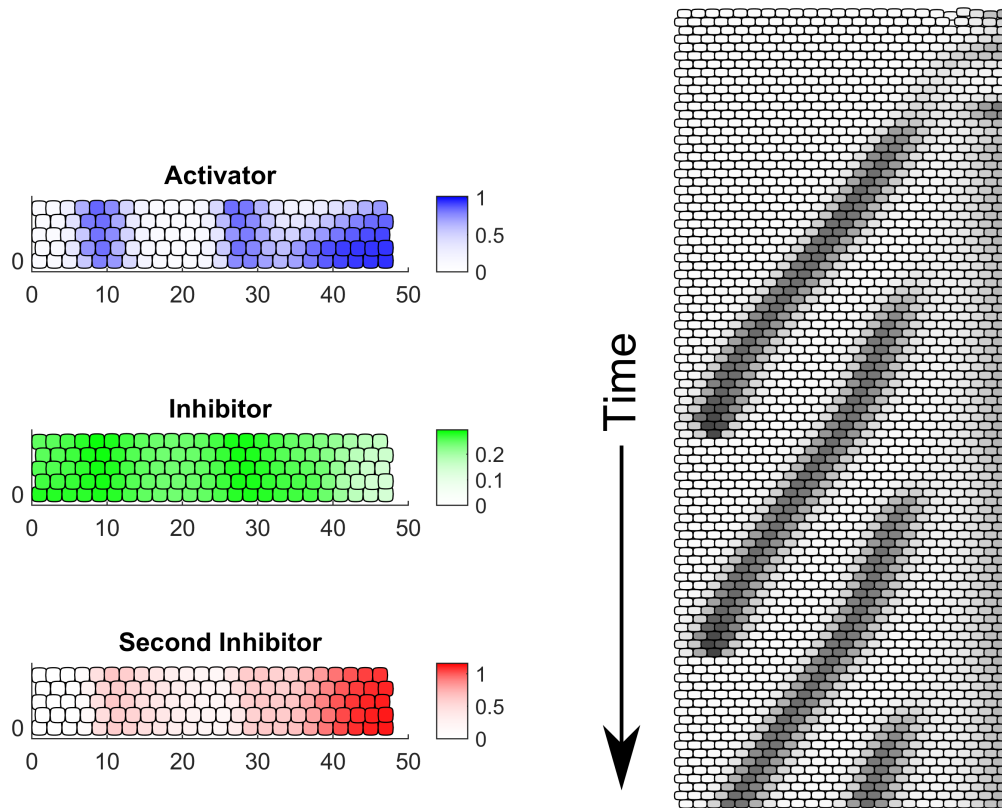
Figure 4.2: Activator-inhibitor system fails to produce proper barbs when cell proliferation is added to the model.
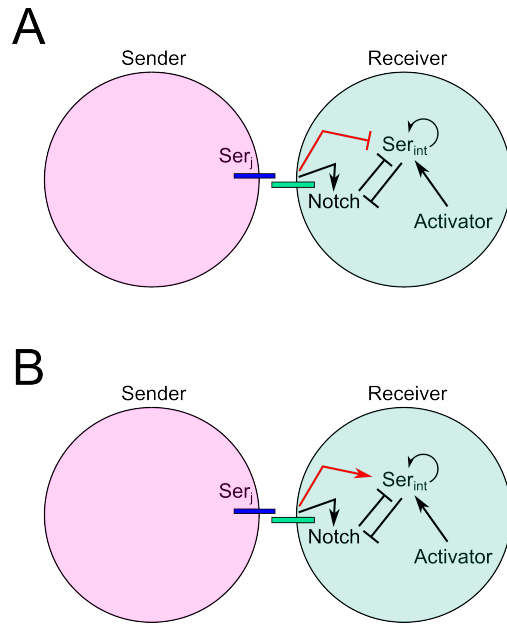
Figure 4.3: Two possible notch-serrate signaling mechanisms in the cell. (A) Notch-serrate signaling inhibits serrate production. (B) Notch-Serrate signaling activates serrate production
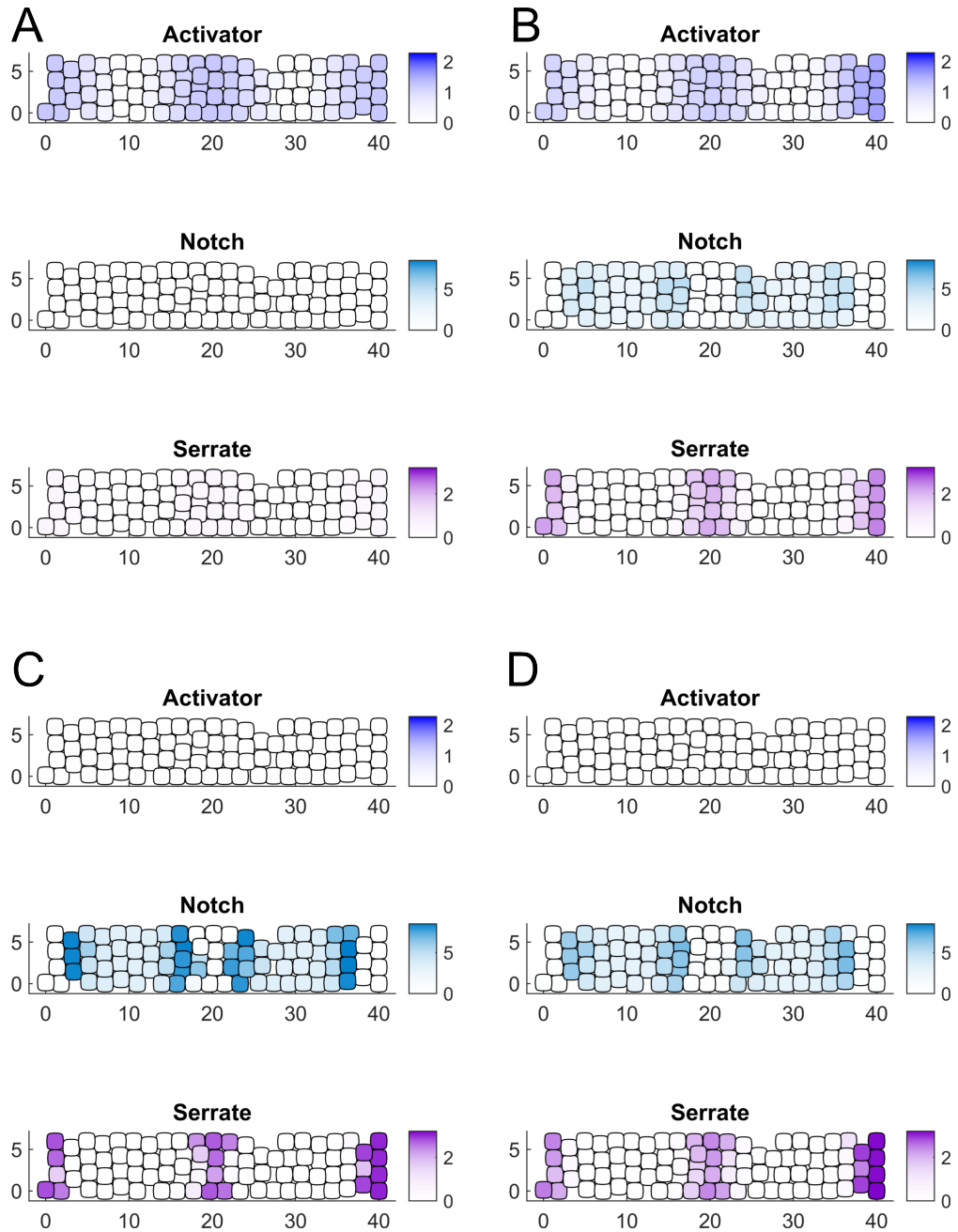
Figure 4.4: Dynamics of notch and serrate signaling inhibits serrate production. (A) initial conditions where activator expression is stratified. (B) Notch and serrate form bands of alternating expression. (C) Activator expression is turned off. (D) Notch serrate band expression remains even with no activator present.
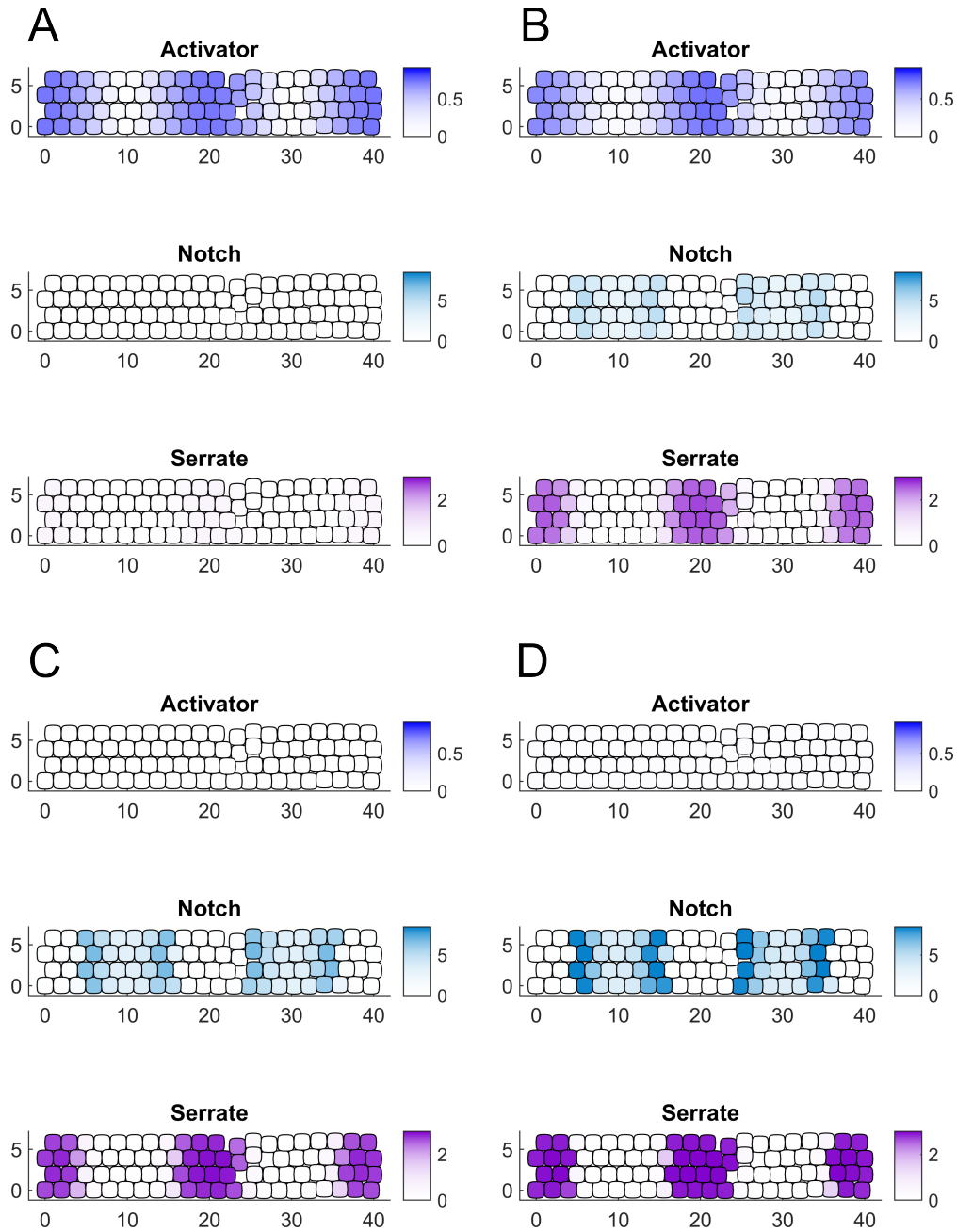
Figure 4.5: Dynamics of notch and serrate signaling activates serrate production. (A) initial conditions where activator expression is stratified. (B) Notch and serrate form bands of alternating expression. (C) Activator expression is turned off. (D) Notch serrate band expression remains even with no activator present.
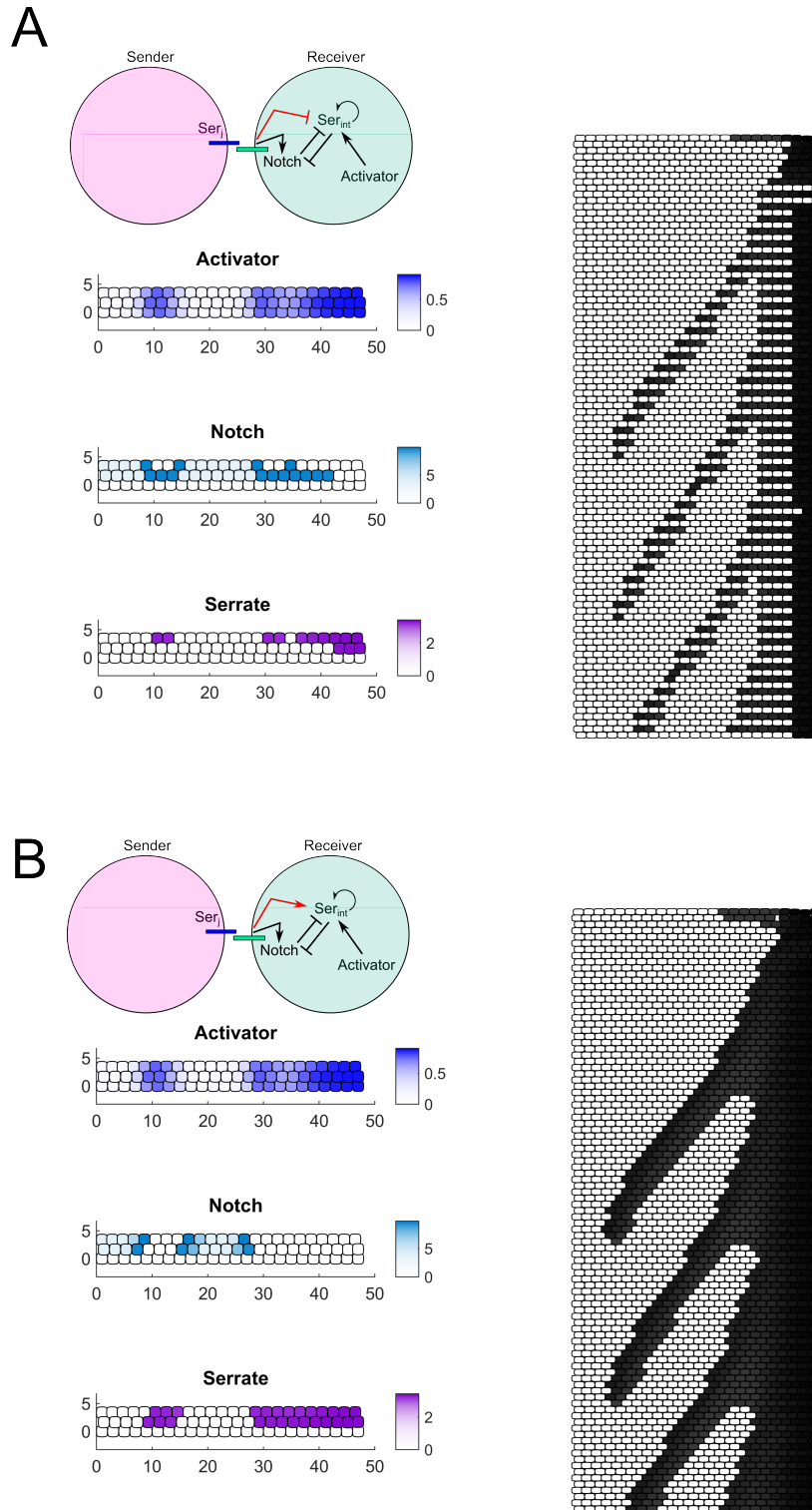
Figure 4.6: (A) Notch-serrate signaling inhibits serrate production does not produce sharp barbs. (B) Notch-serrate signaling upregulates serrate production produces sharp barbs.
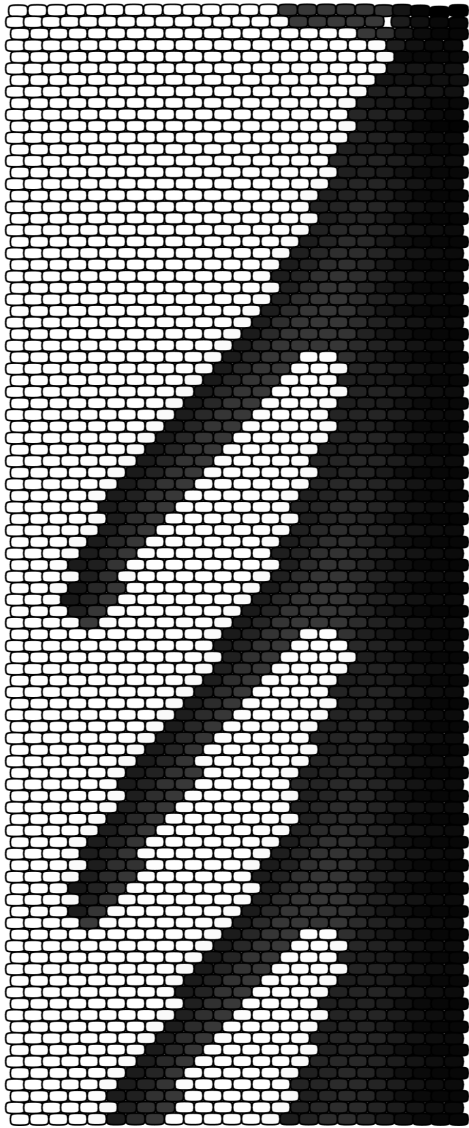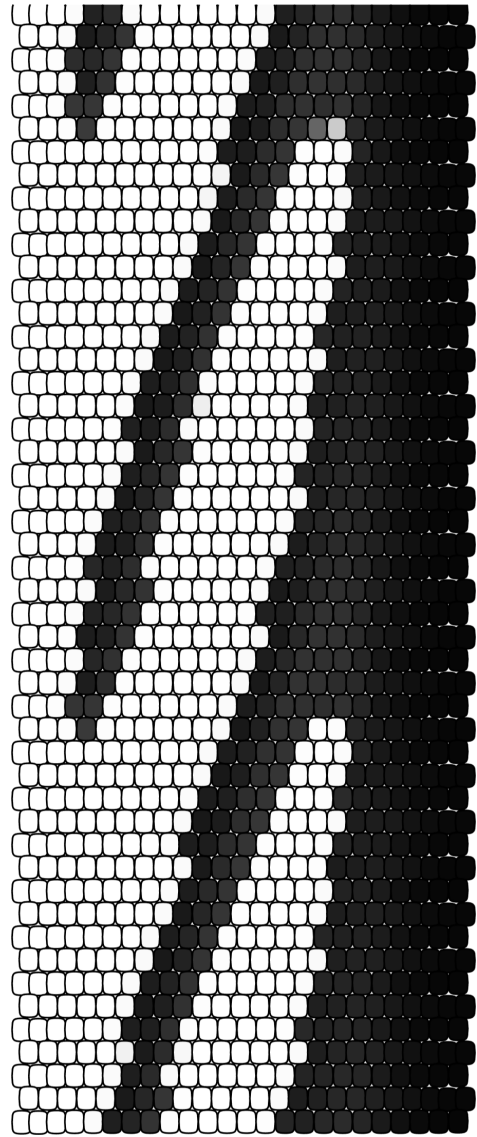
Figure 4.7: Cell elongation in proximal dorsal direction decreases barb-rachis angle. (A) Norma cell astect ratio (B) Elongated cell aspect ratio.

Chapter 5

A Discrete Modeling Framework for Zebrafish Jaw Formation

5.1   Introduction and Biological Background

Pattern formation in developing organisms has been a longstanding problem in developmental biology. To create a specific pattern in developing tissues, cells must adopt fates according to their location. This is can be orchestrated by gradients of secreted signaling molecules, termed morphogens. These morphogens are able to diffuse from a localized source and convey positional information by specifying different cells fates at different morphogen levels [123, 135].

One such system is in zebrafish pharyngeal arch development, where morphogen gradients of Edn and BMP arise and pattern a ventral, intermediate, and dorsal domain in the arch. The ventral domain is specified by expression of Hand, the intermediate domain is specified by Dlx, and the Dorsal domain is specified by Jag, which is part of a Notch-Jag signaling pathway [136, 137, 138]. The gene regulatory network is shown in 5.1. While morphogen

gradients give rise to spatial cues, the boundary specification in arch development in zebrafish also has a temporal aspect in terms of boundary formation order. The intermediate and ventral domains form a sharp boundary early in development, while the dorsal domain appears later and forms a sharp boundary with the intermediate domain. To add complexity to the system, this all occurs while cells are proliferating, and the tissue is growing.

Here, we develop a discrete two-dimensional cell network tissue model to study the role of Notch-Jag signaling in growing zebrafish pharangeal arches. The discrete tissue model is specifically developed to account for the following: (i) cell bio-mechanics, including cell-to-cell adhesion; (ii) cell size; (iii) growth and cell division; (iv) gene regulatory network within cells; and (v) cell contact signaling.

5.2 Model Formulation

5.2.1 Tissue architecture, Cell movement, and Growth

We begin formulating the model in a similar manner to the single cell tracking model in Chapter 3. However, there is no need for modeling cells of irregular shapes, thus we will assume the cells have a spherical shape. Let us consider an arrangement of M cells whose centers of mass are located at n_k for $1 \leq k \leq M$. We define a tissue network from the cells by taking the Delaunay triangulation of the spatial point arrangement of cell centers of mass to form a graph of nodes, representing the cell centers of mass, and edges, representing cell-to-cell contacts[106]. Edges are removed from this graph if their length exceeds a threshold value J^*, giving rise to a tissue network in which only neighboring cells are assumed to be in contact.

To introduce cell bio mechanics into our tissue network, we allow cells to repulse one another when too close, so that each cell essentially consists of a certain amount of volume, and also attract one another when in a certain range, as would be a result of binding of adhesive molecules, such as cadherin and integrin [107] , using the Morse potential [108],

$$V(r) = U_0 e^{-r/\xi} - V_0 e^{-r/\eta} \tag{5.1}$$

In this form, r is the distance from the center of mass of one cell to that of its neighbor and the parameters ξ and η describes the scales in which cell-to-cell attraction and repulsion occur. As a result, the movement of cell k's center of mass is governed by:

$$\mu \frac{d\boldsymbol{y}_k}{dt} = -\Sigma_{O(i)} V(|\boldsymbol{y}_k - \boldsymbol{y}_i|) \tag{5.2}$$

106

where the set i denotes the indices of neighbors of the kth cell. Figure 5.2 shows the cell centers of mass of a tissue reaching an equilibrium.

In order to model the growth and differentiation of the tissue and cells, we define a growth function g_k of the cell. As the cell grows, we assume that once its radius is $\sqrt[3]{2}$ times larger than its initial radius it divides. This is assuming the cell is a sphere, and therefor its volume has doubled before it divides [5]. As a result, we begin with the following equations to describe the behavior of the growth function:

$$g_k(t = 0) = 1 + (\sqrt[3]{2} - 1)\sigma_1 \tag{5.3}$$

$$\frac{dg_k}{dt} = \frac{\sqrt[3]{2} - 1}{\zeta} \tag{5.4}$$

with the kth cell dividing into two cells when gk exceeds $\sqrt[3]{2}$. Here, σ_1 is a uniformly distributed random variable between 0 and 1, and ζ is the cell cycle time. For spatial integration of the growth function of our model, we scale the Morse potential functions accordingly:

$$\mu\frac{d\boldsymbol{y}_k}{dt} = -\Sigma_{O(i)}V(|\boldsymbol{y}_k - \boldsymbol{y}_i|) \tag{5.5}$$

As a result, cells become physically larger in the tissue network before they divide. When a cell divides in our model, we place the cell at a randomly chosen angle θ, at an ϵ distance away. When the cell divides the mother cell cells is given a new g_k of $1 + \sigma_2$ and the offspring is assigned $g_{N+1} = \sqrt[3]{2 - g_k^3}$. Figure 5.3 demonstrates a representation of a network of cells before and after growth occurs, with and without cell division.

Finally, we assume that the domain we assume that the domain in which the cells grow is restricted by a pre-formed extra-cellular environment, which restricts movement ventrally and laterally, but allows the tissue to grow upward. In order to do this we impose strict boundaries on our movement, whereby a cell which is slated to move outside the boundary from eq. (5.2) does not move that time step.

Parameters for all simulations can be found in Appendix E.

5.2.2 Morphogens and the Gene Regulatory Network

The morphogens Edn (E) and BMP (B) are produced outside and ventral to the pharangeal arch, and create a gradient which is high ventrally and low dorsally. Due to our assumption that the tissue growth is restricted to a specified environment, we model diffusion in a growing rectangular domain where the left, right, and dorsal edges have reflective boundary conditions, while the ventral edge has Dirichlet boundary conditions whose values are α_E and α_B, for Edna and BMP, respectively. The equations for the morphogens are:

$$\frac{\partial E}{\partial t} = D_E \Delta E - r_E E \tag{5.6}$$

$$\frac{\partial B}{\partial t} = D_B \Delta B - r_B B \tag{5.7}$$

$$\tag{5.8}$$

Where D_E and D_B are diffusion coefficients and r_E and r_B are degradation rates.

Since the boundary in which the cells grow is known and there is no influence from the system to the morphogens, we can solve for the steady state of E and B for use throughout the simulation.

To incorporate the effect of the morphogens on the gene network we calculate the weighted value of the morphogens at the four grid-points surrounding the cell center of mass, giving us the concentration of Edn and BMP inside cell k,E_k and B_k.

The equations describing the gene-regulatory network are:

$$\frac{\partial J}{\partial t} = J_M \frac{b_J + (\gamma_{J1}S)^2}{1 + (\gamma_{J1}S)^2 + (\gamma_{J2}E)^2 + (\gamma_{J3}D)^2 + (\gamma_{J4}H)^2} - r_J J \tag{5.9}$$

$$\frac{\partial N}{\partial t} = N_M \frac{b_N + (\gamma_{N1}S)^2}{1 + (\gamma_{N1}S)^2} - r_N N \tag{5.10}$$

$$\frac{\partial D}{\partial t} = D_M \frac{b_D + (\gamma_{D1}B)^2 + (\gamma_{D2}E)^2}{1 + (\gamma_{D1}B)^2 + (\gamma_{D2}E)^2 + (\gamma_{D3}H)^2 + (\gamma_{D4}J)^2} - r_D D \tag{5.11}$$

$$\frac{\partial H}{\partial t} = H_M \frac{b_H + (\gamma_{H1}B)^2}{1 + (\gamma_{H1}B)^2 + (\gamma_{H2}D)^2} - r_H H \tag{5.12}$$

Where, J, N, D, and H are the genes Jag, Notch, Dlx and Hand with degradation rates r_J, r_N, r_D, and r_H, respectively. J_M, N_M, D_M, and H_M represents a maximum production rate, b_J, b_N, b_D, and b_H are basal production rates, and γ's are EC50 values for each interaction. S represents a signal which is turned on by notch-jag binding and is defined as:

$$\frac{\partial S}{\partial t} = k_{on} N \Sigma_{O(i)} J_i - r_S S \tag{5.13}$$

Where k_{on} is a binding rate between cell surface notch and the jag neighboring cells i, and $r_S S$ is the degradation rate of the signal in the cell.

5.3 Results

Our simulations of the system for zebrafish pharyngeal jaw development captures the observed spatial and temporal patterning phenomena. First the ventral and intermediate genes, Hand and Dlx, are expressed in the entire tissue (fig. 5.4 A). As the tissue grows dorsally, the expression the intermediate and ventral boundary begins to form, as Hand remains expressed in the more dorsal region of the arch, while Dlx is expressed in the dorsal region of the arch (fig. 5.4 B). Finally, Jag expression is turned on in the most dorsal portion of the arch, forming the dorsal-intermediate boundary with Dlx (fig. 5.4 C).

Next we use the model to study the purpose of the notch jag signaling present in the system. We find that by turning off notch signaling in the system $\gamma_{j1} = 0$, the system has a higher difficulty patterning the dorsal-intermediate boundary. When J_M is low the boundary fails to form (fig. 5.5 A). This is due to Jag being unable to express high enough levels to down-regulate Dlx in the dorsal region, meanwhile Dlx is able to remain high enough to down-regulate Jag. When J_M is increased past a certain threshold then the dorsal-intermediate boundary formation occurs (fig. 5.5 B,C). Conversely, when notch signaling is enabled, pharyngeal arch with low J_M forms dorsal boundary. The notch signaling provides the dorsal cells with a way to overcome the down-regulation of Jag by Dlx and up-regulate Jag production allowing the dorsal-intermediate boundary to form (fig. 5.6 A). When J_M is increased, the dorsal-intermediate boundary shifts ventrally, decreasing the intermediate domain size while increasing the dorsal domain size (fig. 5.6 B), which is consistent with results found in experiments [137]. Interestingly the sharpness of the dorsal intermediate boundary appears to be unaffected by the increase in J_M. We also note that there is no difference between the boundary sharpness with and without notch signaling. Most likely the signaling is present to aid in ensuring the dorsal intermediate boundary forms, while the boundary sharpness is determined by the mutual inhibition of Jag and Dlx.

5.4 Conclusion

As an organism or tissue develops, some of its primary functions are to grow and pattern simultaneously. The zebrafish pharyngeal arch serves as a great model to study the morphogenesis of a biological system which is dependent on several temporal and spacial scales.

In this chapter, we developed a discrete tissue model framework for the zebrafish pharyngeal arch that accounts for growth, bio-mechanical cell-cell interaction, cell-cell signaling, gradient formation and gene regulation. Our model is able to capture the experimental results of both the spatial and temporal dynamics of boundary specification. The initial formation of a ventral intermediate boundary arises quickly due to the dual Edn and Bmp gradients. The tissue must grow to a certain size before the formation of the dorsal region. This is due to the Edn concentration decreasing as the tissue grows dorsally.

The model predicts that the presence of a Notch-Jag signaling mechanism adds robustness to the formation of the dorsal region. Though the region is able to form without the presence of notch signaling, it must have a very high production rate to do so. Notch signaling is able to overcome this and the tissue can form properly with a lower maximum production rate of Jag. Interestingly, notch signaling appears to have little or no influence on boundary sharpening. The model simulations show that the boundary is not sharpened by the addition of notch-jag signaling pathway. Instead the tissue relies on the mutual inhibition between Jag and Dlx to sharpen the dorsal intermediate boundary, and between Hand and Dlx to sharpen the ventral intermediate boundary.

While the modeling framework presented here focuses on the pharyngeal development of zebrafish, it can be useful in several other tissues in which cell-cell contact signaling and bio-mechanics are of interest such as the drosophila eye and wing disc [139], or its role in tumorogenesis [140].

5.5 Figures
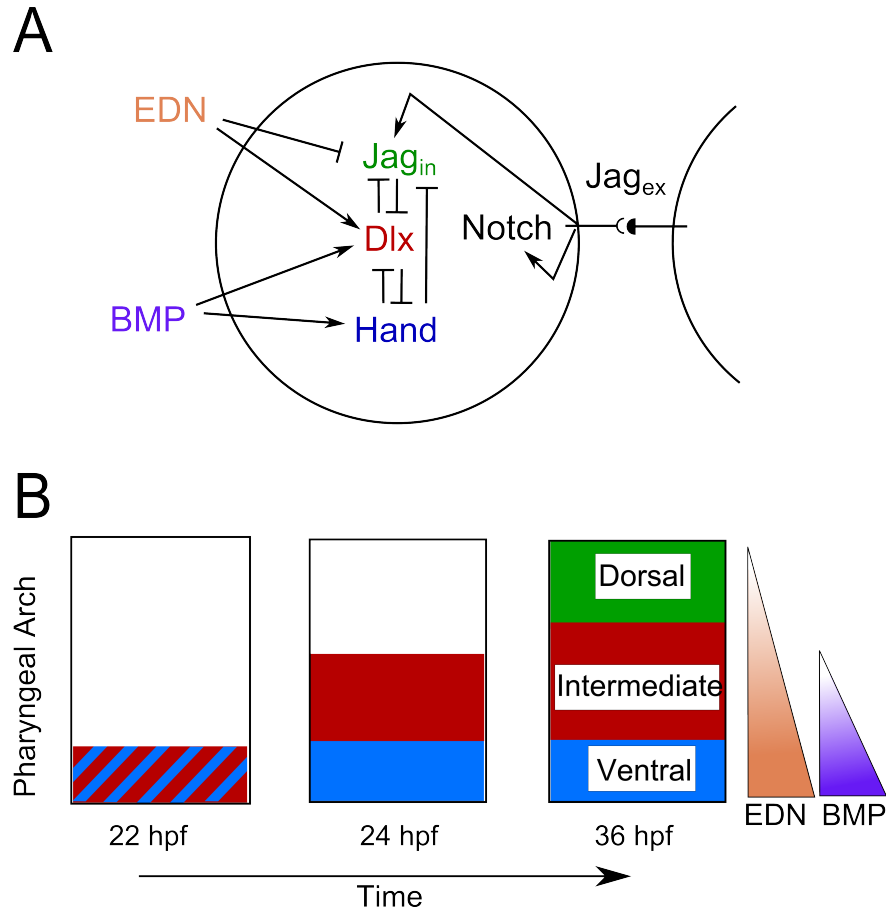
Figure 5.1: (A) schematic diagram of gene regulatory network regulating region specification in zebrafish pharyngeal arch. Edn and Bmp are morphogen gradients produced ventral to the arch. (B) Schematic of temporal and spacial patterning of the arch formation. The arch regions are specified initially in the most ventral region, expressing Dlx, and eventual intermediate gene marker, and Hand, the ventral marker. As time evolves the arch grows dorsally and the ventral-intermediate boundary is formed. The Dorsal-intermediate boundary is formed last, and is specified by Jag expression.
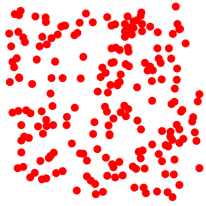
Initial State   Steadt State
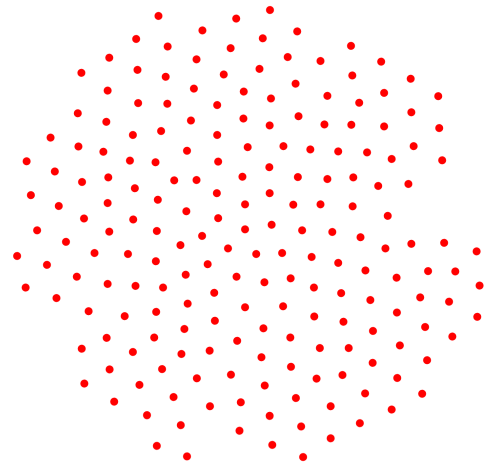
Figure 5.2: Cell center of mass distribution before and after time evolution.
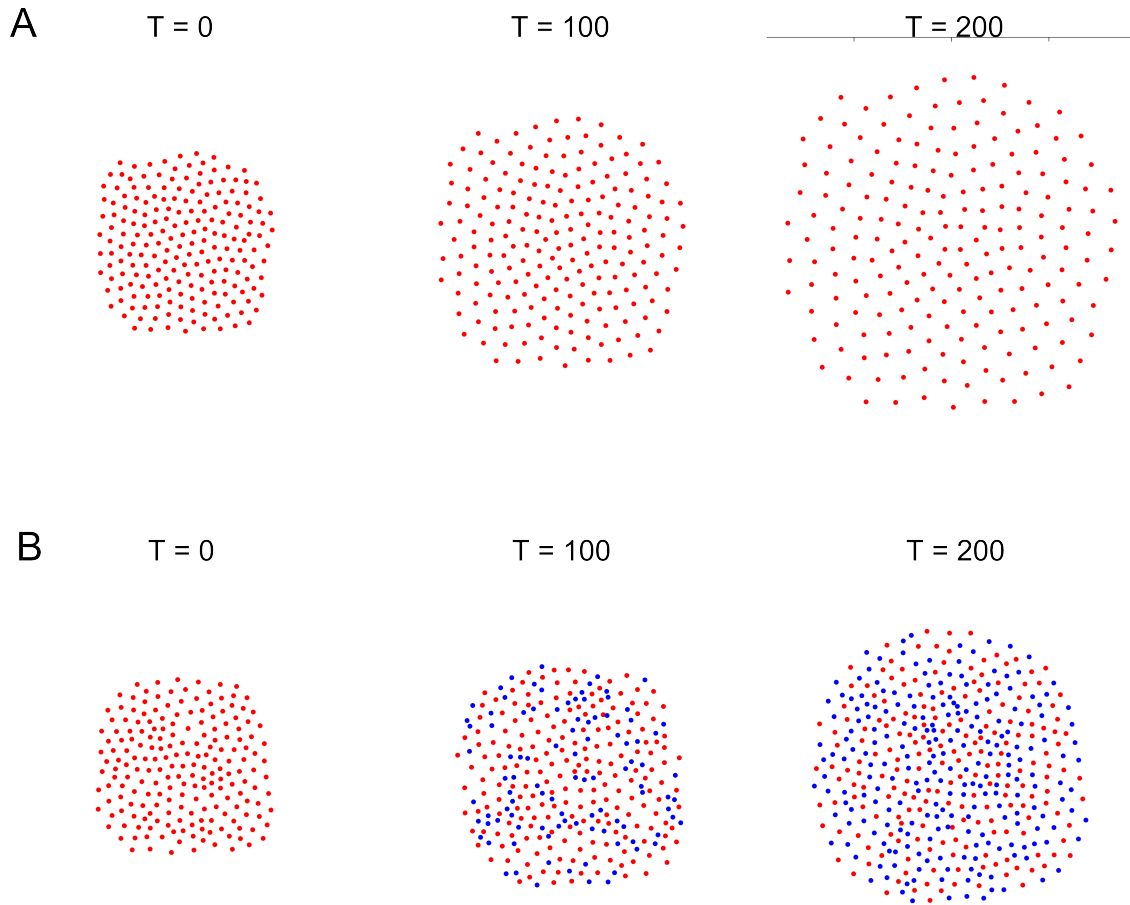
Figure 5.3: Cell center of mass distribution when tissue growth is enabled. (A) Cells grow but do not undergo cell division. (B) Cells grow and undergo cell division when their radius reaches a certain threshold. Red marker represents initial population of cells, blue markers are offspring cells.
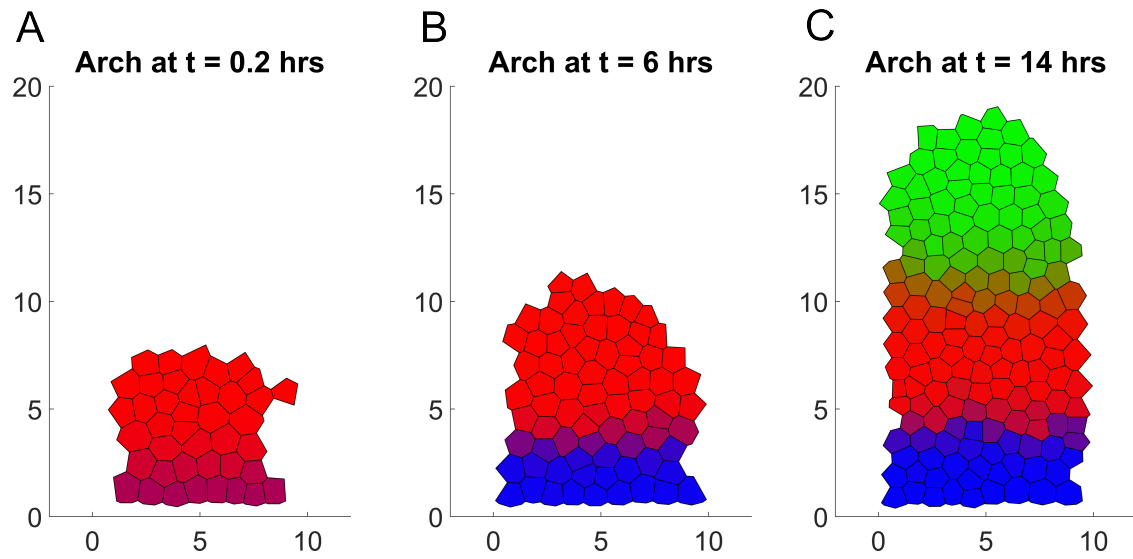
Figure 5.4: Tissue growth and patterning in pharyngeal arch. (A) Early time shows no clear ventral intermediate boundary. (B) Ventral intermediate regions form separated by a sharp boundary. (C) Dorsal region is final region to develop.
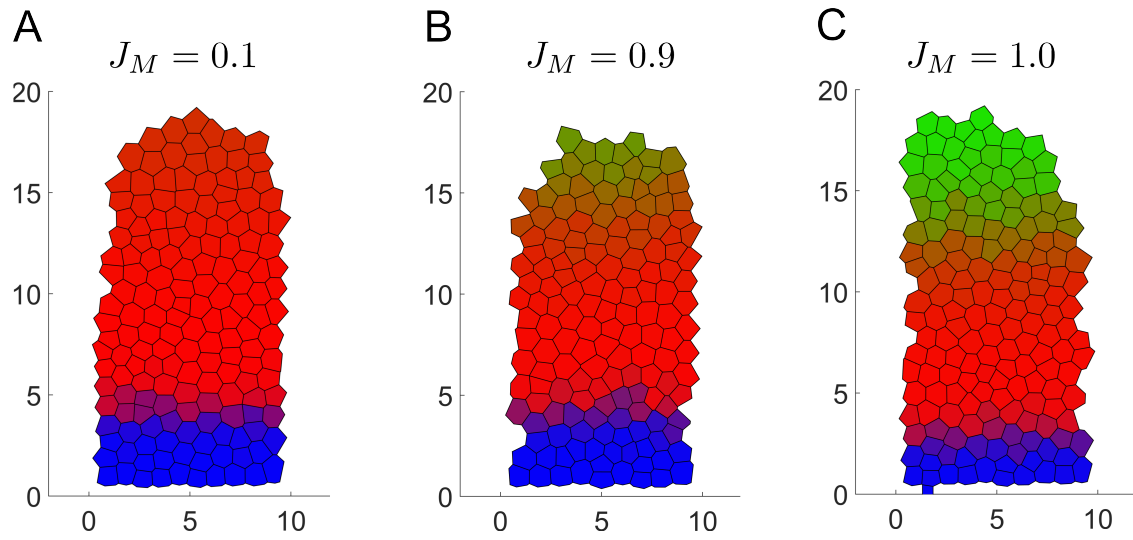
Figure 5.5: Pharyngeal arch without Notch signaling. (A) Tissue with low max production rate (J_M) of jag fails to form a dorsal boundary. (B,C) Increase in J_M forms dorsal boundary
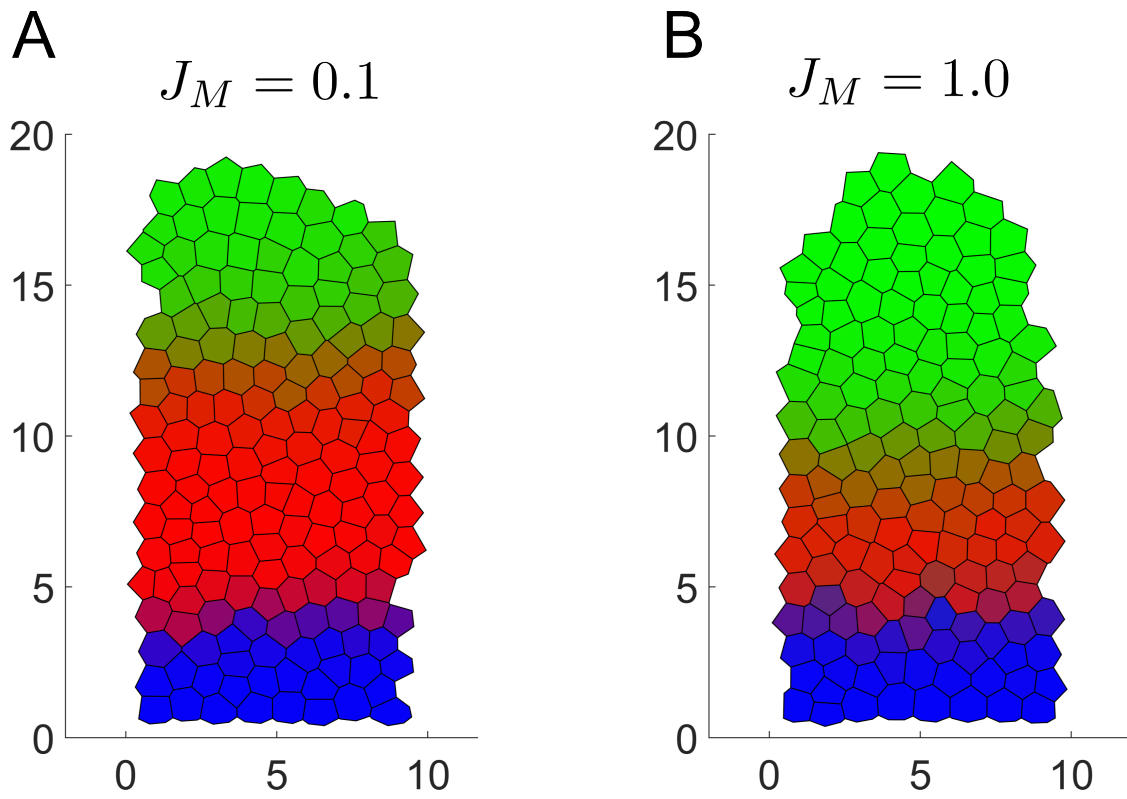
Figure 5.6: Pharyngeal arch with Notch signaling. (A) Dorsal boundary forms with low J_M. (B) Dorsal region expands ventraly as J_M increases.

Chapter 6

Conclusion

Now that more and more biological knowledge at the biochemical, cellular, and tissue level is accumulating, it is important to find unified understandings and make sense of this well-correlated information. Mathematical modeling of biological tissues serves as a particularly useful avenue to achieve this. Tissue models can account for multiple spatial and temporal scales to integrate several experimental findings, give insight into the occurrence of such findings, and perform new in silico experiments, though this process can pose significant challenges from computational and modeling standpoints.

The modeling studies performed in this thesis provide new insight on the roles of tissue and diseased morphogenesis in developmental biology. Spatial cell lineage models accounting for two moving interfaces in two dimensions revealed how the cell lineage properties in conjunction with the physical properties at the boundary can give rise to specialized forms for proper function in tissue found in the oral cavity. Moreover, pathological tissue shapes can be caused by the combination of improper cell-lineage and boundary properties. A multi-module feather model developed, allowed us to explore the regulatory system which gives rise to a diverse set of feather shape. Using the model in conjuction with experimental

findings we developed hypothesis on the role of cell shape changes in feather morphology, as well as gained a deeper understanding of the anisotropic RA topology in the evolution of feathers. Two distinct discrete cell models used in different biological systems allowed us to study the complex role of cell contact based signaling in boundary formation. The single cell tracking model is able to simulate the bio chemical and bio mechanical interactions between cells of irregular shapes, and the population dynamics of the tissue as a whole. The discrete cell network model of zebrafish pharyngeal arch development provided a way to study tissue growth and boundary specification in a temporal and spatial manner using morphogen gradients.

To arrive to these new findings, new tissue modeling frameworks needed to be developed. These innovative frameworks can be put to future use to answer more questions, study other biological systems, or be extended as newer discoveries are made about their model systems.

Bibliography

[1] K. B. Jones and O. D. Klein, "Oral epithelial stem cells in tissue maintenance and disease: the first steps in a long journey.," *International journal of oral science*, vol. 5, pp. 121–9, sep 2013.

[2] M. F. Gausti, "Analytic Geometry of Some Rectilinear Figures.," *Int. J. Educ. Sci. Technol.*, vol. 23, 1992.

[3] M. F. Gausti, A. Cobarrubias, F. J. R. Carrillo, and A. C. Rodriguez, "LCD Pixel Shape and Far-Field Diffraction Patterns.," *Optik*, vol. 116, 2005.

[4] M. S. Robinson, D. A. Sahlender, and S. D. Foster, "Rapid Inactivation of Proteins by Rapamycin-Induced Rerouting to Mitochondria," *Developmental Cell*, vol. 18, pp. 324–331, feb 2010.

[5] A. Tzur, R. Kafri, V. S. LeBleu, G. Lahav, and M. W. Kirschner, "Cell growth and size homeostasis in proliferating animal cells.," *Science (New York, N.Y.)*, vol. 325, pp. 167–71, jul 2009.

[6] A. I. Hamilton and H. J. Blackwood, "Cell renewal of oral mucosal epithelium of the rat.," *Journal of anatomy*, vol. 117, pp. 313–27, apr 1974.

[7] M. I. Koster and D. R. Roop, "Mechanisms Regulating Epithelial Stratification," *Annual Review of Cell and Developmental Biology*, vol. 23, pp. 93–113, nov 2007.

[8] I. H. Smart, "Location and orientation of mitotic figures in the developing mouse olfactory epithelium.," *Journal of anatomy*, vol. 109, pp. 243–51, jul 1971.

[9] S. Lowell, P. Jones, I. Le Roux, J. Dunne, and F. M. Watt, "Stimulation of human epidermal differentiation by DeltaNotch signalling at the boundaries of stem-cell clusters," *Current Biology*, vol. 10, pp. 491–500, may 2000.

[10] C. Jopling, E. Sleep, M. Raya, M. Martí, A. Raya, and J. C. Izpisúa Belmonte, "Zebrafish heart regeneration occurs by cardiomyocyte dedifferentiation and proliferation.," *Nature*, vol. 464, pp. 606–9, mar 2010.

[11] K. Kikuchi, J. E. Holdway, A. a. Werdich, R. M. Anderson, Y. Fang, G. F. Egnaczyk, T. Evans, C. a. Macrae, D. Y. R. Stainier, and K. D. Poss, "Primary contribution to

zebrafish heart regeneration by gata4(+) cardiomyocytes.," *Nature*, vol. 464, pp. 601–5, mar 2010.

[12] M. V. Plikus, M. Zeichner-David, J.-A. Mayer, J. Reyna, P. Bringas, J. G. M. Thewissen, M. L. Snead, Y. Chai, and C.-M. Chuong, "Morphoregulation of teeth: modulating the number, size, shape and differentiation by tuning Bmp activity.," *Evolution & development*, vol. 7, no. 5, pp. 440–57, 2005.

[13] X.-P. Wang, M. Suomalainen, S. Felszeghy, L. C. Zelarayan, M. T. Alonso, M. V. Plikus, R. L. Maas, C.-M. Chuong, T. Schimmang, and I. Thesleff, "An integrated gene regulatory network controls stem cell proliferation in teeth.," *PLoS biology*, vol. 5, p. e159, jun 2007.

[14] Z. Yue, T. X. Jiang, R. B. Widelitz, and C. M. Chuong, "Mapping stem cell activities in the feather follicle," *Nature*, vol. 438, pp. 1026–1029, 2005.

[15] S. J. Morrison and D. T. Scadden, "The bone marrow niche for haematopoietic stem cells.," *Nature*, vol. 505, pp. 327–34, jan 2014.

[16] C. Blanpain and B. D. Simons, "Unravelling stem cell dynamics by lineage tracing.," *Nature reviews. Molecular cell biology*, vol. 14, pp. 489–502, aug 2013.

[17] E. Fuchs, T. Tumbar, and G. Guasch, "Socializing with the Neighbors," *Cell*, vol. 116, pp. 769–778, mar 2004.

[18] K. A. Moore and I. R. Lemischka, "Stem cells and their niches.," *Science (New York, N.Y.)*, vol. 311, pp. 1880–5, mar 2006.

[19] A. J. Engler, S. Sen, H. L. Sweeney, and D. E. Discher, "Matrix elasticity directs stem cell lineage specification.," *Cell*, vol. 126, pp. 677–89, aug 2006.

[20] F. M. Watt and W. T. S. Huck, "Role of the extracellular matrix in regulating stem cell fate.," *Nature reviews. Molecular cell biology*, vol. 14, pp. 467–73, aug 2013.

[21] H. Thissen, G. Johnson, P. G. Hartley, P. Kingshott, and H. J. Griesser, "Two-dimensional patterning of thin coatings for the control of tissue outgrowth.," *Biomaterials*, vol. 27, pp. 35–43, jan 2006.

[22] A. Celli, S. Sanchez, M. Behne, T. Hazlett, E. Gratton, and T. Mauro, "The Epidermal Ca2+ Gradient: Measurement Using the Phasor Representation of Fluorescent Lifetime Imaging," *Biophysical Journal*, vol. 98, no. 5, pp. 911–921, 2010.

[23] H. Hennings, D. Michael, C. Cheng, P. Steinert, K. Holbrook, and S. H. Yuspa, "Calcium regulation of growth and differentiation of mouse epidermal cells in culture," *Cell*, vol. 19, pp. 245–254, jan 1980.

[24] M. P. Adams, D. G. Mallet, and G. J. Pettet, "Towards a quantitative theory of epidermal calcium profile formation in unwounded skin.," *PloS one*, vol. 10, p. e0116751, jan 2015.

[25] B. P. Chan and K. W. Leong, "Scaffolding in tissue engineering: general approaches and tissue-specific considerations.," *European spine journal : official publication of the European Spine Society, the European Spinal Deformity Society, and the European Section of the Cervical Spine Research Society*, vol. 17 Suppl 4, pp. 467–79, dec 2008.

[26] R. D. O'Dea, M. R. Nelson, A. J. El Haj, S. L. Waters, and H. M. Byrne, "A multiscale analysis of nutrient transport and biological tissue growth in vitro," *Mathematical Medicine and Biology*, vol. 32, pp. 345–366, sep 2015.

[27] F. M. Watt, "Engineered Microenvironments to Direct Epidermal Stem Cell Behavior at Single-Cell Resolution," *Developmental Cell*, vol. 38, no. 6, pp. 601–609, 2016.

[28] C.-M. Chuong and R. B. Widelitz, "The river of stem cells.," *Cell stem cell*, vol. 4, pp. 100–2, feb 2009.

[29] G. D. Frantz and S. K. McConnell, "Restriction of Late Cerebral Cortical Progenitors to an Upper-Layer Fate," *Neuron*, vol. 17, pp. 55–61, jul 1996.

[30] A. D. Lander, K. K. Gokoffski, F. Y. M. Wan, Q. Nie, and A. L. Calof, "Cell lineages and the logic of proliferative control.," *PLoS biology*, vol. 7, no. 1, p. e15, 2009.

[31] W.-C. Lo, C.-S. Chou, K. Gokoffski, F. Wan, A. Lander, A. Calof, and Q. Nie, "Feedback regulation in multistage cell lineages," *Mathematical Biosciences and Engineering*, vol. 6, no. 1, pp. 59–82, 2009.

[32] N. J. Savill, "Mathematical models of hierarchically structured cell populations under equilibrium with application to the epidermis," *Cell Proliferation*, vol. 36, pp. 1–26, feb 2003.

[33] A. Gandolfi, M. Iannelli, and G. Marinoschi, "An age-structured model of epidermis growth.," *Journal of mathematical biology*, vol. 62, pp. 111–41, jan 2011.

[34] H. Zhang, W. Hou, L. Henrot, S. Schnebert, M. Dumas, C. Heusèle, and J. Yang, "Modelling epidermis homoeostasis and psoriasis pathogenesis.," *Journal of the Royal Society, Interface / the Royal Society*, vol. 12, feb 2015.

[35] R. O'Dea, H. Byrne, and S. Waters, *Continuum Modelling of In Vitro Tissue Engineering: A Review*. Springer Berlin Heidelberg, 2012.

[36] C.-S. Chou, W.-C. Lo, K. K. Gokoffski, Y.-T. Zhang, F. Y. M. Wan, A. D. Lander, A. L. Calof, and Q. Nie, "Spatial Dynamics of Multistage Cell Lineages in Tissue Stratification," *Biophysj*, vol. 99, no. 10, pp. 3145–3154, 2010.

[37] P. Jones, "Stem cell patterning and fate in human epidermis," *Cell*, vol. 80, pp. 83–93, jan 1995.

[38] J. Ovadia and Q. Nie, "Numerical Methods for Two-Dimensional Stem Cell Tissue Growth," *Journal of Scientific Computing*, may 2013.

[39] T. A. Winning and G. C. Townsend, "Oral mucosal embryology and histology," *Clinics in Dermatology*, vol. 18, no. 5, pp. 499–511, 2000.

[40] S. M. Wise, J. S. Lowengrub, H. B. Frieboes, and V. Cristini, "Three-dimensional multispecies nonlinear tumor growth–I Model and numerical method.," *Journal of theoretical biology*, vol. 253, pp. 524–43, aug 2008.

[41] H. P. Greenspan, "On the growth and stability of cell cultures and solid tumors.," *Journal of theoretical biology*, vol. 56, pp. 229–42, jan 1976.

[42] R. A. Foty, C. M. Pfleger, G. Forgacs, and M. S. Steinberg, "Surface tensions of embryonic tissues predict their mutual envelopment behavior.," *Development (Cambridge, England)*, vol. 122, pp. 1611–20, may 1996.

[43] T. Lecuit and P.-F. Lenne, "Cell surface mechanics and the control of cell shape, tissue patterns and morphogenesis," *Nature Reviews Molecular Cell Biology*, vol. 8, pp. 633–644, aug 2007.

[44] J. Wang and G. Baker, "A numerical algorithm for viscous incompressible interfacial flows," *Journal of Computational Physics*, vol. 228, no. 15, pp. 5470–5489, 2009.

[45] J. Tang, E.-A. Ling, Y. Wu, and F. Liang, "Juxtanodin in the rat olfactory epithelium: specific expression in sustentacular cells and preferential subcellular positioning at the apical junctional belt.," *Neuroscience*, vol. 161, pp. 249–58, jun 2009.

[46] S. Gottlieb, "Total variation diminishing Runge-Kutta schemes," *Mathematics of Computation*, 1998.

[47] G. Sa, X. Xiong, T. Wu, J. Yang, S. He, and Y. Zhao, "Histological features of oral epithelium in seven animal species: As a reference for selecting animal models," *European Journal of Pharmaceutical Sciences*, vol. 81, pp. 10–17, 2016.

[48] X. Xiong, T. Wu, and S. He, "Physical forces make rete ridges in oral mucosa," *Medical Hypotheses*, vol. 81, no. 5, pp. 883–886, 2013.

[49] M. Kawasaki, K. Kawasaki, S. Oommen, J. Blackburn, M. Watanabe, T. Nagai, A. Kitamura, T. Maeda, B. Liu, R. Schmidt-Ullrich, T. Akiyama, J.-I. Inoue, N. L. Hammond, P. T. Sharpe, and A. Ohazama, "Regional regulation of Filiform tongue papillae development by Ikkα/Irf6," *Developmental Dynamics*, vol. 245, pp. 937–946, sep 2016.

[50] D. E. Cutright and H. Bauer, "Cell renewal in the oral mucosa and skin of the rat. I. Turnover time.," *Oral Surg Oral Med Oral Pathol*, vol. 23, no. 2, pp. 249–259, 1967.

[51] C. S. Potten, "Epidermal Cell Production Rates," *Journal of Investigative Dermatology*, vol. 65, pp. 488–500, dec 1975.

[52] J. R. Bickenbach, "Identification and behavior of label-retaining cells in oral mucosa and skin.," *Journal of dental research*, pp. 1611–20, aug 1981.

[53] J. R. Bickenbach and I. C. Mackenzie, "Identification and Localization of Label-Retaining Cells in Hamster Epithelia," *Journal of Investigative Dermatology*, vol. 82, pp. 618–622, jun 1984.

[54] T. Asaka, M. Akiyama, Y. Kitagawa, and H. Shimizu, "Higher density of label-retaining cells in gingival epithelium," *Journal of Dermatological Science*, vol. 55, pp. 132–134, aug 2009.

[55] C. A. Squier and M. J. Kremer, "Biology of oral mucosa and esophagus.," *Journal of the National Cancer Institute. Monographs*, vol. 2001, no. 29, pp. 7–15, 2001.

[56] P. Viswanathan, M. Guvendiren, W. Chua, S. B. Telerman, K. Liakath-Ali, J. A. Burdick, and F. M. Watt, "Mimicking the topography of the epidermaldermal interface with elastomer substrates," *Integr. Biol.*, vol. 8, no. 1, pp. 21–29, 2016.

[57] R. Parisi, D. P. M. Symmons, C. E. M. Griffiths, and D. M. Ashcroft, "Global epidemiology of psoriasis: a systematic review of incidence and prevalence.," *The Journal of investigative dermatology*, vol. 133, pp. 377–85, mar 2013.

[58] A. M. Bowcock and J. G. Krueger, "Getting under the skin: the immunogenetics of psoriasis.," *Nature reviews. Immunology*, vol. 5, pp. 699–711, sep 2005.

[59] E. F. Wagner, H. B. Schonthaler, J. Guinea-Viniegra, and E. Tschachler, "Psoriasis: what we have learned from mouse models.," *Nature reviews. Rheumatology*, vol. 6, pp. 704–14, dec 2010.

[60] M. A. Lowes, A. M. Bowcock, and J. G. Krueger, "Pathogenesis and therapy of psoriasis.," *Nature*, vol. 445, pp. 866–73, feb 2007.

[61] G. D. Weinstein and J. L. McCullough, "Cytokinetics in diseases of epidermal hyperplasia.," *Annual review of medicine*, vol. 24, pp. 345–52, jan 1973.

[62] M. El-Domyati, N. H. Moftah, G. A. Nasif, H. M. Abdel-Wahab, M. T. Barakat, and R. T. Abdel-Aziz, "Evaluation of apoptosis regulatory proteins in response to PUVA therapy for psoriasis.," *Photodermatology, photoimmunology & photomedicine*, vol. 29, pp. 18–26, feb 2013.

[63] F. Meisgen, N. Xu, T. Wei, P. C. Janson, S. Obad, O. Broom, N. Nagy, S. Kauppinen, L. Kemény, M. Ståhle, A. Pivarcsi, and E. Sonkoly, "MiR-21 is up-regulated in psoriasis and suppresses T cell apoptosis.," *Experimental dermatology*, vol. 21, pp. 312–4, apr 2012.

[64] M. Laporte, P. Galand, D. Fokan, C. de Graef, and M. Heenen, "Apoptosis in established and healing psoriasis.," *Dermatology (Basel, Switzerland)*, vol. 200, pp. 314–6, jan 2000.

[65] S. P. Higgins, M. Freemark, and N. S. Prose, "Acanthosis Nigricans: A practical approach to evaluation and management," *Dermatology Online Journal*, vol. 14, sep 2008.

[66] Z. Kutlubay, B. Engin, O. Bairamov, and Y. Tüzün, "Acanthosis Nigricans: A Fold (Intertriginous) Dermatosis," *Clinics in Dermatology*, apr 2015.

[67] P. Litonjua, A. Piñero-Piloña, L. Aviles-Santa, and P. Raskin, "Prevalence of acanthosis nigricans in newly-diagnosed type 2 diabetes.," *Endocrine practice : official journal of the American College of Endocrinology and the American Association of Clinical Endocrinologists*, vol. 10, pp. 101–6, jan 2004.

[68] A. S. Kong, R. L. Williams, R. Rhyne, V. Urias-Sandoval, G. Cardinali, N. F. Weller, B. Skipper, R. Volk, E. Daniels, B. Parnes, and L. McPherson, "Acanthosis Nigricans: high prevalence and association with diabetes in a practice-based research network consortium–a PRImary care Multi-Ethnic network (PRIME Net) study.," *Journal of the American Board of Family Medicine : JABFM*, vol. 23, pp. 476–85, jan 2010.

[69] P. D. Cruz Jr. and J. A. Hud Jr., "Excess Insulin Binding to Insulin-Like Growth Factor Receptors: Proposed Mechanism for Acanthosis Nigricans.," *Journal of Investigative Dermatology*, vol. 98, pp. 82S–85S, jun 1992.

[70] C. Lv, S. Song, W. Luo, P. M. Elias, and M.-Q. Man, "Cutaneous resonance running time is decreased in psoriatic lesions.," *Skin research and technology : official journal of International Society for Bioengineering and the Skin (ISBS) [and] International Society for Digital Imaging of Skin (ISDIS) [and] International Society for Skin Imaging (ISSI)*, vol. 18, pp. 232–7, may 2012.

[71] J. Ovadia and Q. Nie, "Stem Cell Niche Structure as an Inherent Cause of Undulating Epithelial Morphologies," *Biophysj*, vol. 104, no. 1, pp. 237–246, 2013.

[72] A. K. Langton, P. Halai, C. E. Griffiths, M. J. Sherratt, and R. E. Watson, "The impact of intrinsic ageing on the protein composition of the dermal-epidermal junction." 2016.

[73] F. H. Silver, L. M. Siperko, and G. P. Seehra, "Mechanobiology of force transduction in dermal tissue," *Skin Research and Technology*, vol. 9, pp. 3–23, feb 2003.

[74] R. O. Prum and A. H. Brush, "The evolutionary origin and diversification of feathers," *Q. Rev. Biol.*, vol. 77, pp. 261–295, 2002.

[75] X. Xu, "An integrative approach to understanding bird origins," *Science*, vol. 346, 2014.

[76] C. M. Chuong, "Adaptation to the sky: defining the feather with integument fossils from mesozoic China and experimental evidence from molecular laboratories," *J. Exp. Zool. B Mol. Dev. Evol.*, vol. 298, pp. 42–56, 2003.

[77] X. Xu, X. Zheng, and H. You, "Exceptional dinosaur fossils show ontogenetic development of early feathers," *Nature*, vol. 464, pp. 1338–1341, 2010.

[78] L. M. Chiappe, *No Glorified Dinosaurs: The Origin And Early Evolution Of Birds*, vol. 263. John Wiley, 2007.

[79] X. Xu, Z. Zhou, and R. O. Prum, "Branched integumental structures in Sinornithosaurus and the origin of feathers," *Nature*, vol. 410, pp. 200–204, 2001.

[80] C. F. Chen, "Development, regeneration, and evolution of feathers," *Annu. Rev. Anim. Biosci.*, vol. 3, pp. 169–195, 2015.

[81] C. M. Chuong, R. Chodankar, R. B. Widelitz, and T. X. Jiang, "Evo-devo of feathers and scales: building complex epithelial appendages," *Curr. Opin. Genet. Dev.*, vol. 10, pp. 449–456, 2000.

[82] A. Feduccia and H. B. Tordoff, "Feathers of archaeopteryx: asymmetric vanes indicate aerodynamic function," *Science*, vol. 203, pp. 1021–1022, 1979.

[83] G. S. Paul, *Dinosaurs Of The Air: The Evolution And Loss Of Flight In Dinosaurs And Birds*, vol. 460. Johns Hopkins University Press, 2002.

[84] C. J. Pennycuick, *Modelling The Flying Bird*, vol. 480. Academic Press, 2008.

[85] G. Dyke, "Aerodynamic performance of the feathered dinosaur Microraptor and the evolution of feathered flight," *Nat. Commun.*, vol. 4, p. 2489, 2013.

[86] S. D. Scott and C. McFarland, *Bird Feathers: A Guide To North American Species*. Stackpole Books, 2010.

[87] P. Lucas and A. Stettenheim, *Avian Anatomy Integument. Usda Agriculture Handbook*, vol. Vol. 362. 1972.

[88] M. Yu, P. Wu, R. B. Widelitz, and C. M. Chuong, "The morphogenesis of feathers," *Nature*, vol. 420, pp. 308–312, 2002.

[89] M. P. Harris, S. Williamson, J. F. Fallon, H. Meinhardt, and R. O. Prum, "Molecular evidence for an activator-inhibitor mechanism in development of embryonic feather branching," *Proc. Natl Acad. Sci. Usa*, vol. 102, pp. 11734–11739, 2005.

[90] Z. Yue, T. X. Jiang, R. B. Widelitz, and C. M. Chuong, "Wnt3a gradient converts radial to bilateral feather symmetry via topological arrangement of epithelia," *Proc. Natl Acad. Sci. Usa*, vol. 103, pp. 951–955, 2006.

[91] R. O. Prum and S. Williamson, "Theory of the growth and evolution of feather shape," *J. Exp. Zool.*, vol. 291, pp. 30–57, 2001.

[92] A. Q. Cai, "Cellular retinoic acid-binding proteins are essential for hindbrain patterning and signal robustness in zebrafish," *Development*, vol. 139, pp. 2150–2155, 2012.

[93] L. Shen and Z. Chen, "Critical review of the impact of tortuosity on diffusion," *Chemical Engineering Science*, vol. 62, no. 14, pp. 3748–3755, 2007.

[94] K. A. Rejniak, V. Estrella, T. Chen, A. S. Cohen, M. C. Lloyd, and D. L. Morse, "The role of tumor tissue architecture in treatment penetration and efficacy: an integrative study.," *Frontiers in oncology*, vol. 3, p. 111, jan 2013.

[95] J. Vermot, "Retinoic acid controls the bilateral symmetry of somite formation in the mouse embryo," *Science*, vol. 308, pp. 563–566, 2005.

[96] C. Mou, "Cryptic patterning of avian skin confers a developmental facility for loss of neck feathering," *P Lo S Biol.*, vol. 9, p. e1001028, 2011.

[97] M. Rhinn and P. Dollé, "Retinoic acid signalling during development.," *Development (Cambridge, England)*, vol. 139, pp. 843–58, mar 2012.

[98] K. M. Crawford and P. C. Zambryski, "Plasmodesmata signaling: many roles, sophisticated statutes.," *Current opinion in plant biology*, vol. 2, pp. 382–7, oct 1999.

[99] N. Kirschner, R. Rosenthal, M. Furuse, I. Moll, M. Fromm, and J. M. Brandner, "Contribution of Tight Junction Proteins to Ion, Macromolecule, and Water Barrier in Keratinocytes," *Journal of Investigative Dermatology*, vol. 133, pp. 1161–1169, may 2013.

[100] A. Li, S. Figueroa, T.-X. Jiang, P. Wu, R. Widelitz, Q. Nie, and C.-M. Chuong, "Diverse feather shape evolution enabled by coupling anisotropic signalling modules with self-organizing branching programme," *Nature Communications*, vol. 8, p. ncomms14139, jan 2017.

[101] A. Baroni, E. Buommino, V. De Gregorio, E. Ruocco, V. Ruocco, and R. Wolf, "Structure and function of the epidermis related to barrier properties," *Clinics in Dermatology*, vol. 30, pp. 257–262, may 2012.

[102] R. G. Thakar, Q. Cheng, S. Patel, J. Chu, M. Nasir, D. Liepmann, K. Komvopoulos, and S. Li, "Cell-shape regulation of smooth muscle cell proliferation.," *Biophysical journal*, vol. 96, pp. 3423–32, apr 2009.

[103] D. Stekel, J. Rashbass, and E. D. Williams, "A computer graphic simulation of squamous epithelium.," *Journal of theoretical biology*, vol. 175, pp. 283–93, aug 1995.

[104] T. Sutterlin, S. Huber, H. Dickhaus, and N. Grabe, "Modeling multi-cellular behavior in epidermal tissue homeostasis via finite state machines in multi-agent systems," *Bioinformatics*, vol. 25, pp. 2057–2063, aug 2009.

[105] T. Sütterlin, E. Tsingos, J. Bensaci, G. N. Stamatas, and N. Grabe, "A 3D self-organizing multicellular epidermis model of barrier formation and hydration with realistic cell morphology based on EPISIM," *Scientific Reports*, vol. 7, p. 43472, mar 2017.

[106] G. Grise and M. Meyer-Hermann, "Towards sub-cellular modeling with delaunay triangulation," *Mathematical Modelling of Natural Phenomena*, vol. 5, no. 1, pp. 224–238, 2010.

[107] S. M. Albelda and C. A. Buck, "Integrins and other cell adhesion molecules," *The FASEB Journal*, vol. 4, no. 11, pp. 2868–80, 1990.

[108] T. J. Newman, "Modeling Multicellular Systems Using Subcellular Elements," *Mathematical Biosciences and Engineering*, vol. 2, pp. 613–624, aug 2005.

[109] J. C. Dallon and H. G. Othmer, "How cellular movement determines the collective force generated by the Dictyostelium discoideum slug," *Journal of Theoretical Biology*, vol. 231, no. 2, pp. 203–222, 2004.

[110] A. T. L. Van Lommel, *From Cells to Organs.* Kluwer Academic Publishers, 2003.

[111] E. M. Marieb, *Human Anatomy and Physiology.* Benjamin-Cummings, 3rd ed. ed., 1995.

[112] G. Alefeld and J. Herzberger, *Introduction to Interval Analysis.* New York: Academic Press, 1983.

[113] M. Mangel and M. B. Bonsall, "Phenotypic Evolutionary Models in Stem Cell Biology: Replacement, Quiescence, and Variability," *PloS one*, vol. 3, no. 2, p. e1591, 2008.

[114] S. J. Morrison and J. Kimble, "Asymmetric and symmetric stem-cell divisions in development and cancer.," *Nature*, vol. 441, pp. 1068–74, jun 2006.

[115] E. Clayton, D. P. Doupé, A. M. Klein, D. J. Winton, B. D. Simons, and P. H. Jones, "A single type of progenitor cell maintains normal epidermis.," *Nature*, vol. 446, pp. 185–9, mar 2007.

[116] D. T. Gillespie, "Exact stochastic simulation of coupled chemical reactions," *J. Phys. Chem.*, vol. 81, no. 25, pp. 2340–2361, 1977.

[117] D. T. Gillespie, A. Hellander, and L. R. Petzold, "Perspective: Stochastic algorithms for chemical kinetics.," *The Journal of chemical physics*, vol. 138, p. 170901, may 2013.

[118] D. Rogulja, C. Rauskolb, and K. D. Irvine, "Morphogen control of wing growth through the Fat signaling pathway.," *Developmental cell*, vol. 15, pp. 309–21, aug 2008.

[119] A. M. Turing and R. S. Great Britain, "The Chemical Basis of Morphogenesis," *Philosophical Transactions of the Royal Society of London. Series B, Biological Sciences*, vol. 237, p. 36, 1952.

[120] H. Meinhardt, *The Algorithmic Beauty of Sea Shells.* Springer, 4 ed., 2009.

[121] A. Gierer and H. Meinhardt, "A theory of biological pattern formation," *Kybernetik*, vol. 12, pp. 30–39, dec 1972.

[122] S. Kondo and T. Miura, "Reaction-Diffusion Model as a Framework for Understanding Biological Pattern Formation," *Science*, vol. 329, no. 5999, 2010.

[123] J. B. A. Green and J. Sharpe, "Positional information and reaction-diffusion: two big ideas in developmental biology combine.," *Development (Cambridge, England)*, vol. 142, pp. 1203–11, apr 2015.

[124] S. A. Ting-Berreth and C. M. Chuong, "Sonic Hedgehog in feather morphogenesis: induction of mesenchymal condensation and association with cell death," *Dev. Dyn.*, vol. 207, pp. 157–170, 1996.

[125] A. Li, Y.-C. Lai, S. Figueroa, T. Yang, R. B. Widelitz, K. Kobielak, Q. Nie, and C. Ming Chuong, "Deciphering principles of morphogenesis from temporal and spatial patterns on the integument.," *Developmental dynamics : an official publication of the American Association of Anatomists*, apr 2015.

[126] M. Sato, T. Yasugi, Y. Minami, T. Miura, and M. Nagayama, "Notch-mediated lateral inhibition regulates proneural wave propagation when combined with EGF-mediated reaction diffusion.," *Proceedings of the National Academy of Sciences of the United States of America*, vol. 113, pp. E5153–62, aug 2016.

[127] M. Boareto, M. K. Jolly, A. Goldman, M. Pietilä, S. A. Mani, S. Sengupta, E. Ben-Jacob, H. Levine, and J. N. Onuchic, "Notch-Jagged signalling can give rise to clusters of cells exhibiting a hybrid epithelial/mesenchymal phenotype," *Journal of The Royal Society Interface*, vol. 13, no. 118, 2016.

[128] A. Louvi and S. Artavanis-Tsakonas, "Notch signalling in vertebrate neural development," *Nature Reviews Neuroscience*, vol. 7, pp. 93–102, feb 2006.

[129] R. Crowe, D. Henrique, D. Ish-Horowicz, and L. Niswander, "A new role for Notch and Delta in cell fate decisions: patterning the feather array," *Development*, vol. 125, no. 4, 1998.

[130] A. Li, M. Chen, T.-X. Jiang, P. Wu, Q. Nie, R. Widelitz, and C.-M. Chuong, "Shaping organs by a wingless-int/Notch/nonmuscle myosin module which orients feather bud elongation.," *Proceedings of the National Academy of Sciences of the United States of America*, vol. 110, pp. E1452–61, apr 2013.

[131] M. Wardetzky, S. Mathur, F. Kaelberer, and E. Grinspun, "Discrete Laplace operators: No free lunch," jan 2007.

[132] M. Boareto, M. K. Jolly, M. Lu, J. N. Onuchic, C. Clementi, and E. Ben-Jacob, "JaggedDelta asymmetry in Notch signaling can give rise to a Sender/Receiver hybrid phenotype," *Proceedings of the National Academy of Sciences*, vol. 112, pp. E402–E409, feb 2015.

[133] D. Sprinzak, A. Lakhanpal, L. Lebon, L. A. Santat, M. E. Fontes, G. A. Anderson, J. Garcia-Ojalvo, and M. B. Elowitz, "Cis-interactions between Notch and Delta generate mutually exclusive signalling states.," *Nature*, vol. 465, pp. 86–90, may 2010.

[134] D. del Álamo, H. Rouault, and F. Schweisguth, "Mechanism and Significance of cis-Inhibition in Notch Signalling," *Current Biology*, vol. 21, no. 1, pp. R40–R47, 2011.

[135] A. D. Lander, "Pattern, Growth, and Control," *Cell*, vol. 144, pp. 955–969, mar 2011.

[136] C. T. Miller, D. Yelon, D. Y. R. Stainier, and C. B. Kimmel, "Two endothelin 1 effectors, hand2 and bapx1, pattern ventral pharyngeal cartilage and the jaw joint.," *Development (Cambridge, England)*, vol. 130, pp. 1353–65, apr 2003.

[137] E. Zuniga, F. Stellabotte, and J. G. Crump, "Jagged-Notch signaling ensures dorsal skeletal identity in the vertebrate face.," *Development (Cambridge, England)*, vol. 137, pp. 1843–1852, jun 2010.

[138] L. Barske, A. Askary, E. Zuniga, B. Balczerski, P. Bump, J. T. Nichols, and J. G. Crump, "Competition between Jagged-Notch and Endothelin1 Signaling Selectively Restricts Cartilage Formation in the Zebrafish Upper Face," *PLOS Genetics*, vol. 12, p. e1005967, apr 2016.

[139] S. Artavanis-Tsakonas, M. D. Rand, and R. J. Lake, "Notch Signaling: Cell Fate Control and Signal Integration in Development," *Science*, vol. 284, no. 5415, 1999.

[140] F. Radtke and K. Raj, "The role of Notch in tumorigenesis: oncogene or tumour suppressor?," *Nature Reviews Cancer*, vol. 3, pp. 756–767, oct 2003.

Appendix A

A Spatial Cell Lineage Model for Healthy and Diseased Epidermis

All simulations are run using MATLAB 2016a. An N of 128 is chosen, with a time step of $\tau = \Delta X/4$.

Initial perturbation for all simulation unless otherwise stated is:

$$h_0\left(x, 0\right) = 0.2\cos\left(4\pi x\right), \quad h_1\left(x, 0\right) = 0.54$$

Parameters for all simulations unless otherwise stated are:

Variable	Value
p_0, p_1	1.0, 0.7
ν_0, ν_1	1, 1
d_0, d_1, d_2	0.1, 0.1, 1
K	1e-1
ξ_0, ξ_1	1e-4, 1e-2
k	3e-3
γ_0, γ_1	0.3, 0.7
m_0, m_1	10, 4
ς_0, ς_1, ς_2	0.1, 0.1, 0.1
n_0, n_1, n_2	2, 2, 2
D_{Ca}, D_N	1e-2, 1e-2
Ca_{deg}, N_{deg}	1, 0
μ_0, μ_1, μ_2	0, 1, 1
η_0, η_1, η_2	0, 0, 0
ζ_0, ζ_1, ζ_2	0, 0, 0
ρ_0, ρ_1, ρ_2	1, 0.5, 0.1
α_0, α_1	-200, 0
β_0, β_1	0.3, 0

Figure 1.3A:

Initial boundary conditions:

$$h_0\left(x, 0\right) = 0, \quad h_1\left(x, 0\right) = 0.54$$

Figure 1.4A:

Variable	Value
k	0

Figure 1.5A:

Variable	Value
ν_1	0.1
d_2	0.5

Figure 1.5B:

Variable	Value
ν_1	1
d_2	2

Figure 1.5C:

$$h_0\left(x, 0\right) = 0.2 \cos\left(8\pi x\right)$$

Variable	Value
ξ_0, ξ_1	1e-7, 1e-5
k	1e-4

For figure 1.6 the basal boundary was fixed and not allowed to evolve over time. The apical boundary remained dynamic, allowing the tissue to grow.

For figure 1.6A,D,G:

$$h_0\left(x, 0\right) = 0$$

For figure 1.6B,E,H:

$$h_0(x, 0) = B \cos(4\pi x)$$

For figure 1.6C,F,I:

$$h_0(x, 0) = B \cos(6\pi x)$$

Figure 1.6A,B,C:

Variable	Value
β_0, β_1	0.3, 0

Figure 1.6D,E,F:

Variable	Value
β_0, β_1	0.3, 0

Figure 1.6G,H,I:

Variable	Value
β_0, β_1	0.3, 0

For figure 6J, β_0 was varied between 0 and 1.

For figure 6J the basal boundary was fixed by equations, where was B varied between 0.1 and 0.4.

Figure 1.9C:

Variable	Value
ξ_0, $\xi_{\min}$	1e-3, 5e-5
D_A	1e-6
$A_{\deg}$	5
$P_{\max}$	10
α_0, $\alpha_{\min}$	-185, -15
ω_p	5e3
q_p	2
ω_c	2
q_c	2
ω_α	2
q_α	2
σ_0	0

Figure 1.10 Healthy Tissue:

Variable	Value
p_0, p_1	1.0, 0.5
ν_0, ν_1	1, 1
d_0, d_1, d_2	0, 0, 0.1
K	1e-1
ξ_0, ξ_1	5e-5, 5e-4
k	15e-4

Figure 1.10 Psoriatic Tissue:

Variable	Value
p_0, p_1	1.0, 0.4
ν_0, ν_1	1, 1.2
d_0, d_1, d_2	0, 0, 0.1
K	1e-1
ξ_0, ξ_1	5e-5, 2e-3
k	3e-4

Figure 1.10 AN Tissue:

Variable	Value
p_0, p_1	1.0, 0.9
ν_0, ν_1	1, 1.2
d_0, d_1, d_2	0.1, 0.1, 1
K	1e-1
ξ_0, ξ_1	5e-5, 5e-5
k	5e-4

Appendix B

A Multi-Regulatory Feather Model for Diverse Feather Shapes

All simulations are run using MATLAB 2016a. We solved the system of partial differential equations using a second order finite difference scheme in space. For the temporal discretization, the MRF model uses a fourth order Runge-Kutta time integration method while the PB model uses a first order Euler method. The MRF model is run to steady state. Different spatial resolutions have been used to test the code for the order of accuracy of the numerical method, including N = 200, 400 and 800, where N is the number of points for spatial discretization. Similarly, the temporal order of accuracy of the approximation has also been tested and studied

Parameters for the Multi-Module Regulatory Feather Model

Variable	Value
D_{RA}	[1e-2, 1e-1]
D_{WNT}	1e-2
D_{GDF}	1e-2
D_{GREM}	1e-2
V_{RAo}	[0, 1e-5]
V_R	2e-6
V_{GREM}	1e-6
B_{RAo}	1e-1
B_{WNT}	0.1
B_{GDF}	0
B_{GREM}	0
B_{CYP}	[0, 1e-1]
B_{BP}	[0, 1e-1]
ra_{deg}	1
r_{deg1}	1e-4
r_{deg2}	1e-5
bp_{deg1}	1e-4
bp_{deg2}	1e-5
rabp_{deg}	1e-1
wnt_{deg}	1e-4
gdf_{deg}	1e-4
grem_{deg}	1e-4
r_{on}	1e-3
r_{off}	1e-6
m_{on}	1
m_{off}	1e-3
j_α	1
j_β	1e-3
k_p	5e-1
k_1	1e-2
k_2	1e-1
k_3	4e-3
k_4	5e-5
k_5	1e-1
n_1	2
n_2	1
n_3	-1
n_4, n_5	-2
β	[0, .5]

Variable	Value
v_{cyp}	[1, 20]
v_{bp}	[1, 5]
v_{wnt}	[1, 5]
v_{gdf}	[1, 20]
a_{cyp}	[0, 15]
a_{bp}	[0, 1]
a_{wnt}	1
a_{gdf}	1

Parameters for the model of Periodic Branching model

Variable	Value
D_a	[8e-3, 2e-2]
D_b	[0.2, 0.5]
r_a	0.01
r_b	0.015
r_c	3e-4
b_a	[0, 1e-3]
b_b	[0.15, 0.3]
b_c	5e-4
s	1e-2
s_a	1.8
s_b	1.8
s_c	0.35
s_g	1e-3
n_g	-2

When modeling the retrogressed feathers (fig())In the PB and MRF models we replace the previously equations CHANGE THESE, which represent the spatially dependent production of CYP26B1 (CYP), CRABP1 (BP), WNT3A (WNT), and GDF10 (GDF), with equations B.1-B.4, B.5-B.8, B.9-B.12, or B.13-B.16 for each of the four feathers studied. All other equations for both the PB and MRF models remain unchanged.

For, $x \in [0, 1)$

Chicken primary remige

$$[CYP]_j = a_{\text{cyp}} * Exp[v_{\text{cyp}} \left(\sin \left(2\pi (x + 0.075) \right) - 1 \right)] + B_{\text{CYP}} \tag{B.1}$$

$$V_{\text{BP}} (x) = a_{\text{bp}} * Exp[v_{\text{bp}} \left(\sin \left(2\pi (x + 0.5) \right) - 1 \right)] + B_{\text{BP}} \tag{B.2}$$

$$V_{\text{WNT}} (x) = a_{\text{wnt}} * \left[1 + \left(v_{wnt1} \left(1 - \cos \left(2\pi x \right) \right) \right)^{\eta_{\text{wnt}}} \right]^{-1} \tag{B.3}$$

$$V_{\text{GDF}} (x) = a_{\text{gdf}} * Exp[v_{gdf1} \left(\cos \left(2\pi (x + 0.5) \right) - 1 \right)] \tag{B.4}$$

Chicken breast plume (with after-feather)

$$[CYP]_j = a_{\text{cyp}} \tag{B.5}$$

$$V_{\text{BP}} (x) = a_{\text{bp}} * \left[1 + \left(v_{\text{bp}} \left(1 - \kappa_{\text{bp}} \sin \left(2\pi x \right) \right) \right)^{\eta_{\text{wnt}}} \right]^{-1} \tag{B.6}$$

$$\begin{aligned} V_{\text{WNT}} (x) &= a_{\text{wnt}} * \left[1 + \left(v_{wnt1} \left(1 - \sin \left(2\pi x \right) \right) \right)^{\eta_{\text{wnt}}} \right]^{-1} \\ &+ a_{\text{wnt}} * \left[1 + \left(v_{wnt2} \left(1 - \sin \left(2\pi (x + 0.5) \right) \right) \right)^{\eta_{\text{wnt}}} \right]^{-1} \end{aligned} \tag{B.7}$$

$$\begin{aligned} V_{\text{GDF}} (x) &= a_{\text{gdf}} * \left[1 + \left(v_{gdf1} \left(1 - \sin \left(2\pi x \right) \right) \right)^{\eta_{\text{gdf}}} \right]^{-1} \\ &+ a_{\text{gdf}} * \left[1 + \left(v_{gdf2} \left(1 - \sin \left(2\pi (x + 0.5) \right) \right) \right)^{\eta_{\text{gdf}}} \right]^{-1} \end{aligned} \tag{B.8}$$

Ostrich primary remige

$$[CYP]_j = a_{\text{cyp}} \tag{B.9}$$

$$V_{\text{BP}} (x) = a_{\text{bp}} \tag{B.10}$$

$$V_{\text{WNT}} (x) = a_{\text{wnt}} * \left[1 + \left(v_{wnt1} \left(1 - \cos \left(2\pi x \right) \right) \right)^{\eta_{\text{wnt}}} \right]^{-1} \tag{B.11}$$

$$V_{\text{GDF}} (x) = a_{\text{gdf}} * Exp[v_{gdf1} \left(\cos \left(2\pi (x + 0.5) \right) - 1 \right)] \tag{B.12}$$

Emu primary remige

$$[CYP]_j = a_{\text{cyp}} \tag{B.13}$$

$$V_{\text{BP}}(x) = a_{\text{bp}} \tag{B.14}$$

$$V_{\text{WNT}}(x) = a_{\text{wnt}} * \left[1 + (v_{wnt1}(1 - \sin(2\pi x)))^{\eta_{\text{wnt}}}\right]^{-1}$$
$$+ a_{\text{wnt}} * \left[1 + (v_{wnt2}(1 - \sin(2\pi(x + 0.5))))^{\eta_{\text{wnt}}}\right]^{-1} \tag{B.15}$$

$$V_{\text{GDF}}(x) = a_{\text{gdf}} * \left[1 + (v_{gdf1}(1 - \sin(2\pi x)))^{\eta_{\text{gdf}}}\right]^{-1}$$
$$+ a_{\text{gdf}} * \left[1 + (v_{gdf2}(1 - \sin(2\pi(x + 0.5))))^{\eta_{\text{gdf}}}\right]^{-1} \tag{B.16}$$

The parameters used for the PB, MRF models for the retrogressed feathers are listed bellow:

Parameters for the PB model

Variable	Value
D_a	1e-2
D_b	4e-1
r_a	1e-2
r_b	15e-3
r_c	3e-4
b_a	0
b_b	2e-1
b_c	5e-4
s	1e-2
s_a	18e-1
s_b	18e-1
s_c	35e-2
s_g	1e-3
n_g	-2

Parameters for the MRF model

Parameter	Chicken primary remige	Chicken breast plume (with after-feather)	Ostrich primary remige	Emu primary remige
D_{RA}	1e-2	1e-2	1e-2	1e-2
D_{WNT}	1e-1	4e-1	1e-1	4e-1
D_{GDF}	1e-2	1e-2	1e-2	1e-2
D_{GREM}	1e-2	1e-2	1e-2	1e-2
V_{RAo}	8e-6	4e-6	4e-6	4e-6
V_R	2e-6	2e-6	2e-6	2e-6
V_{GREM}	1e-6	5e-6	1e-5	5e-6
B_{RAo}	1e-1	1e-1	1e-1	1e-1
B_{WNT}	0	0	0	0
B_{GDF}	0	0	0	0
B_{GREM}	0	0	0	0
B_{CYP}	5e-2	N/A	N/A	N/A
B_{BP}	1e-1	N/A	N/A	N/A
$\mathrm{ra}_{\mathrm{deg}}$	1	1	1	1
r_{deg1}	1e-4	1e-4	1e-4	1e-4
r_{deg2}	1e-5	1e-5	1e-5	1e-5
bp_{deg1}	1e-4	1e-4	1e-4	1e-4
bp_{deg2}	1e-5	1e-5	1e-5	1e-5
$\mathrm{rabp}_{\mathrm{deg}}$	1e-1	1e-1	1e-1	1e-1
$\mathrm{wnt}_{\mathrm{deg}}$	1e-4	1e-4	1e-4	1e-4
$\mathrm{gdf}_{\mathrm{deg}}$	1e-4	1e-5	1e-4	1e-5
$\mathrm{grem}_{\mathrm{deg}}$	1e-4	1e-4	1e-4	1e-4
r_{on}	1e-3	1	1	1
r_{off}	1e-6	1e-3	1e-3	1e-3
m_{on}	1	1	1	1
m_{off}	1e-3	1e-3	1e-3	1e-3
j_{α}	1	1	1	1
j_{β}	1e-3	1e-2	1e-2	1e-2
k_p	5e-1	5e-1	5e-1	5e-1
k_1	1e-2	1e-2	1e-2	1e-2
k_2	1e-1	6e-3	1e-1	6e-3
k_3	1e-2	1e-2	1e-2	1e-2
k_4	4e-3	4e-3	4e-3	4e-3
k_5	3e-1	1e-2	7e-4	1e-2

Parameter	Chicken primary remige	Chicken breast plume (with after-feather)	Ostrich primary remige	Emu primary remige
n_1	2	2	2	2
n_2	1	1	1	1
n_3	-1	-1	-1	-1
n_4, n_5	-2	-2	-2	-2
β	0	0	0	0
v_{cyp}	4	N/A	N/A	N/A
v_{bp}	3	5	N/A	N/A
v_{wnt1}, v_{wnt2}	5, N/A	15, 150	6e-1, N/A	50, 50
v_{gdf1}, v_{gdf2}	10, N/A	50, 50	10, N/A	50, 50
a_{cyp}	5	1	1	1
a_{bp}	1	1	1	1
a_{wnt}	4e-4	4e-4	4e-4	4e-4
a_{gdf}	8e-6	4e-6	4e-6	4e-6
η_{wnt}	-2	2	-2	2
η_{gdf}	N/A	2	N/A	2

Appendix C

A Single-Cell Tracking Model for Irregular Cell Shapes

All simulations are run using MATLAB 2016a. To solve for cell movement a TVD 2nd order Runge-Kutta is used with a time step of $\Delta t = 0.1$. The continuous ODE's (eqs) were solved using a forward Euler scheme with a time step of $\Delta t = 1$. For all simulations:

Variable	Value
μ	0.1
V_0, U_0	1, 1
σ	0.1

Figure 3.5:

For the three cell types, red, blue, and black, their rectellipse values are:

Red- $s = 0.9$, $a = 1$, $b = 1$ Blue- $s = 0.9$, $a = 1.2$, $b = 0.6$ Black- $s = 0$, $a = 1$, $b = 1$

Figure 3.6:

An value of $C_0 = 50$ was used to initialize the system.

Variable	Value
p_0^r, p_0^a, p_0^s	0.1, 0.9, 0
p_1^r, p_1^a, p_1^s	0.1, 0.7, 0.2
ν_0, ν_1	0.1, 0.1
d_0, d_1, d_2	0.01, 0.01, 0.5

Figure 3.7:

An value of $C_0 = 15$ was used to initialize the system.

Variable	Value
p_0^r, p_0^a, p_0^s	0.1, 0.9, 0
p_1^r, p_1^a, p_1^s	0.1, 0.7, 0.2
ν_0, ν_1	0.1, 0.1
d_0, d_1, d_2	0.01, 0.01, 0.5

Appendix D

Notch Signaling as a Strategy for Robust Barb Formation in Feathers

All simulations are run using MATLAB 2016a. To solve for cell movement a TVD 2nd order Runge-Kutta is used with a time step of $\Delta t = 0.1$. For all simulations:

Variable	Value
D_a	8e-3
D_b	2e-1
r_a	1e-2
r_b	15e-3
r_c	3e-4
b_a	1
b_b	2e-2
b_c	5e-4
s	1e-2
s_a	1.8
s_b	1
s_c	0.3
s_g	1e-3
n_g	-2

Notch Serrate Model A and B have parameters:

Variable	Value
s_N, s_S	0.1, 0.1
b_N, b_S	0.1, 0.3
$\deg_N$, $\deg_S$	0.01, 0.01
n_N, n_S	2,2
γ_N, γ_S	100,100

Appendix E

A Discrete Modeling Framework for Zebrafish Jaw Formation

All simulations are run using MATLAB 2016a. To solve for cell movement and growth TVD 2nd order Runge-Kutta is used with a time step of $\Delta t = 0.1$, to solve for gene-expression a TVD 2nd order Runge-Kutta is used with a time step of $\Delta t = 0.005$. For all simulations:

Variable	Value
U_0, V_0	0.1, 0.1
ξ, η	0.1, 0.3
ζ	200
D_E, D_B	10, 1
r_E, r_B	0.2, 0.2
α_E, α_B	1, 1
J_M, N_M, D_M, H_M	0.1-1, 0.5, 1, 0.4
b_J, b_N, b_D, b_H	0.4, 0.1, 0.1, 0
r_J, r_N, r_D, r_H, r_S	0.1, 0.1, 0.1, 0.1, 1
k_{on}	1.1
γ_{J1}, γ_{J2}, γ_{J3}, γ_{J4}	0.3, 0.03, 0.3, 1
γ_{N1}	0.3
γ_{D1}, γ_{D2}, γ_{D3}, γ_{D4}	0.4, 0.3, 0.1 0.3
γ_{H1}, γ_{H2}	0.3, 1